Outflow and feedback in active galactic nuclei: high-resolution X-ray spectroscopy and variability

Rob Detmers

December 1, 2011

"Take what you can from your dreams, make them as real as anything"
Dave Matthews

ISBN 978-90-393-5693-7

Cover image: Hubble Space Telescope image of Mrk 509 showing the bright core around the supermassive black hole (credits: MAST / SRON). The inset is taken from an animated film of a black hole wind (credits: Nahum Arav and Daniel Zukowski). The cover was made by Oliwia Madej.

Outflow and feedback in active galactic nuclei: high−resolution X-ray spectroscopy and variability

Uitstroom en terugkoppeling in actieve sterrenstelsels: hoge resolutie Röntgen spectroscopie en variabiliteit

(met een samenvatting in het Nederlands)

Proefschrift

ter verkrijging van de graad van doctor aan de Universiteit Utrecht op gezag van de rector magnificus, prof. dr. G. J. van der Zwaan, ingevolge het besluit van het college voor promoties in het openbaar te verdedigen op donderdag 1 december 2011 des middags te 2.30 uur

door

Robertus Gerardus Detmers

geboren op 14 juni 1981 te Arnhem

Promotor: Prof. dr. F. W M. Verbunt

Co-promotor: Dr. J. S. Kaastra

Dit proefschrift werd mede mogelijk gemaakt met financiële steun van NWO en LKBF

Contents

Chapter 1

Introduction

1.1 Active Galactic Nuclei

It is generally believed that the center of every galaxy contains a super−massive black hole (SMBH). With masses ranging from 10^6 to 10^{10} $M_\odot$, they are the most powerful emitters of electromagnetic radiation in the universe. When actively accreting they are called Active Galactic Nuclei, or AGN for short. Probably one of the best definitions is given by Peterson (2008):
"Active nuclei are those that emit radiation that is fundamentally powered by accretion onto super−massive ($\gtrsim 10^6$ $M_\odot$) black holes"

It is now widely recognized that AGN are connected to the evolution of the host galaxy and are even affecting the evolution of the largest clusters of galaxies (Scannapieco & Oh 2004, Di Matteo et al. 2005, Somerville et al. 2008, Hopkins & Elvis 2010). How AGN exactly affects the evolution of the host galaxies is still not known, but one of the prime suspects (aside from the radiation) are the outflows, which are seen in a large (50 %) fraction of AGN. Therefore in order to investigate this connection (also known as feedback), we need to look closely at the properties of the AGN outflows, which we try to unravel here by using high resolution X-ray spectroscopy and variability. AGN emit in every energy band, from the radio all the way to the gamma-ray band. The field of AGN research is a vast one. I will therefore give a brief general overview of the aspects of the X-ray bright AGN important for my work (mostly Seyfert 1 galaxies) and then discuss in detail the outflows, emission lines and variability that make up the core of this PhD research.

1.2 A brief history of AGN

The first systematic study of local, bright AGN was done by Seyfert (1943). This study of the bright, blue cores of local spiral galaxies showed the presence of strong emission lines. The sources were divided in Type 1 and Type 2 sources, where the latter lack the broad (Full Width Half Maximum (FWHM) >1000 km s^{-1}) emission lines, but do show the narrow (FWHM < 500 km s^{-1}) emission lines. What these sources exactly were, remained unknown for quite some time.

In radio band surveys, another class of strange objects were discovered, the quasars. As they appeared to be connected with star-like objects in shape when seen through optical telescopes, they were also called Quasi-Stellar Objects (QSO). However the optical spectra were not at all star-like. The main breakthrough in revealing the nature of QSO's came when Schmidt (1963) realized that the emission lines of the quasar 3C 273 were the hydrogen Balmer lines, but then redshifted to $z = 0.158$. This means that these sources are located at cosmological distances (approximately 2.2 billion lightyears in this case) and therefore the intrinsic luminosity must be 100 times higher than the brightest galaxies. On top of that it became apparent that these quasars were also highly variable at all wavelengths on timescales on the order of days. This led to the main investigation and discussion of what could be producing the light of a trillion stars in a region with the size of a few light days. Eventually this resulted in the theory of accretion onto super−massive black holes as the main power source for quasars.

It was also realized that the Seyfert galaxies actually were accreting super−massive black holes. Their luminosities were far less than that of quasars, but due to their nearby location, they could be studied in great detail. The distinction between Seyfert galaxies and quasars is a rather artificial one. Quasars are essentially scaled up (high mass and high luminosity) versions of Seyfert galaxies that are generally located at large distance ($z \geq 0.1$). The luminosity is usually used to distinguish between a Seyfert galaxy and a quasar, where AGN with a bolometric luminosity in excess of 10^{38} W are classified as quasars.

Support for the idea of accreting SMBHs as a power source for both quasars and Seyfert galaxies, comes from observations of the super−massive black hole in our Galaxy, Sgr A*, by measuring the orbits of stars around the center (Schödel et al. 2003, Ghez et al. 2005) and by mega-maser measurements in the accretion disk of NGC 4258 (Miyoshi et al. 1995). Additional proof comes from the so-called reverberation mapping (Peterson & Wandel 2000). This is based on tracking the response of the broad emission lines studied in the optical/UV band, to variations in the continuum flux. If the gas which is producing these emission lines is virialized (i.e. the motion is dominated by the gravity of the black hole), then measuring the line width for different emission lines should yield the same mass for the black hole. By comparing these reverberation masses with those obtained from gas and stellar dynamics, the validity of this idea can be checked.

Currently the field of AGN research is a vast one. From researchers studying the highest redshift quasars in order to understand how AGN are formed in the early

universe, to clusters of galaxies which show the interaction of the relativistic AGN jet and to the outflows that are thought to affect star formation and galaxy evolution. Before discussing the details of the outflows and the research shown in this Thesis it is important to first discuss the properties of AGN.

1.3 The anatomy of an Active Galactic Nucleus

Almost every X-ray bright AGN consists of the following components.

- A central super−massive black hole
- A (relativistic) jet
- An accretion disk
- A hot corona
- A Broad emission Line Region (BLR)
- A Narrow emission Line Region (NLR)
- A dusty torus-like structure, responsible for the obscuration in Type 2 AGN
- An ionized outflow or wind (seen in about 50 % of Type 1 AGN)

The general picture is that shown in Fig. 1.1, a central black hole surrounded by an accretion disk. The outer edge of the accretion disk is most likely the inner edge of the BLR, at which the dust sublimation temperature is reached and the inner edge of the dusty torus begins. All of this is embedded in a low density gas, the NLR. It is the dusty torus, that is the key ingredient for the unification model of AGN. If our line of sight does not intersect the torus, we directly see the BLR and the accretion disk and we observe a Type 1 AGN. If on the other hand our line of sight intersects with the torus, then the central regions are blocked and we only see the far away emission of the NLR. The outflows are only seen in about 50 % of the Type 1 AGN and are thought to originate in the accretion disk, BLR or the inner edge of the torus (see e.g. Crenshaw et al. 2003, for an overview).

1.3.1 (Relativistic) Jet

Jets (whether relativistic or not) are seen in many accreting compact objects, including AGN. Blazars (AGN where we look directly into the jet) and radio galaxies (AGN that have a strong radio flux) both show strong, relativistic jets. I do not describe the relativistic jet in further detail here, as the AGN studied in this work are all radio quiet, which have either no or very weak jets. For for information on relativistic jets in AGN, see the overview by Harris & Krawczynski (2006).

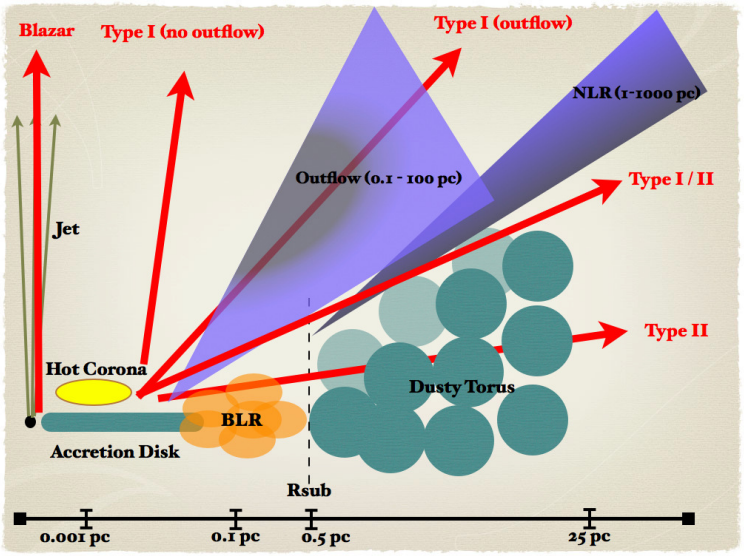

Figure 1.1: A sketch of the inner region of an AGN. The different regions are marked with their name. R_{sub} is the dust sublimation radius. On the x−axis a rough distance scale is shown. The thick red arrows show the type of AGN observed for different viewing angles.

1.3.2 Accretion disk

Accretion of gas and dust onto a (super−massive) black hole is the most efficient method to extract energy from normal matter. This is the foremost way to power the AGN. As the gas falling onto the AGN still has some residual angular momentum, it will form an accretion disk around the black hole. The simplest model for an accretion disk is that of a geometrically thin and optically thick disk, so that its spectrum can be approximated by a blackbody (Shakura & Sunyaev 1973). Thermal emission from this accretion disk is responsible for most of the soft X-ray, UV and optical continuum emission. Depending on the mass of the black hole and on the accretion rate it will radiate most of its energy in either the EUV or optical regime. For example, Mrk 509 with its black hole mass of 1.43×10^8 $M_\odot$ radiates most of its energy in the far UV band, while the accretion disks in 10^6 $M_\odot$ AGN radiate most of their energy in the EUV-ray band. The assumption of a blackbody is a gross oversimplification, however, as the accretion disk in reality is much more complex and is subject to instabilities. So although the accretion disk spectra of AGN can be well fitted by a blackbody component, any derived parameters should be taken with caution. The accretion disk is also the region where some of the outflows are thought to originate.

1.3.3 Hot corona

X-ray spectra of AGN show a hard power−law component (above 0.5 keV) in the form of $F_E \sim E^{-\tau}$, that can not be explained by an extension of the blackbody component to X-ray energies. This component is thought to be produced by inverse Compton scattering of hot electrons that are present above the accretion disk in a 'hot corona'. What the exact shape or nature of this corona is, is not entirely clear. It can either be the base of a relativistic jet, a layer of hot electrons above the accretion disk or patches of hot electrons generated by magnetic reconnections, like in the corona of the sun.

1.3.4 Broad emission Line Region

Optical and UV spectra of Type 1 AGN show broadened emission lines, with widths up to several 1000s km s^{-1}. It are these emission lines that are used for the reverberation mapping of AGN to determine the mass of the black hole by tracking the response of the emission lines to continuum variations. Although the first variations of emission lines were observed as early as 1968 (Andrillat 1968), it was not until the establishment of the AGN Watch consortium in 1988 that systematic long-term observations were performed on a sample of the brightest Seyfert 1 galaxies (Clavel et al. 1991, Peterson et al. 1991). From this dedicated monitoring, the derived radius of the BLR seemed to vary over the years. From this rather puzzling result (how could the gas be at different places from one year to the next ?), the 'locally optimally emitting cloud (LOC)' model was conceived (Baldwin et al. 1995). In this model, the gas is present throughout the BLR, but is seen only where the conditions for reverberation mapping (the largest change in line luminosity) are optimal. Although the LOC model has been very successful in explaining the observed properties of the BLR, a fully complete photoionization model of the BLR is still missing.

These reverberation mapping campaigns also resulted in a relation between the radius of the H_β emission line and the continuum luminosity at 5100 Å (see Fig. 1.2). This relation allows for quick estimates on the mass of the black hole in Type 1 AGN and also in nearby quasars. The only quantities that are needed are the velocity width of the emission line and the continuum luminosity as a proxy for the radius.

The exact nature of the BLR is still uncertain. The most favored model is where the BLR is located between the edge of the accretion disk and the inner edge of the dusty torus, where the gas in the accretion disk becomes unstable to self-gravity and forms clumps. These clumps could be part of the accretion flow or could be part of an outflow or wind from the accretion disk. The exact kinematics (inflow/outflow) of the BLR are currently still unknown, although observations have shown that the dominant motion is virialized motion around the SMBH (Peterson 2010). One major uncertainty in the derived masses of the black holes is the effect of the inclination of the BLR. Although for a large sample of sources, the M−σ relation holds quite well, the scatter in individual cases can be quite large (up to an order of magnitude in some cases).

Recently also X-ray broad emission lines have been detected in high resolution

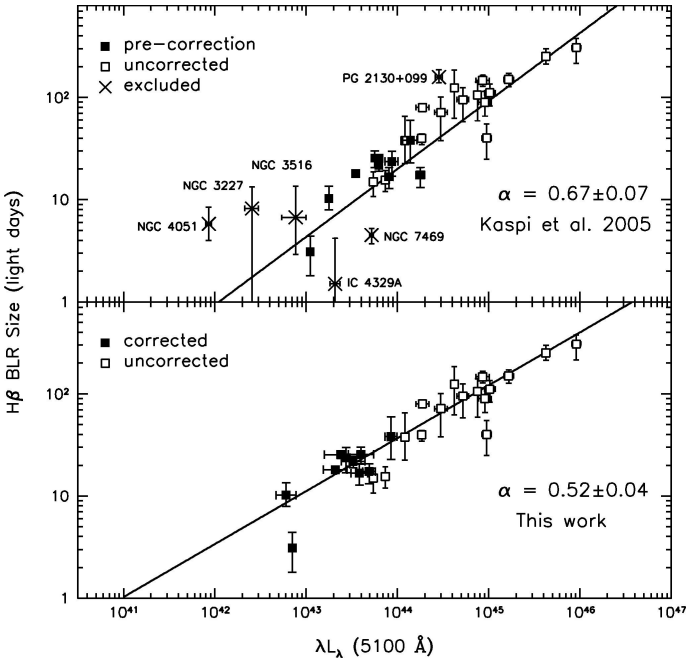

Figure 1.2: The R − L relation for a sample of reverberation mapped AGN (Bentz et al. 2006). Unfilled boxes are uncorrected for the host galaxy contribution, while filled boxes are corrected for host galaxy contribution to the emission lines.

spectra of several Seyfert 1 galaxies (Kaastra et al. 2002b, Costantini et al. 2007a, Longinotti et al. 2009, Blustin & Fabian 2009). The widths of the lines also suggest an origin in the BLR. The LOC model has actually been successfully extended up to the X-ray regime, showing that the same gas responsible for the UV and optical lines is also responsible for the X-ray broad emission lines (Costantini et al. 2007a). Velocity resolved reverberation mapping is the best method to obtain accurate information on the kinematics of the BLR (Peterson 2010) and although it is within the reach of current technology (Horne et al. 2004), it has been only done for a few sources (Denney et al. 2009). This method did reveal the different kinematics (inflow, outflow and virialized motion) for each of the three different sources, so further studies can be used to probe the geometry and kinematics of the BLR, thereby reducing the systematic uncertainties of the black hole mass measurements which are still present at the moment.

1.3.5 Narrow emission Line Region

Narrow (FWHM less than 500 km s^{-1}) emission lines are seen in every energy band, from IR to the X-ray regime. These lines are located at large (1−1000 pc) distances from

the central source (see e.g. Netzer 2008). The exact geometry and origin of the NLR are unknown at the moment, but a cone−like shape seems to be favored, based on the imaging observations of several close Type 2 Seyfert galaxies (Bianchi et al. 2006). The observed spectrum of the NLR includes strong forbidden emission lines due to the low density of the gas. For the closest sources, spatially resolved spectroscopy can be performed (Collins et al. 2009, Kraemer et al. 2009). These studies show that although on large scales the NLR is relatively smooth it has a patchy structure on smaller scales, most likely due to different densities in these different regions. The density structure has been studied in a few nearby Type 2 AGN (Bennert et al. 2006b, Bianchi et al. 2006) and shows different distributions for different galaxies, ranging from $n \sim R^{-1}$ to R^{-2}. Obtaining these profiles is not trivial, as the host galaxy emission has to be subtracted and the spectra also have to be de−reddened (the removal of the contribution of intervening dust).

In Type 1 AGN it is much harder to observe the narrow emission lines, due to the bright continuum emission from the central source. In the X-ray regime, generally the O VII forbidden emission line is the strongest and is most frequently detected also in the spectra of Type 1 AGN (Kaastra et al. 2002b, Behar et al. 2003, Costantini et al. 2007a). In the optical and UV bands, separating the narrow emission features from the broad emission lines can be difficult. This is why generally speaking NLR studies are easier to perform in Type 2 AGN. Only for a few nearby Type 1 AGN the NLR has been studied in detail (NGC 4151 for example, Das et al. 2005, Kraemer et al. 2008). The connection of the NLR with the ionized outflow is still unclear. In some sources, NGC 3783 (Behar et al. 2003) and NGC 5548 (see Chapter 4), it seems that both the emission and absorption features could originate in the same gas, but solid proof in the form of multi-wavelength photoionization modeling is still lacking in most sources.

1.3.6 The dusty torus

The torus or "dusty doughnut" is the structure which is mainly responsible for the observed differences between Type 1 and Type 2 AGN. Antonucci (1993) first proposed an optically thick, dusty structure to account for the observed differences between the two types of AGN. If the observer's line of sight crosses the torus, the radiation from the central engine is blocked and one only sees the narrow emission lines from the far away (10 – 100s of pc) narrow line region (NLR). Only if we look from an angle which does not intersect the torus, we can directly see the central engine. In this case we see both the broad− and narrow emission lines, as well as the continuum emission from the central source (the accretion disk). This so−called 'Unified Model' of AGN has been very successful in explaining the observed differences between Type 1 and Type 2 AGN (see Fig. 1.1). The torus is also the main supply source for the gas which eventually accretes unto the black hole. The size of the torus is thought to be on the order of tens of pc. It re-emits the absorbed X-ray and UV flux in the (near−) IR band. The inner radius of the torus depends on the luminosity of the central source, as this controls the dust sublimation radius. In some models the outflow originates

as a thermal wind near the inner edge of the torus (Krolik & Kriss 2001).

1.3.7 The outflow

Outflows are an integral part of AGN. About half of the Type 1 AGN show narrow, blueshifted absorption lines in their UV and X-ray spectra (NAL outflows). The most extreme example of AGN outflows are the Broad Absorption Line (BAL) outflows seen in luminous quasars, which reach outflow velocities of up to 50 000 km s^{-1}. Also in about 50 % of the local Seyfert galaxies outflows are seen, although the outflow velocities are less extreme, on the order of 1000s km s^{-1}. The exact origin of these outflows is not known, they can either originate from the accretion disk or the dusty torus. These outflows are thought to be the link between the host galaxy and the AGN. As this work mainly concerns the outflows seen in local Seyfert 1 galaxies, we discuss them further in a separate section (Section 1.4).

1.3.8 New developments

Recent developments and observations have made a few dents in the unified model. Although it is still very successful in explaining the main differences between the types of AGN, there are cases that show that the picture is more complex than what is assumed.

Evolution

The evolutionary stage is a key ingredient missing from the unified model. The evolutionary stage of an AGN can be very important for its properties as well. This implies that the distinction between Type 1 and Type 2 AGN is not only due to the viewing angle, but must also reflect the state of evolution the AGN is in. The discovery of completely absorbed AGN, showing blueshifted emission lines of Ne v, indicates that there are cocoon−like AGN, completely encased in dust and gas (Spoon & Holt 2009, Spoon et al. 2009). One can think of these as infant AGN, where the young AGN tries to clear away the surrounding gas and dust. Over time the AGN will start carving an opening in the surrounding gas and dust. Eventually the AGN has blown away all the gas and dust and it starves itself. This way, the distinction between Type 1 and Type 2 AGN depends also on the evolutionary stage of the AGN. However these AGN are generally found in ULIRG (ultra−luminous infrared galaxies) type of galaxies, which are rare in the nearby universe.

Clumpy torus

Recent results point to a more patchy / clumpy torus, instead of one solid object that obscures the central engine completely. There are several observations that support this idea. One is that there are AGN that switch between Compton thick absorption (i.e. absorption by gas with a column density $\geq 10^{28}$ m^{-2}) and Compton

thin (absorption by gas with a column density $\leq 10^{27}$ m^{-2}) in a matter of days (NGC 1365, see Risaliti et al. 2005). This can not be due to changes in the ionization state, as the total column density should remain constant in that case. It seems that dense 'clouds' of gas are moving in front of the central source. Another point of evidence comes from the recent IR interferometry observations of several nearby AGN (Jaffe et al. 2004, Tristram et al. 2007, Burtscher et al. 2009). These observations show hot (T $\geq$ 800 K) and colder (200 − 300 K) dust close to each other. This can only be the case if the torus is clumpy instead of uniform. In addition, recent observations using IR reverberation mapping (Suganuma et al. 2006) have shown that the inner radius of the torus is on the order of 0.1 pc (depending on the source). The time lags obtained from the IR reverberation are just slightly larger than those obtained from the BLR reverberation mapping. This indicates that the BLR radius is constrained by the inner edge of the torus and that the torus is the region where dust sublimates in the BLR. These results all point towards a more clumpy torus scenario, which means that the distinction between Type 1 and Type 2 not only depends on the inclination angle, but also is a statistical property, i.e. there is a chance that even if the inclination angle is small (so that we should observe a Type 2 AGN), we might still look through the clumpy torus and see a Type 1 AGN.

Intermediate line region

New results connecting the absorbing to the emitting gas have shown the presence of emission lines with an intermediate FWHM (700 km s^{-1}). Their widths place these lines at distances 0.1 − 1 pc away from the central source. The obtained covering factors (i.e. the fraction of the continuum source covered by the absorbers in the line−of−sight) from UV spectra are small, on the order of 0.1. The FWHM's of these lines are similar to those of the optical forbidden high ionization lines (FHIL), which are emission lines of highly ionized ions, such as Fe x. Interestingly, Mullaney et al. (2009) recently performed photoionization models for the FHILs in Ark 564 and show that the location of the FHIL lines is consistent with the inner edge of the torus. In a significant number of sources, the FHIL lines show large (several 100s of km s^{-1}) blueshifts, possibly indicating an outflow (Gelbord et al. 2009). This raises the question whether these FHIL emission lines and the ILR are connected to the ionized outflows. Are they one and the same gas ? Or are they different phenomenon altogether?

Clearly the field of AGN research is vibrant and with the availability of new techniques, future observatories (such as ASTRO-H and ALMA) and large surveys (such as the Sloan Digital Sky Survey) the physics of the inner regions and the connections between the different types of AGN can be revealed.

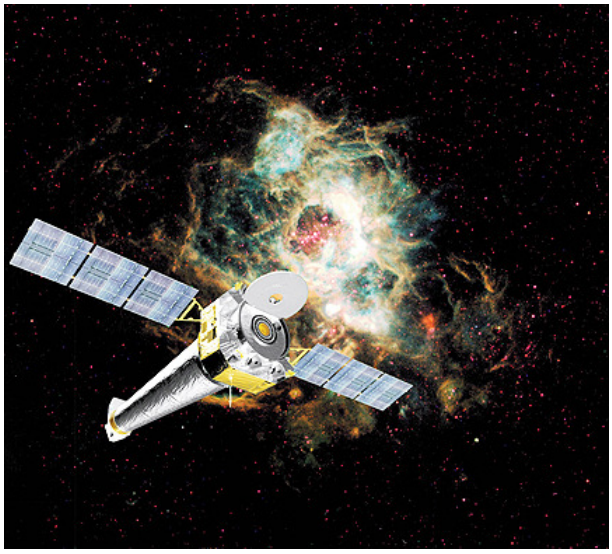

Figure 1.3: Artist impression of Chandra. Image courtesy of NASA.

1.4 AGN outflows

1.4.1 Early X-ray observations of outflows

The first tentative evidence of X-ray absorption by highly ionized material in an AGN was obtained by the Einstein Observatory. It was suggested by Halpern (1984) that the attenuation of the continuum in MR2251−178 could be caused by a variable column density of photoionized gas, a so-called warm absorber. Other early X-ray satellites were EXOSAT and Ginga, which supported the interpretation of the existence of a warm absorber. The low spectral resolution (R = 20 at 1 keV) of the instruments onboard of these satellites however prevented observers from separating neutral from ionized absorption. Only with the advent of medium (R = 50 at 6 keV) resolution spectrometers, such as the Solid−State Imaging Spectrometer on board of ASCA, could a major step forward be made and O VII and O VIII absorption features were detected in several Seyfert 1 spectra. The medium resolution meant however that the features were blended with the iron unresolved transition array (UTA, blended, closely spaced absorption lines of iron ions). Column densities and ionization states could still be obtained by the ratios of the depths of the edges. Accurate ionic column densities and especially outflow velocities (if indeed outflowing) however were still unknown. At the same time, high resolution (R 20000) UV spectra of Type 1 AGN, showed the presence of blueshifted absorption lines by ionized C, N and O ions. The high spectral resolution allowed for accurate outflow velocity determinations of up to 2000 km s^{-1}. The questions of whether the detected X-ray absorbing gas was also outflowing and what its connection was to the UV outflows would only be answered

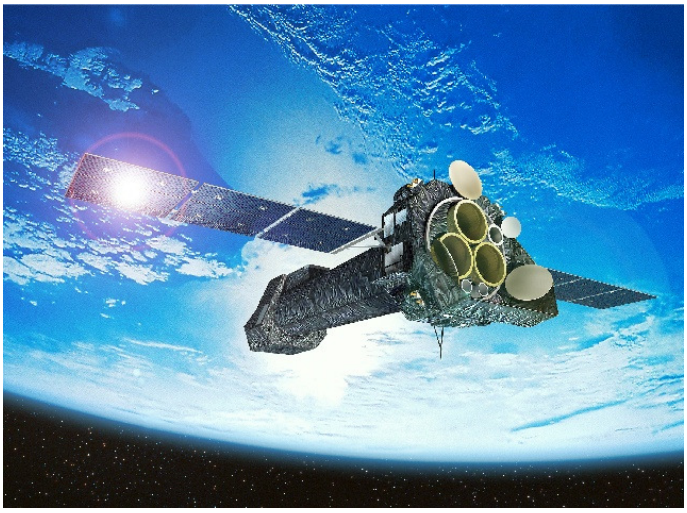

Figure 1.4: Artist impression of XMM-Newton in orbit above Africa. Image courtesy of ESA.

with the next generation of X-ray satellites.

1.4.2 The revolution of *Chandra* and *XMM-Newton*

With the launch of the *Chandra* and *XMM-Newton* telescopes (see Fig. 1.3 and 1.4 for artistic impressions of both satellites) one decade ago, the field of X-ray spectroscopy was revolutionized. Thanks to the high spectral resolution offered by the gratings (the Reflection Grating Spectrometer on board of *XMM-Newton* and the Low Energy Transmission Grating Spectrometer (LETGS) and High Energy Transmission Grating Spectrometer (HETGS) on board of *Chandra*), resolving powers of R = 200 – 1000 could be reached. The ionized outflow which was previously only visible by absorption edges, was shown to consist of a wealth of absorption lines. From O III to O VIII and Fe I to Fe XXIV, a whole range of ions, transitions and ionization states were visible (see e.g. Kaastra et al. 2002b, Kaspi et al. 2002). Almost all of these absorption lines appeared blue-shifted with respect to the AGN rest frame. This means that this absorbing gas is actually outflowing from the nucleus with velocities up to 2000 km s^{-1}, just as had been observed in UV spectra of Type 1 AGN. Due to the superior resolution offered by these new instruments, a proper spectroscopic analysis of the ionized outflow could now be performed. Also (narrow) emission lines were detected in many AGN spectra, especially those of Type 2 AGN. This wealth of information meant that for the first time spectroscopy of the absorption and emission regions of AGN could be done. The ionization structure of the outflow and emitting gas could be obtained from line ratios and ionic column densities. Kinematics could be obtained from the line shifts and the line broadening. These two satellites have paved the way for multi-wavelength, high-resolution spectroscopy of local AGN.

1.4.3 Observed properties of NAL outflows

The NAL outflows are characterized by narrow (FWHM less than several 100 km s^{-1}), blueshifted absorption lines, reaching outflow velocities of up to several thousand km s^{-1}. High resolution UV spectra show multiple velocity components, in some cases up to fourteen (Mrk 509, Kriss et al. 2011). They span a huge range in ionization states, from Fe I to Fe XVI and they show absorption lines of all of the most abundant elements, such as C, N, O, Ne, Mg, Si and Fe. The kinematics of the UV and X-ray outflows are quite similar and this has led to the current paradigm that the UV and X-ray absorbers are most likely co-located, where the UV absorbers are denser clumps in a hotter, more tenuous X-ray gas. The UV spectra show lowly ionized gas (showing up in absorption lines of C II, Mg II) which consists of ions that escape detection in the X-ray spectra. They also show medium ionized gas, seen in absorption lines of N V, C IV and O VI. These ions also show up in the X-ray part of the outflow, although generally O VI is the only abundant ion that shows up in both bands. The X-ray spectrum of the outflow also shows a higher ionized component that is not seen in UV spectra. Comparisons of the column densities are difficult, as the UV lines are often heavily saturated. In most cases the column densities were significantly different between the UV and X-ray outflows. Later it was realized that velocity dependent covering factors of the UV components could account for the observed differences in column density (Arav et al. 2002).

There has been a lot of work done in the last decade to characterize the properties of these outflows and significant progress has been made (Kaastra et al. 2000, Kaspi et al. 2002, Steenbrugge et al. 2005, Blustin et al. 2005, Costantini et al. 2007a). The location and origin of the outflow, however, remain unsolved problems. Estimates based on variability (see Sect. 1.5) have placed the outflow from within 0.1 pc of the central source in NGC 4051 (Steenbrugge et al. 2009) to within 7 pc in NGC 5548 (see Chapter 3). For the UV absorbers the distance limits are larger, such as less than 25 pc in NGC 3783 (Gabel et al. 2003) or less than 250 pc in Mrk 509 (Kriss et al. 2011). All these observations have also shown that in order to detect all the ionization and velocity components of the outflow, very high quality spectra are required (usually requiring $10^5 - 10^6$ s of observing time), limiting the number of sources whose outflows have been studied with high levels of detail (NGC 3783, NGC 5548, NGC 4151, NGC 4051, MCG-6-30-15 and Mrk 509).

1.4.4 Outflow models

There are several models for explaining the origin and driving force of the outflows in AGN. They can be divided into thermal, radiatively driven and magnetic.

The most well-known of the thermal wind or Compton heated wind models is evaporation of the dusty 'torus' (Krolik & Kriss 2001). In this model the ionizing flux of the central source evaporates material of the torus when the local sound speed exceeds the escape speed. The velocities that can be reached by this process are on the order of several hundreds of km s^{-1}. There can be a range of densities and

temperatures in the evaporated gas, leading to the observed wide range of ionization states. Blustin et al. (2005) showed that estimates of the location of the outflows in local Seyfert 1 galaxies are consistent with the location of the dusty 'torus'. Also other estimates (see e.g. Costantini 2010) of the location of the outflow are indeed consistent with the location of the inner edge of the torus. Only in a few cases and then only for the highest ionized gas, was the estimated distance closer to the central source, i.e. originating in the BLR. However all of these distance estimates are still uncertain or not constraining enough, as generally only upper or lower limits can be obtained from the observations. Also the outflow velocities of these thermal wind models are not large enough to explain the fastest outflows (i.e. $\geq$1000 km s^{-1}).

Due to their large luminosities, a natural candidate for the origin of the outflow is a radiatively driven wind. In the case of powerful quasars, such as the Broad Absorption Line Quasars (BAL-QSOs), models indeed show that the radiation pressure can account for the observed outflow velocities (10000s km s^{-1}). The presence of line−locking in their UV spectra supports this hypothesis (Arav et al. 1995). Even in Seyfert galaxies, radiatively driven winds can play a role. The radiation pressure on dust is many times larger than that on ionized gas, due to the larger opacity of the dust grains (see e.g. Fabian et al. 2008). This way, the effective radiation pressure is many times larger than that for dust free ionized gas so that an outflow may be driven. The attractiveness of the line−driven model is that it does not rely on forces that are hard to measure (i.e. magnetic forces) and so can be tested directly against observations.

The third type of models are the magnetohydrodynamic models (Blandford & McKee 1982, Königl & Kartje 1994, Fukumura et al. 2010). In these models a wind is launched from the accretion disk by magnetic fields and is then accelerated outwards by the irradiation of the AGN. In most of these models, there is a large column density at high inclination angles (around 90 degrees, i.e. in the plane of the accretion disk), while the low column density gas is at low inclination angles (around zero degrees). This means that the column density of the wind is also a function of the inclination angle of the system. This difference in column density is a natural explanation for the observed differences between Type 1 and Type 2 AGN and it was indeed also suggested (Königl & Kartje 1994) that the torus is in fact an MHD type of wind. Magnetic fields are a natural occurrence in accretion disks, as the most favored model to remove angular momentum from the accreted material is through the magneto−rotational instability (MRI, Balbus & Hawley 1991), so magnetically driven winds are a good candidate for the origin of these outflows.

1.4.5 Comparison with observations

In most cases it is difficult to directly compare outflow models to observations. Accurate locations of the outflow are rarely known and wind models do not yet accurately predict observable parameters, such as ionic column densities, ionization structure. However progress is being made, but a systematic analysis of the observed proper-

ties of the outflows and a comparison to the different models is still lacking. The main problem is that in most sources we still lack high quality spectra of the outflows. However the models still make some predictions regarding outflow velocities, velocity structure or location of the outflow.

- Thermal wind models: Velocities of several 100s km s^{-1}, origin near the inner edge of the torus.
- Radiatively driven outflows: Velocities up to 50000 km s^{-1} (in the case of BAL QSOs), origin near the accretion disk (BLR) or the torus in the case of radiation pressure on dust.
- Magnetic outflows: Velocities up to 50000 km s^{-1}, origin in the accretion disk.

Obtaining accurate velocity, ionization and density profiles for multiple sources will greatly help determining the origin and the launch mechanism of the outflow.

1.4.6 Photoionization modeling

In order to model the observed absorption lines with a physical model we need to know the proper ionization balance of the gas. This can be obtained from the spectral energy distribution (SED) in combination with a photoionization code, such as Cloudy or XSTAR. These codes yield the absorption and emission of a slab of gas that has been irradiated by ionizing flux. A grid is then constructed for a range of ionization states and column densities of the gas. In the spectral fitting, this grid is then typically searched through using minimization procedures. These codes assume ionization equilibrium and generally do not allow for complex absorption structures, i.e. we are in the optically thin limit. Abundances can also be changed as needed. Also the shape of the SED is of crucial importance for the resulting ionization balance, as well as accurate and updated atomic physics (recombination rates for example). The effects of these parameters on the resulting ionization balance have been extensively tested (except for different abundances) by Chakravorty et al. (2009). A similar exercise was performed for the Mrk 509 campaign, although the changes in the ionization balance are not large for the different tested SEDs (see Fig. 1.5).

1.4.7 Structure of the outflow

The geometry and structure of the outflow are of importance for determining the properties and origin of the outflow. The ionization and velocity structure of the outflow can give us important clues as well. UV observations have shown that the outflow consists of multiple velocity components, in some cases five or more (e.g. NGC 5548, NGC 3783, Mrk 509). However the ions observed in the UV only cover a limited range of ionization states. X-ray observations have shown a similar velocity structure as the UV observations, but with less components as the lower resolution

means that velocity components are blended. In addition, a high velocity (1000s km s^{-1}) component that does not have any counterpart in the UV has been seen in some sources. This component is also highly ionized, which is the reason that it is undetectable in the UV spectra. Based on variability studies it is clear that the highest ionized gas in some sources at least also has the highest outflow velocity and is located closest to the central source (see Chapter 2). In other sources the connection between ionization parameter and outflow velocity is not so certain (Blustin et al. 2005). Again one has to be careful in drawing conclusions from low signal to noise spectra. The UV data give a much more accurate picture of the velocity structure of the outflow (due to the superior resolution) and it is clear that gas of the same ionization state can have multiple velocity components. This and the similar outflow velocities observed in the X-ray regime indicates that the X-ray and UV absorbing gas are co-located and that the outflow has local density gradients (cooler clumps absorbing UV radiation and warmer gas absorbing X-rays).

The ionization structure of the outflow is better studied in the X-ray regime, as it offers the full range of ionization states. By measuring the distribution of column density vs. ionization parameter, the ionization structure of the outflow can be investigated. By measuring how much gas there is at each ionization parameter, one can determine if the outflow is continuous or consists of separate components. Early analysis of outflows showed different results for different sources. In NGC 3783, it appears that the outflow consists of separate components, that appear to be in pressure equilibrium (Krongold et al. 2003). In NGC 5548 on the other hand, a continuous outflow is favored (Steenbrugge et al. 2005), while in Mrk 279 a continuous outflow is also favored, but with a more complex substructure (Costantini et al. 2007a). The best method to study the exact ionization structure of the outflow is to obtain accurate column densities as a function of ionization parameter. The way this is done is through the so-called Absorption Measure Distribution (AMD) (Holczer et al. 2007):

$$AMD = \frac{dN_H}{d(log\,\xi)}, \tag{1.1}$$

where N_H is the hydrogen column density and with the ionization parameter ξ defined in the following way (Tarter et al. 1969):

$$\xi = \left(\frac{L}{n\,R^2}\right), \tag{1.2}$$

with L the ionizing luminosity between $1 - 1000$ Rydberg, n the density of the gas and R the distance form the central source. By integrating over the full range of ξ of ions detected in the spectrum, the distribution of the AMD can be found for which the predicted ionic column densities match the observed column densities. This requires the use of photoionization codes to calculate the ionic fraction f_{ion} at each ξ. Also abundances have to be assumed, which are unknown a priori. The best method is to use the iron ions, as they span a large (5 orders of magnitude) range of ionization parameters and this way the AMD does not depend on relative

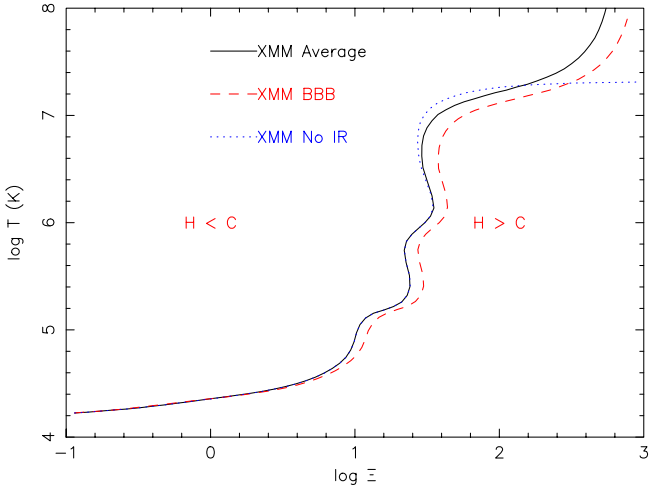

Figure 1.5: The cooling curve derived for three different SEDs of Mrk 509 (solid line: the average SED of 10 observations, dashed line: same as the solid line but with a big blue bump in the EUV region, dotted: same as the solid line but without any infrared contribution to the SED). Regions where heating (H) or cooling (C) dominate are indicated. Areas of the curve with a negative slope are unstable to changes in the ionizing luminosity.

abundances. This method only works for sources with strong iron UTAs, such as IRAS 13349+2438 and NGC 3783. For other sources ions from other elements have to be included as well, so relative abundances start to play a role. It is not straightforward to determine the correct AMD. One has to define the number of bins in which the AMD is evaluated and the bins can be highly correlated, possibly leading to large errors. Nevertheless this is the best method to study the structure of the outflow. Two important results showed up from this analysis. First, the AMD of all outflows studied appears to have a very flat distribution (Behar 2009). Second there are minima in the AMD distributions for certain ranges of ξ. The current theory is that thermal instabilities are responsible for these minima. If the gas is thermally unstable at a certain temperature (because it is on an unstable branch of the cooling curve, see Fig. 1.5), we will not observe any gas with ξ values that correspond to that temperature.

Recently it was shown that density profiles could be derived from the AMD (Behar 2009). It was found that for both large scale and small scale density gradients, the density drops of approximately as r^{-1}. This rules out a spherical, mass-conserving outflow or a constant density absorber. By combining these density profiles with limits on the location of the outflow for different values of ξ (as obtained from

variability studies), the location as a function of ξ can be obtained in principle (in the case of a large scale density gradient). One must be careful in applying this method however, as the actual situation is most likely a combination of local and large scale density gradients, which complicates the distance estimates. By combining the X-ray data with the UV data, local density gradients can be determined if the X-ray and UV components have the same outflow velocity. As components with the same outflow velocity are very likely to be co-spatial as well, the difference in ξ for the UV and X-ray gas should originate in differences in densities. Combining this information again with variability studies to put constraints on the exact distance, a two−dimensional picture of the outflow can be obtained. This requires excellent, high signal to noise, multi-wavelength spectra, so this method is unfortunately limited to only a handful of sources at the moment. For an alternative view on this method in the case of discrete components (where this method does not work), see Chapter 2.

1.4.8 Connection to emission lines

The connection of the outflow to the different emission line regions (BLR and NLR) is currently not fully established. The narrow emission lines seen in X-ray spectra typically do not show any blueshifts, except for some sources. This could be because the NLR is not connected at all to the outflow, or because of the geometry of the NLR (for emission, the line profiles are integrated over the whole NLR, including the parts which are redshifted, resulting in no significant blueshift). In Type 2 AGN the X-ray NLR is in the shape of a cone (the so-called ionization cone, which contains gas ionized by the AGN) and in some cases blueshifts are observed. Also the ionized species of the emission and absorbing gas are similar (with O VII usually being the dominant absorption and emission feature).

The main problem however is that the location and geometry of the outflow are poorly constrained in almost every source. In the cases (such as the sources discussed in this Thesis) where we do have a constraint on the location of the outflow, that constraint is not tight enough to allow us to differentiate between an origin of the outflow in either the BLR, the inner edge of the torus or the NLR. In most Type 1 AGN, the bright continuum also prevents us from observing many emission lines, while in Type 2 AGN the outflows are not observed due to a non-favorable line of sight. The best method to investigate the connection between the outflows and the emitting gas is to perform photoionization calculations for the different geometries, ionization states and distances of the absorbing / emitting gas and then compare the results to the observations. This has not been done so far, as it is a very time consuming task, but currently it is the only viable way forward.

1.4.9 Ultrafast outflows

Recently, ultrafast outflows ($\geq 10\,000$ km s^{-1}, UFOs) have been reported in the X-ray spectra of several QSOs and Seyfert galaxies (Pounds et al. 2003, Reeves et al. 2003, Ponti et al. 2009, Tombesi et al. 2010a, Kaspi & Behar 2010). These outflows are

generally detected in the Fe−K region (around 6.4 keV) in blueshifted absorption lines of Fe Kα indicating the presence of highly ionized gas outflowing at large velocities. These outflows are very interesting as due to their large velocities they could potentially have a large impact on the feedback. If these outflows are indeed real then their outflow velocities rule out the torus as the origin. They would have to be either radiatively or magnetically driven outflows originating very close to the nucleus. Whether these outflows are connected to their low velocity counterparts (the 'traditional' warm absorber) is unclear. The main problem with these features is that they are marginally significant (2−3 σ) and appear to be transient (Kaspi & Behar 2010, Vaughan & Uttley 2008). Also one would like to see these outflow velocities in more than one ion and or transition, so that the features can be properly identified (which is difficult to do with only one absorption line, as the outflow velocity is not known a priori). If these features are transient, then they could be short lived ejections of gas from the accretion disk and will not have a major impact on feedback. From all the research done on these UFOs, firm proof is still lacking. Only with high−resolution, high−throughput instruments (such as those on ASTRO-H) will this issue be solved.

1.4.10 Outflows and feedback

There are two main feedback effects of AGN outflows. One is the chemical enrichment of the ISM / ICM, for which the mass loss rate is the most important. The other is the deposit of kinetic energy into the ISM, preventing star formation and regulating the growth of the black hole. Although the exact mechanism by which the outflow deposits its internal energy is not exactly known, estimates place the energy needed for feedback to be effective between 0.5 % and 5 % of the total bolometric luminosity of the AGN. One scenario is that the AGN outflow has enough energy to blow the ISM and dense clouds of cold gas out of the galaxy, but the amount of energy required would mean that only the strongest outflows could do this.
Another more recent scenario is that of a two-stage wind, in which the outflow drives a hot ISM wind (Hopkins & Elvis 2010). In this way a less powerful wind can also have strong feedback effects. In almost all cases the kinetic energy of the ionized outflows in nearby Seyfert galaxies is negligible (Costantini 2010). This is mainly due to the low outflow velocities, as compared to the BAL−QSOs. Their kinetic luminosities are orders of magnitude less than the bolometric luminosities of the AGN. However their mass outflow rates can be significant, between 0.1 and 1 $M_\odot$ yr^{-1}. This means that they can still play an important role in the enrichment of their host galaxy.
An important note however is that these estimates are highly uncertain. The distances are still not known (only upper limits exist), their geometry is unknown and the possible existence of ultrafast (10000s of km s^{-1}) outflows in some of the sources can change the estimated feedback parameters quite significantly.

1.5 Variability

All Type 1 AGN are highly variable (Type 2s are as well, but we do not observe the continuum directly, so we leave them out of the discussion here). Depending on the energy band (X-ray, UV, Optical, IR) the continuum emission varies on timescales ranging from minutes to days. On top of that there are also variations on a longer timescale, most likely related to variations in the accretion rate. The amplitude of the variability seems to be inversely proportional to the source luminosity (and therefore also to the black hole mass).

The variability of AGN can be used to probe the inner regions, which are unresolved with our current Opt, UV and X-ray telescopes. A clear example of using this variability to probe the geometry is the reverberation mapping of the BLR (see Sect. 1.2). Another good example is using the correlations between UV, Opt and IR fluxes and the time delays between variations in different bands to locate the inner surface of the dusty "torus" (Suganuma et al. 2006). This method has actually shown that the dust is located much closer to the central engine than previously thought, almost by an order of magnitude (less than 0.1 pc). Variability is actually the main method which can be used to determine the geometry of not just the optical BLR gas, but also the NLR, and the locations of the outflow. The gas surrounding the central source will respond to continuum variations on different timescales depending on the physical conditions (density, ionization state) and location of the gas.

Also the outflows seen in AGN are not static. Depending on the ionizing flux they receive from the central source, they can change their ionization state and become less or more ionized. In other cases the absorption is seen to move in front of the central source, causing a dip in the observed continuum flux, similar to an eclipse. It is exactly this variability that we can exploit in order to obtain crucial information on the density, location and structure of the outflow. Therefore multi−epoch observations of a single AGN are crucial. Monitoring AGN is very important, as it is the only method at the moment to obtain the locations of the outflows (at least in the X-ray regime, in the UV density diagnostics can sometimes be performed using excited states of C III).

There are two important timescales related to variability studies. The first is the more well-known light-travel time. This is the timescale by which light from the continuum source travels to the emitting gas (see Fig. 1.6 for a sketch). What we observe is the average response of the whole emitting region, and so the light travel time depends on the geometry of the emitting region as well as the distance to it.

For emission components, both these timescales play a role, as the light first has to travel from the central source to the emitting gas, then the gas responds to the new ionizing flux and then finally travels to the observer. Therefore the total response time $\tau_{\rm var} = \tau_{\rm lt} + \tau_{\rm rec}$. In the case of the outflows, there is no light travel time delay, as we only observe the outflow along our line of sight. So for the outflows, only the recombination time $\tau_{\rm rec}$ is important.

By observing an AGN multiple times during a certain period (usually years), we can investigate if the spectral properties have changed over time and put constraints

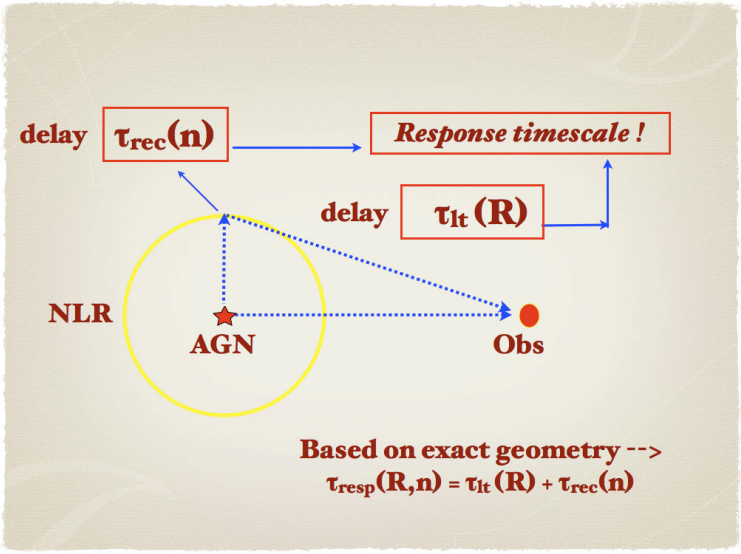

Figure 1.6: A sketch of how the response timescale of emission lines is defined.

on the timescale of any observed variations. We ignore here the case of movement of gas components in and out of the line of sight, which is independent of any continuum variability. If the gas changes its ionization state from one observation to the other, the time between those observations gives us an upper limit to the recombination / ionization timescale (as generally we only know that the gas changed in ionization state somewhere between those observations). Therefore by measuring an upper limit to the recombination timescale, we can determine a lower limit to the density of the gas and thus an upper limit to the distance R of the gas (see eq. 1.2).

1.5.1 Time-dependent ionization

The current models we use to determine the ionization balance of the absorbing gas assume that the gas is in ionization equilibrium. This is a valid assumption if the density of the gas is high, so that the recombination timescale is small or if the changes in the ionizing flux are small. As we do not know the density a priori, this assumption might be and probably is indeed flawed. There are several effects that play a role with time−dependent models :

- Delayed and smoothed response of the absorbing gas to continuum variations
- Over−ionization of the absorbing gas if subjected to frequent, consistent changes in the ionizing luminosity
- Different elements may or may not all be in ionization equilibrium

In almost all cases the ionization timescale ($\tau_{\rm ion} \sim 1/F_{\rm ion}$) is much shorter than the recombination timescale ($\tau_{\rm rec} \sim 1/\alpha_{\rm rec} n_{\rm e}$). Due to the delay of the absorbing gas, the time behavior of the absorbing gas can be opposite to that of the continuum.

Testing whether the absorbing gas is in equilibrium is not an easy task. In most cases the timescale between multiple high resolution X-ray observations of a single AGN can be months or even years. Without a good handle on the continuum variability in between observations (by using X-ray monitoring satellites such as *RXTE*), the full history of the continuum flux remains unknown. On the other end of the spectrum, we have the rapidly and drastically changing NLS1 galaxies. In some of these sources (such as NGC 4051), the flux varies by an order of magnitude in a matter of hours. Obtaining a high quality high resolution spectrum in such a short time is not feasible with the current technology. Using CCD−type instruments with a large effective area (such as EPIC−pn) to probe changes in the absorbing gas is feasible only if an accurate model of the ionized outflow, including ionization structure, has been obtained from high quality, high resolution data. Without this accurate description, identifying which of the ions are responsible for the observed changes is not possible and a correct determination of the density can not be obtained.

1.6 Feedback

The exact nature of AGN feedback is currently one of the major unsolved topics in astronomy. Over the last decade it has become clear that the evolution of the AGN and its host galaxy (and also on larger scales) are tightly connected. The most extreme examples of this interaction between the AGN and its environment are the X-ray cavities seen in clusters of galaxies (see e.g. Fabian et al. 2006, Rafferty et al. 2006, McNamara & Nulsen 2007). These are thought to be powered by a relativistic jet from the central AGN. The energy deposited by these jets during one activity cycle of the AGN (several 10^7 years) can be on the order of 10^{54} J (McNamara et al. 2009). This energy heats up the gas between the galaxies and prevents it from cooling, thus solving the 'cooling flow problem' in clusters of galaxies (Peterson et al. 2001, Tamura et al. 2001).This is the problem that we expect the cores of clusters to contain a lot of cool gas, which is not what was observed by the Reflection Grating Spectrometer (RGS) on board of the *XMM-Newton* satellite. It was one of the main surprising results found with the new high resolution X-ray gratings.

Another example of AGN feedback is the so-called M - σ relation (Gebhardt et al. 2000, Ferrarese et al. 2001). This is the relation between the velocity dispersion of stars in the stellar bulge and the mass of the SMBH (see Fig. 1.7). This relation is one of the key proofs that the evolution of the AGN and the host galaxy are connected. The mass of the SMBH is always on the order of 0.1 % of the mass of the bulge. Somehow the black hole knows about the bulge of the galaxy and vice versa. The most likely cause of this connection are AGN outflows regulating the growth of the black hole and the star formation in the bulge. At the same time the star formation in the center of the galaxy controls the amount of gas that is available for accretion, as stellar

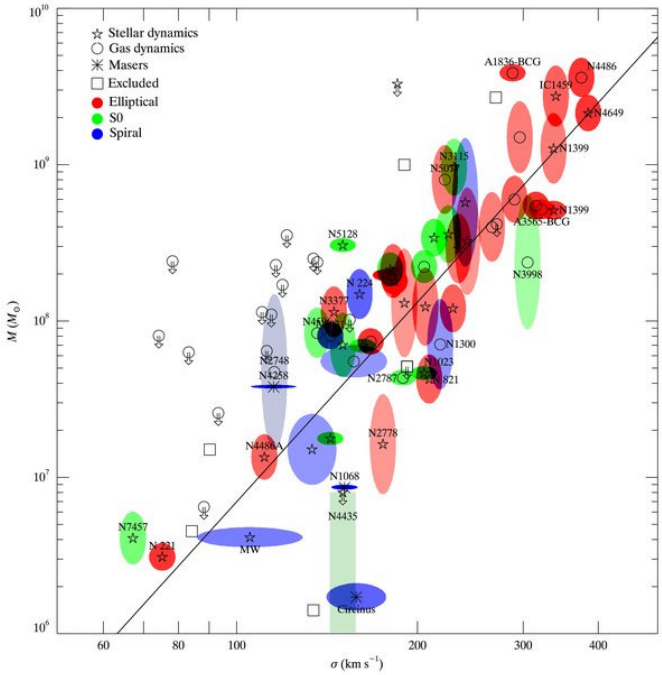

Figure 1.7: The M $-$ σ relation for a sample of nearby AGN (Gültekin et al. 2009). The colors indicate the type of host galaxy; elliptical (red), S0 (green) or spiral (blue). The symbols indicate by which method the black hole masses were obtained; stellar dynamics (pentagrams), gas dynamics (circles) or masers (asterisks). Sources marked by a rectangle are excluded in the fit.

winds and supernovae blow the surrounding gas to the center of the galaxy, where it is accreted unto the black hole. The idea is that when a starburst occurs in the bulge of a galaxy (through galaxy mergers for example), stellar winds and supernovae blow away a lot of gas towards the black hole, beginning the active phase of the AGN. Eventually an outflow develops, which sweeps away the surrounding gas and dust and switches off star formation by heating the gas in the bulge. This way the bulge and the SMBH grow steadily, regulated by the feedback of the AGN. This process can repeat itself over the lifetime of the AGN and its host galaxy, as there can be multiple episodes of AGN activity.

It seems that AGN can play a major role in the evolution of their host galaxy and also on the scale of whole clusters of galaxies. There has been a large effort into investigating and understanding the origin and effects of AGN feedback in the last decade. Major questions that are still unresolved are:

- How do AGN turn on and off ?
- Are radio-loud AGN a different population or is it a different phase of the AGN

life ?

- How can we link the different spatial scales (i.e. from kpc scale to the sub-pc scale close to the black hole) ?
- Are the ionized outflows seen in Seyfert 1 galaxies (i.e. warm absorbers) capable of influencing their host galaxy ?

Although we now know that AGN outflows can have an effect on the Inter Stellar Medium (ISM) and Inter Galactic Medium (IGM) of their host galaxy, exact outflow rates or total thermal luminosities are still unknown in most cases. We also do not know how the outflow interacts with its environment. Only detailed multiwavelength studies of AGN outflows can increase our understanding of the exact physics which occur in these outflow and where and how they are formed. The basic quantities that we need to know to asses whether or not these outflows can affect their host galaxy are:

- The mass outflow rate $\dot{M}_{out}$
- The total internal luminosity L_{int}

By analyzing UV and X-ray spectra of the outflows, we try to determine the mass outflow rates and the internal luminosities. Both quantities depend on the exact geometry of the outflow however, which we do not know and at the moment still is model dependent. If we assume that the outflow is bi-conical, then the mass outflow rate can be defined in the following way (see Krongold et al. 2007, there is a factor of 2×1.23 missing, for which we have corrected):

$$\dot{M}_w = 1.97\,\pi\, m_p\, N_H\, v_r\, R\, f \tag{1.3}$$

Here $\dot{M}_w$ is the mass outflow rate, m_p the proton mass, N_H the hydrogen column density, v_r the outflow speed, R the distance from the central source and f a factor of order unity that depends on the line of sight with respect to the wind. The total internal luminosity is then simply:

$$L_{int} = \frac{1}{2}\,\dot{M}_w\, v_r^2 + L_{therm} \tag{1.4}$$

In most cases, as the gas is photoionized, the thermal energy will at most be on the order of the kinetic energy. It is very difficult to obtain accurate estimates for these quantities. In most cases the distance is only properly constrained for one component, or for a few ions. What is really needed are accurate distances for every ionization component of the outflow as well as accurate outflow velocities and filling factors. In addition constraints on the geometry of the outflow are crucial. These quantities can only be obtained by multiple, high quality, high-resolution UV and X-ray observations of a single AGN. Without accurate constraints on these quantities, the mass outflow rate and total internal luminosity remain free knobs to turn in the simulations. This is the key step to increase our understanding on AGN feedback. But in order to answer all these questions, we first need to describe how the AGN environment looks like.

1.7 This Thesis

This Thesis focusses on combining variability and high-resolution X-ray spectroscopy to locate the ionized outflow and X-ray NLR gas in several sources. The main reason to do this is that these quantities are crucial for obtaining the geometry of the inner region of these AGN and consequently also for determining the strength of the feedback in these sources (the mass outflow rate for example). The topics covered in this Thesis are the following:

- Calibration of the instruments remains an important issue, more so now that higher quality spectra are becoming available. Accurate cross-calibration of the European Photon Imaging Camera CCD (EPIC−pn) and RGS was needed to improve simultaneous fitting of both spectra. This we did as the goal was to measure small changes in the ionized outflow of Mrk 509 between three different observations. As shown in 2 we have managed to improve the cross−calibration down to 4 %. Simultaneous fitting of both EPIC-pn and RGS spectra showed changes in the highest ionization component of the outflow on the timescale of half a year. This constrained the location of this component to within 0.5 pc form the central source. Updates to the Scientific Analysis Software (SAS) have now been made to include a similar model for the cross-calibration.

- Mrk 509 has been the target of a large multi-wavelength campaign in 2009. The goal of this campaign is to locate the outflow and to obtain the ionization, velocity and density structure of the outflow. Chapter 3 focusses on the stacked 600 ks RGS spectrum in order to obtain an accurate description of the outflow, which is needed for the goal of the campaign (i.e. reverberation mapping of the outflow on a timescale of 4 days). Due to the high quality spectrum and the accurate column densities obtained for all ions, for the first time it has been shown clearly that the outflow does not consist of a continuous distribution, but is made up of discrete components (up to 6 in total). We also have found indications of an outflow velocity increasing with the ionization parameter. Further papers in the series will deal with obtaining a two-dimensional picture of the outflow including distances and comparisons to models.

- Comparing two *Chandra* LETGS observations of the Seyfert 1 galaxy, NGC 5548, in Chapter 4 we have detected clear evidence of recombination of the ionized outflow. Using the long term *RXTE* light curve, to constrain the timescale of the recombination, we have constrained the location of the ionized outflow to within 7 pc.

- Using the same observation, we also for the first time observed variability in the X-ray narrow emission lines. From the observed timescale of the variability, in Chapter 5 we have constrained both the geometry and location of the X-ray NLR in NGC 5548. Extending this work to other Type 1 AGN, using the archives of *XMM-Newton* and *Chandra*, in Chapter 6 we searched for other sources with

variable X-ray narrow emission lines, but the low quality of the spectra or systematic uncertainties in either the continuum or absorption prevented any claim of significant variability. Future photoionization modeling of the X-ray NLR in these systems, may constrain the location and geometry as well as the connection to the ionized outflow.

Chapter 2

The outflow in Mrk 509. A method to calibrate *XMM-Newton* EPIC-pn and RGS

R.G. Detmers, J.S. Kaastra, E. Costantini, F. Verbunt, M. Cappi and C. de Vries

Published in Astronomy & Astrophysics, volume 516, A61, 2010

2.1 Abstract

We analyzed three *XMM-Newton* observations of the Seyfert 1 galaxy Mrk 509, with the goal of detecting small variations in the ionized outflow properties. Measurements such as these are limited by the quality of the cross-calibration between RGS, the best instrument for characterizing the spectrum, and EPIC-pn, the best instrument for characterizing the variability. For all three observations we are able to improve the relative calibration of RGS and pn consistently to 4 %. In all observations we detect three different outflow components and, thanks to our accurate cross-calibration, we are able to detect small differences in the ionization parameter and column density in the highest ionized component of the outflow. This constrains the location of this component of the outflow to within 0.5 pc of the central source. Our method for modeling the relative effective area is not restricted to just this source and can in principle be extended to other types of sources as well.

2.2 Introduction

Active Galactic Nuclei (AGN) outflows are thought to play an important role in feedback processes, that connect the growth of the black hole to the growth of the galaxy (Di Matteo et al. 2005). However, the strength of these outflows (kinetic luminosity) is unknown without knowing their precise distance from the central source. In the UV density sensitive line diagnostics have been used to constrain the density of the outflowing gas, hence also the distance (Gabel et al. 2003). Attempts have been made to do the same in the X-ray regime (Kaastra et al. 2004), but these results were affected by large uncertainties; therefore, currently the best way in the X-ray band to determine the distance of the X-ray outflows is by using variability combined with high-resolution X-ray spectroscopy to constrain the density of the gas, and then use this constraint to put an upper limit to the distance R. The main challenge with this approach is that it requires several crucial ingredients:

- high-resolution X-ray spectroscopic observations to determine the ionization state, column densities, and outflow velocities of the warm absorber;
- multiple observations of the same source;
- a source that varies on a suitable timescale and changes significantly in ionizing flux or in warm absorber properties.

If the source varies too fast, then it becomes difficult to obtain the time-resolved spectra suitable to ionized outflow studies. If the changes in ionizing flux are small, then detecting changes in high-resolution X-ray data is very difficult. There are several sources for which the variability approach has been successful, but all have difficulties or large changes in flux. The *Chandra* data of NGC 3783 (Netzer et al. 2003, Krongold et al. 2005) were spread out over several months (with distance limits between 0.2 and 25 pc), while the *XMM-Newton* observations of this source (Behar et al. 2003) occurred during a gradual rising phase without clear flux extrema, with no changes in the absorber properties leading to a minimum distance of 0.5 - 2 pc from the source, depending on the ionization component. In NGC 4051 the flux dropped by a factor of five (Steenbrugge et al. 2009) leading to a 0.02 - 1 pc upper limit on the location of the absorbing gas. For NGC 5548 there was a 3-year gap in the observations Chapter 4, and the flux changed by a factor of five in the soft (0.2−2 keV) band, which resulted in an upper limit of 7 pc to the location of the warm absorber. Also in NGC 3516, variability was used to constrain the location of the ionized outflow (less than 0.2 pc from the source Netzer et al. 2002), but the flux change was very large (50 at 1 keV).

In principle, the *XMM-Newton* EPIC-pn instrument (Strüder et al. 2001) combined with the *XMM-Newton* Reflection Grating Spectrometer (RGS, den Herder et al. 2001) can be used to detect small changes in the column density of the ionized outflow. The RGS spectrum gives the detailed warm absorber structure, such as outflow velocity, velocity width, and ionization state. With its larger effective area, EPIC-pn can detect

Table 2.1: Mrk 509 Observations.

Obs	Date	Obsid	Duration (ks)	Exposure RGS[a] (ks)	Exposure pn[a] (ks)	Flux[b] (W m^{-2} s^{-1})
1	18-10-2005	0306090201	86	85	58	7.1×10^{-14}
2	20-10-2005	0306090301	47	47	32	7.2×10^{-14}
3	24-04-2006	0306090401	70	67	43	8.1×10^{-14}

[a] Effective exposure time after filtering.
[b] The flux is given for the pn 0.2−10 keV band.

small variations in the column density in response to small changes in the continuum flux. This requires that the relative calibration between EPIC-pn and RGS is better known than the observed variations in the column density and ionization parameter.

To this end we have analyzed three different observations of the bright Seyfert 1 galaxy Mrk 509 (z = 0.0344, $N_{\rm H} = 4.4 \times 10^{24}$ m^{-2}, Fisher et al. 1995, Murphy et al. 1996), taken by *XMM-Newton* EPIC-pn and RGS, during different epochs in order to search for any variability in the outflow. We investigate whether we can model the relative calibration between EPIC-pn and RGS in a consistent way, so as to take it into account when fitting the EPIC-pn and RGS spectra simultaneously. If successful, this approach allows for variability studies of weakly varying AGN, enabling us to also constrain the outflow location in these sources. Additionally, this approach can be extended to other types of sources as well, as the method itself is source independent even though the exact model of the relative calibration will depend on the source type. We stress that it is also important to consider that the calibration of the instruments (e.g. effective area) has changed in time.

Mrk 509 has been observed with high-resolution gratings before, namely in 2000 and 2001 by *XMM-Newton* (Pounds et al. 2001, Page et al. 2003) and *Chandra* HETGS (Yaqoob et al. 2003). Smith et al. (2007) (hereafter S07) re-analyzed the RGS data of 2000 and 2001, and found evidence of three warm absorber components, as well as broad and narrow emission lines. We use this study as a starting point for our analysis of the three new observations taken in 2005 and 2006. Using these data, Cappi et al. (2009) found evidence of a highly ionized and mildly relativistic outflow. Clearly, Mrk 509 is an excellent source to investigate in further detail.

The most recent calibrations of the RGS and pn instruments (see Kaastra et al. 2009, for the RGS) show that the uncertainty in the effective area of the RGS can be reduced to 3 %, while the pn absolute effective area calibration has an accuracy of 10 %[1]. Our aim is to obtain a more accurate relative calibration for RGS and pn.

Section 2.3 describes the data reduction we have applied to all three observations. In Sect. 2.4 we describe the method we used to determine the cross-calibration differences between pn and RGS and how we model these. In Sect. 2.4.5 we present the results we obtained for the cross-calibration. Section 2.5 contains the spectral analysis of all three spectra. We discuss our results in Sect. 2.6 and present our

[1] http://xmm2.esac.esa.int/docs/documents/CAL-TN-0018.pdf

conclusions in Sect. 2.7.

2.3 Data reduction

The log of the three observations of Mrk 509 that we used is given in Table 2.1. We used the SAS 9.0 software package to reduce all the data. We only used these three observations, because the S-N ratio of the first two RGS observations (SN of 3 and 4 in the 7−38 Å respectively) is too low for this study owing to a high background level. The S-N ratios of the three observations are 9, 7, and 8, respectively. We did not use the MOS data, which are affected by pile-up and therefore their useful part has a lower S−N ratio as compared to the pn data.

For the RGS spectra we use the *rgsproc*[2] task with the source coordinates as obtained from SIMBAD[3] (α = 311.04067 degrees, δ = -10.72353 degrees). After checking the background lightcurve for possible flaring intervals (observation 3 had one event with background level 0.25 cts/s and observation 5 had two events with background 0.4 cts s^{-1}, the mean net source count rate being on average 2.8 cts s^{-1}), we determined the good time intervals and rerun the *rgsproc* task now with the good time intervals selected (using a cutoff of 0.1 cts s^{-1} in the background lightcurve) and also with the *keepcool* keyword set to *no*, so cool pixels were also rejected. We also stacked all three observations with the *rgscombine* task for both RGS1 and RGS2 in order to compare the results of the three individual observations with the stacked spectrum.

The OM data were used to obtain fluxes in the UV band, which were used, along with the pn data, to construct the spectral energy distribution (SED) of Mrk 509. The fluxes in the UVW2, UVW1, and UVM2 filters were obtained by extracting the magnitudes from the PPS products of the OM data. These were then corrected for the extinction due to the Galactic absorption towards the source, using the relation between $N_{\rm H}$ and $A_{\rm V}$ from Predehl & Schmitt (1995) and the relation between A_λ and $A_{\rm V}$, as given by Cardelli et al. (1989)

All the pn data were taken in small window mode with a thin filter. The background lightcurves were checked for flaring intervals, and the good time intervals were determined to produce a filtered dataset. For the pn data we first checked for possible pile-up effects. Using the *epatplot* task, we analyzed the number of single and double events and found no signs of pile-up in our spectra. We also checked for X-ray loading, which can occur even when the countrate is below the pile-up limit. X-ray loading is the inclusion of X-ray events in the pn offset map which is produced at the start of the observation. This leads to additional and incorrect offset shifts for pixels where the X-ray loading occurs. All events in the subsequent observation associated with that pixel will be shifted to lower energies, depending on the energy of the incoming X-ray photons. A more detailed description can be found in the EPIC calibration online documentation, document TN-0050[4]. To counteract the effects of

[2]http://xmm.vilspa.esa.es/sas/8.0.0/doc/rgsproc/index.html
[3]http://simbad.u-strasbg.fr/simbad
[4]http://xmm2.esac.esa.int/docs/documents/CAL-TN-0050-1-0.ps.gz

X-ray loading, we excluded the central region from our analysis. We therefore took an annular extraction region centered on the source with an inner radius of 50 (2.5 arcsec) and an outer radius of 600 (30 arcsec) in detector coordinates. The background was extracted from an annulus of the same size outside the source region and avoiding out of time events. We used the SPEX[5] spectral fitting package (Kaastra et al. 1996) and C-statistics for fitting the spectrum. The errors were calculated for $\Delta C = 1$.

2.4 The relative calibration between pn and RGS

2.4.1 Setup

We only use data between 0.32 keV and 1.77 keV (this corresponds to the RGS band, i.e. 7−38 Å). We follow a method in four steps, as explained below, to determine the cross-calibration between pn and RGS. We first fit a model spectrum to the RGS data. All model parameters are frozen, and the model is then applied to the pn data. The ratios of predicted to observed pn count rates are then modeled to determine the relative calibration between RGS and pn. The last step is to do a simultaneous fit of both the pn and RGS spectrum, taking the relative calibration, i.e. into account. As an additional check we created a fluxed RGS spectrum of each observation and follow the same procedure as above.

2.4.2 Spectral Models

We model all RGS spectra with a power law and blackbody component, absorbed by three photoionized components that are modeled with the *xabs* model of SPEX. The cosmological redshift and Galactic absorption are also taken into account. Broad emission lines are modeled with a Gaussian line profile, narrow emission lines with a delta line profile. The flux at earth f_λ may then be written as

$$\begin{aligned} f_\lambda &= \left(R(z) \otimes \left(f_{\rm PL}(F_{\rm PL}, \Gamma_{\rm PL}) + f_{\rm MBB}(F_{\rm MBB}, T_{\rm MBB}) + \sum_{i=1}^{2} G_i(F_i, \lambda_i, \sigma_i) \right.\right. \\ &+ \left.\left. \sum_{\Delta=1}^{1} f_\Delta(\lambda_\Delta, F_\Delta) \right) \times \prod_{j=1}^{3} X_i(N_j, \xi_j, v_j, \sigma_j) \right) A(N_{\rm H}). \end{aligned} \tag{2.1}$$

We normalize the fluxes of the various components by their total flux in the RGS band. The power law $f_{\rm PL}$ is described by a normalization $F_{\rm PL}$ and a slope $\Gamma_{\rm PL}$, while the MBB $f_{\rm MBB}$ is described by a normalization $F_{\rm MBB}$ and an effective temperature $T_{\rm MBB}$ (see Table 2.3). Each broad emission line $G_{\rm i}$ is characterized by a normalization F_i, central wavelength λ_i, and width σ_i, while the narrow line f_Δ is characterized by a normalization F_Δ and wavelength λ_Δ. Each absorption component X is characterized

[5] http://www.sron.nl/spex

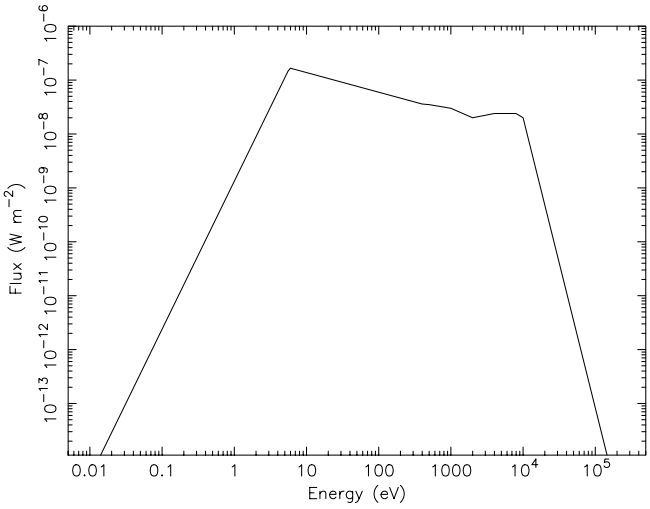

Figure 2.1: The SED used for the Mrk 509 observations.

by a hydrogen column density N_j, ionization parameter ξ_j, outflow velocity v_j, and Gaussian velocity broadening σ_j. The effect of cosmological redshift R depends on redshift z. The galactic absorption A depends on the hydrogen column density $N_{\rm H}$.

The widths σ_i of the two broad emission lines are kept fixed to the values determined from the optical observations, and the central wavelengths λ_i are fixed to the laboratory wavelengths (see Table 2.4). The high wavelength resolution of the RGS requires a detailed description of the wavelength dependence of the interstellar absorption. For this reason we use the SPEX model *hot* with a fixed low temperature $kT = 5 \times 10^{-4}$ keV and fixed column density determined in earlier observations $N_{\rm H} = 4.4 \times 10^{24}$ m^{-2} (Sect 2.2).

The ionization states ξ_j of the photoionized absorbers depend strongly on the assumed SED involved (Chakravorty et al. 2009). We constructed the SED from the Mrk 509 observations, using the pn and OM data to obtain the necessary flux points. The SEDs of the three observations are almost identical, so we use the SED obtained from the first observation. The photoionization balance calculations needed for our spectral modeling were based on this SED and performed using version C08.00 of Cloudy[6] (an earlier version is described by Ferland et al. 1998). The SED used is shown in Fig. 2.1.

[6]http://www.nublado.org/

2.4.3 Method 1

The first step is to obtain an accurate RGS fit for each observation. This is done by fitting the spectral model described in the previous subsection (see Eq. 2.1) to the RGS data. The second step is that we use this fit with all parameters fixed to predict the count rate $C_{\rm M}(PI)$ in the pn. We then compare these with the observed $C_{\rm O}(PI)$ count rates in the pn by computing

$$R(PI) = \frac{C_{\rm O}(PI)}{C_{\rm M}(PI)}. \tag{2.2}$$

The resulting values for $R(PI)$ are plotted in Fig. A.2.

As the third step we calculated these ratios $R(PI)$ using the SPEX model *knak F*. This is a piecewise broken power law, which consists of hinge points (λ_1, λ_2, ... ,$\lambda_{\rm k}$) and the corresponding transmission values (t_1, t_2, ..., $t_{\rm k}$). We choose the hinge points by eye for the first observation, and keep these fixed for all other observations. The transmission values t_i are then fitted to the ratio R for each observation, leading to the values shown in Table 2.2.

At this point we check the *knak* model F as follows: we compute $F \times f_\lambda$ and fold the result through the response matrix of the pn to predict the model count rate, and compare this with the observed pn count rate. Systematic deviations would indicate that the *knak* model must be revised, e.g., by redefining the λ_k. We find that the *knak* model given in Table 2.2 does not produce such systematic deviations (see Fig. A.1).

Once we have a model F for the cross-calibration, we can fit the simultaneous RGS + pn spectrum. This is the fourth and final step. We create two sectors in SPEX, so that we can have two sets of models for the pn and RGS datasets, namely f_λ for the RGS and $f_{\rm pn} \equiv F f_\lambda$ for the pn. We then couple the model parameters in such a way as to take advantage of the strengths of each instrument. We let the RGS spectrum determine the high-resolution features, such as the fluxes F_i and F_Δ of the emission lines and the outflow velocity v_j and velocity broadening σ_j of the ionized absorbers. This is because pn does not have the resolution needed to accurately determine the detailed structure (broadening + outflow velocity) of the outflow. The pn spectrum determines the parameters of the PL and MBB and the column densities N_j and ionization parameters ξ_j of the ionized absorbers (*xabs*). The resulting values are shown in Tables 2.3, 2.4, and 2.5, together with the values of the fixed parameters.

We use this four step procedure for each observation, including the stacked one.

2.4.4 Method 2

As an independent check for each observation, we use the best-fit model f_λ for each observation to predict the RGS count rate $C_{\rm RGS}$ and compute the model flux to be used for the pn f_{pn} by multiplying f_λ with the ratio of the observed to predicted RGS count rates $\frac{C}{C_{\rm RGS}} \times f_\lambda$. We then predict the pn count rate by folding f_{pn} through the corresponding pn response matrix and compare the result with the observed count rate. This procedure makes certain that any (time-dependent) astrophysical

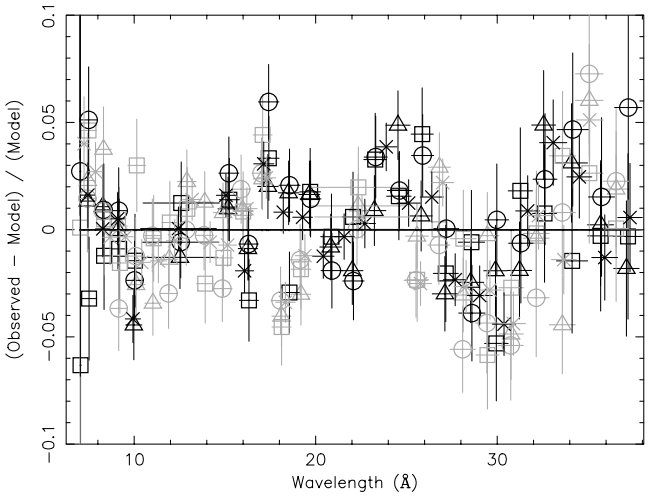

Figure 2.2: Broad band RGS fit residuals for all observations. RGS1 data points are indicated by the black symbols, while RGS2 data points are indicated by the gray ones. The different observations are marked by separate symbols: triangles for observation 1, squares for observation 2, circles for observation 3 and, crosses for the stacked spectrum.

modeling problems are taken care of, and the end result will be the pure cross-calibration residuals. We then compare the cross-calibration residuals we obtain with this method with the first method to see whether the results are consistent (see Fig. A.2).

2.4.5 Further checks

To investigate the relative calibration further, we checked for the presence of any weak deviations that might bias our RGS fit but would escape attention at full spectral resolution. Figure 2.2 shows the residuals in the RGS band after rebinning the spectrum with a factor of 100. The typical residual fluctuations are at the level of 3−4%. The third observation shows a discrepancy between the two RGS spectra. The RGS1 data points are consistently below the RGS2 points, with a difference of about 2 %. This will have an effect on the total RGS flux, which we discuss later in more detail.

Focusing on the pn spectrum, we loaded the best fit RGS model into the corresponding pn data set. If the relative calibration were perfect, then the resulting fit quality of the pn spectrum should be the same as for the RGS-only fit. Instead we found something different. The resulting residuals are shown for each observation

Table 2.2: *Knak* model parameters for the cross-calibration residuals, where a value lower than 1 means the RGS flux is higher than the pn flux.

λ (Å)	1	2	3	stacked
7	0.97±0.01	1.00±0.01	0.98±0.01	0.99±0.01
13	0.98±0.01	0.97±0.01	1.01±0.01	0.98±0.01
15	0.94±0.01	0.97±0.01	0.97±0.01	0.96±0.01
19	0.96±0.01	0.98±0.01	0.98±0.01	0.97±0.01
23	0.87±0.01	0.92±0.01	0.91±0.01	0.90±0.01
28	0.92±0.01	0.94±0.01	0.91±0.01	0.92±0.01
34	0.79±0.02	0.78±0.02	0.81±0.02	0.80±0.01
37	0.90±0.03	0.92±0.03	0.94±0.03	0.91±0.02

in Fig. A.2. RGS and pn agree with each other within 1−4% below 20 Å. Above 20 Å the RGS flux is on average 8−10% higher than the pn flux. All three observations and the stacked spectrum are in agreement with each other (apart from small fluctuations on the level of 2 %).

As mentioned earlier, we modeled these calibration offsets by a *knak* component. The best-fit parameters of this component are shown in Table 2.2. When applying this correction to each pn observation, the fit improves dramatically. The resulting residuals are shown in Fig. A.1. Some fluctuations on the order of 2 % can still be seen in the individual spectra, but our model adequately corrects for the large-scale offsets. We chose the hinge points by eye and fixed them for all other observations. The locations of these hinge points were chosen such that they follow the trend visible in the pn residuals (see Fig. A.2 in the Appendix). If we instead use a different number of points (e.g. 7 points, with fixed 5 Å spacing from 7 to 37 Å), the residuals in Fig. A.1 change by no more than 1−2 %. We also performed additional tests with only 5 equidistant hinge points and the results are similar.

Thus having obtained a model for the relative calibration for each observation, we performed a simultaneous fit of both the pn and RGS spectra, with the relative calibration differences taken into account by our *knak* model.

2.5 Spectral Analysis

2.5.1 Continuum

We have modeled the continuum for all spectral fits with a power law and a modified blackbody component. For all three observations and the stacked spectrum the continuum model parameters are shown in Table 2.3. If we instead only use a power law to model the continuum as in S07, the fits for all three observations are worse by $\Delta C = 75$ per d.o.f. Using only the power law as a continuum has a slight effect on the absorption components, as the power law slope is softer in this case ($\Gamma = 2.6$ instead of 2.3). However, given the large change in ΔC, we used the continuum model of

Table 2.3: Continuum parameters for all observations.

RGS				
Observation	F_{PL} [a]	Γ_{PL}	F_{MBB} [a]	kT_{MBB} (keV)
1	5.42±0.07	2.30±0.03	0.59±0.11	0.092±0.006
2	5.73±0.08	2.35±0.03	0.67±0.17	0.093±0.007
3	4.90±0.10	2.06±0.04	0.91±0.11	0.129±0.006
all	5.44±0.05	2.26±0.02	0.68±0.09	0.096±0.004
RGS + pn				
Observation	F_{PL} [a]	Γ_{PL}	F_{MBB} [a]	kT_{MBB} (keV)
1	5.41±0.05	2.30±0.01	0.61±0.06	0.092±0.003
2	5.72±0.06	2.35±0.02	0.67±0.11	0.093±0.005
3	4.94±0.06	2.07±0.02	0.87±0.05	0.129±0.002
all	5.51±0.02	2.27±0.01	0.63±0.04	0.095±0.002

[a] The unabsorbed flux in the 0.3−2 keV band in 10^{-14} W m^{-2}.

the power law and modified blackbody from here on. The spectrum appears to be harder during the 3rd observation, while there is no significant difference between the first two observations (as expected, since they were taken only two days apart). The continuum parameters for the simultaneous fit are exactly the same as the RGS fits, but the errors are reduced because of the addition of the pn spectrum.

2.5.2 Emission lines

Several broad and narrow emission lines are visible in the spectrum (see Fig. 2.3). The O VII f narrow emission line (rest wavelength 22.101 Å Kelly 1987), as well as the broad O VII recombination line at 21.602 Å (Engstrom & Litzen 1995) and a broad N VII emission line at 24.78 Å (Garcia & Mack 1965). The oxygen lines have already been detected by S07 (although they detect a broad intercombination line instead of a recombination line), but the N VII emission line is a newly detected feature. Table 2.4 shows the line parameters for the RGS only fit. The wavelength of the O VII f line appears to shift between observations. However, this region suffers from bad pixels, which vary from observation to observation, so if one of the bad pixels falls on top of the location of the emission line, the fitted position shifts, depending on the surrounding pixels. Since these lines escape detection in the pn spectrum, we did not fit them in the simultaneous spectrum, but take the fitted values from the RGS only spectra. We fixed the width of the broad emission lines to 0.8 Å, which corresponds to the width of the optical BLR (FWHM $\sim$ 8000 km s^{-1}). We also kept the wavelengths fixed to the rest-frame values. We do not detect any significant variability in the emission lines.

Table 2.4: Emission line parameters for all observations, fluxes are corrected for Galactic absorption.

Line	Observation	Wavelength (Å)	Flux (ph m^{-2} s^{-1})	FWHM (Å)
O VII r	1	21.602 (f)	3.0 ± 0.4	0.8 (f)
O VII r	2	21.602 (f)	2.3 ± 0.6	0.8 (f)
O VII r	3	21.602 (f)	2.3 ± 0.5	0.8 (f)
O VII r	all	21.602 (f)	2.4 ± 0.3	0.8 (f)
N VII Lyα	1	24.78 (f)	1.0 ± 0.3	0.8 (f)
N VII Lyα	2	24.78 (f)	0.8 ± 0.4	0.8 (f)
N VII Lyα	3	24.78 (f)	1.0 ± 0.4	0.8 (f)
N VII Lyα	all	24.78 (f)	1.1 ± 0.2	0.8 (f)
O VII f	1	22.07 ± 0.01	0.6 ± 0.2	-
O VII f	2	22.07 ± 0.03	0.2 ± 0.2	-
O VII f	3	21.99 ± 0.02	1.0 ± 0.5	-
O VII f	all	21.99 ± 0.02	0.30 ± 0.11	-

[1] The (f) indicates that the parameter was kept fixed.

2.5.3 Warm absorber

We detect three distinct warm absorber components, similar to what S07 found by stacking two earlier RGS observations of Mrk 509. We started out by using only one component, and then added components as the fit required. The second and third components are needed (ΔC = 50 and 40 respectively), but adding a fourth component does not improve the fit any further. The warm absorber in Mrk 509 consists of a low ($\xi \sim 0.6$), a medium ($\xi \sim 2.0$), and a high ($\xi \sim 3.1$) ionization component. The main absorption lines visible in the spectrum can be seen in Fig. 2.3. All warm absorber parameters are shown in Table 2.5. The values for the parameters are consistent for the RGS only and the simultaneous fit, but the errors on the latter are smaller due to the addition of the pn spectra. All parameters were set to a reasonable initial value (based on average values of warm absorber parameters found in the literature) and then freed to obtain the best fit.

2.6 Discussion

2.6.1 Warm absorber variability

When comparing the warm absorber components for all three observations, we do not detect any significant variability in components 1 and 2. The high ionization component, does show a change in column density and ionization parameter between the first and the third observations. Changes in column density can be either due to motion across the line of sight, or as in NGC 5548 (Chapter 4) due to recombination

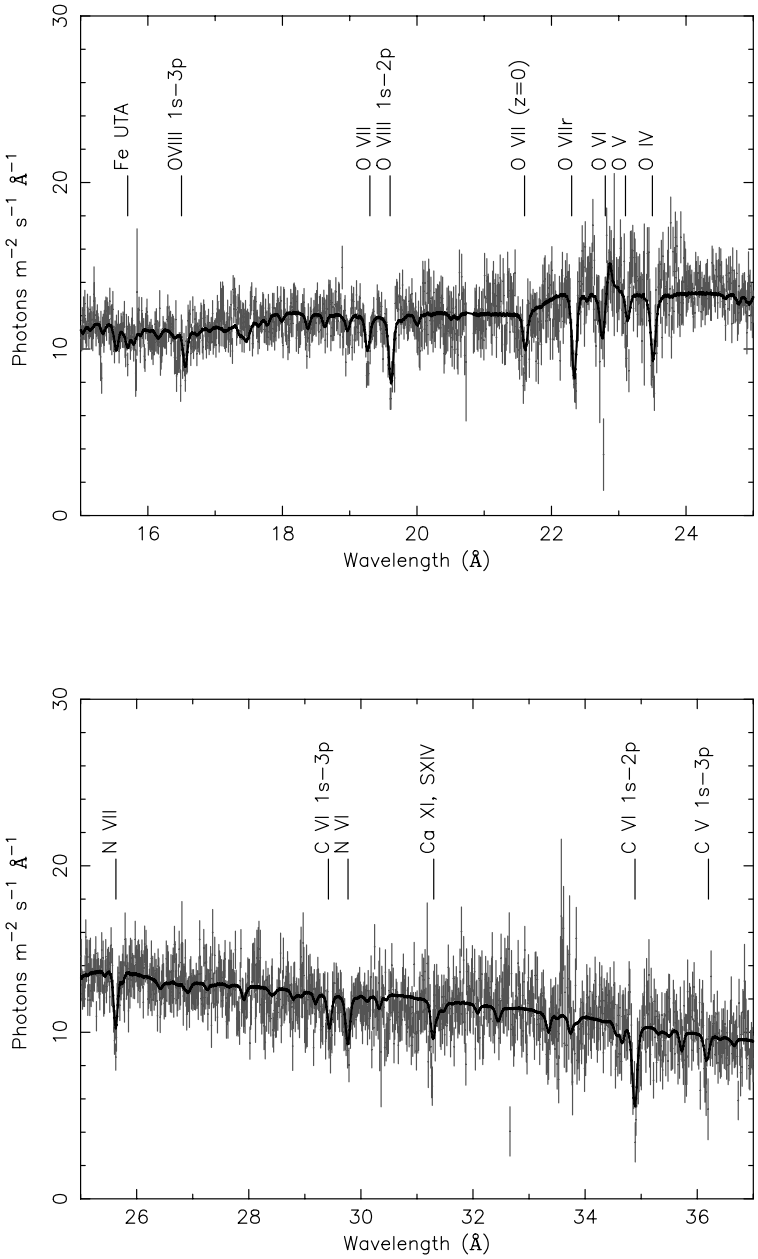

Figure 2.3: The best-fit RGS spectrum for the stacked observation with the absorption lines indicated.

Table 2.5: Warm absorber parameters.

RGS					
Comp	Obs	$N_H{}^a$	log ξ^b	v^c	Δv^d
		(10^{24} m^{-2})	(10^{-9} W m)	(km s^{-1})	(km s^{-1})
1	1	1.35±0.31	0.60±0.18	95±40	− 230±70
	2	0.77±0.27	0.34±0.20	95 (f)	− 230 (f)
	3	0.61±0.21	0.60±0.23	95 (f)	− 230 (f)
	all	1.0±0.2	0.6±0.1	170± 40	− 120± 60
2	1	12.0±2.1	1.97±0.03	80±20	0^{+20}_{-100}
	2	11.4±2.5	1.94±0.03	80 (f)	0 (f)
	3	6.1±1.7	1.91±0.04	80 (f)	0 (f)
	all	10.5±2.0	1.95±0.02	70± 10	0±40
3	1	52±21	3.27±0.09	65±50	− 490±120
	2	26±12	3.13±0.12	65 (f)	− 490 (f)
	3	23±9	3.06±0.09	65 (f)	− 490 (f)
	all	80^{+90}_{-20}	3.20±0.08	25±10	− 290±40
RGS + pn					
1	1	1.36±0.23	0.64±0.15	95±40	− 230±70
	2	0.79±0.22	0.35±0.17	95 (f)	− 230 (f)
	3	0.68±0.19	0.63±0.20	95 (f)	− 230 (f)
	all	1.2±0.2	0.61±0.10	170±40	− 120±60
2	1	12.0±1.7	2.01±0.02	80±20	0^{+10}_{-110}
	2	11.4±1.6	1.96±0.03	80 (f)	0 (f)
	3	6.1±2.8	1.92±0.04	80 (f)	0 (f)
	all	10.5±2.0	2.01±0.03	70±10	0±40
3	1	51±14	3.29±0.04	65±50	-475^{+60}_{-140}
	2	25.4±6.2	3.11±0.06	65 (f)	− 475 (f)
	3	18.2±5.0	3.01±0.06	65 (f)	− 475 (f)
	all	69^{+80}_{-10}	3.19±0.06	25±10	− 295±40

[1] The (f) indicates that the parameter was kept fixed.
[a] Column density.
[b] Ionization parameter.
[c] r.m.s. velocity broadening
[d] Outflow velocity, a negative velocity corresponds to a blueshift.

/ re-ionization of the absorbing gas due to a change in the continuum flux. One has to be careful, however in this case, as there is a correlation between ξ and column density, in the sense that a lower ξ and smaller column density can produce the same spectral fit as a higher ξ, larger column density case. To check for this effect we also performed a fit where we kept the column density fixed to the column density of the first observation. All three observations have the same ξ value for the high ionization component (log ξ = 3.25). However for the third observations the fit in

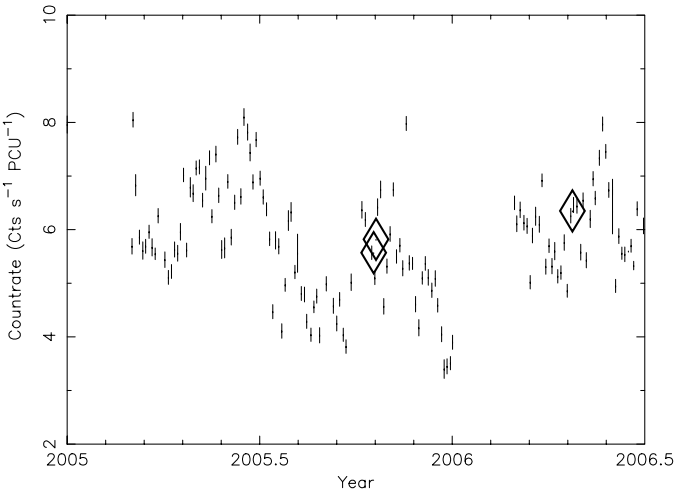

Figure 2.4: The RXTE 2−10 keV lightcurve of Mrk 509, from 2005 to 2007. Data were taken from the online RXTE mission-long data products. The diamonds indicate the exact date of the three *XMM-Newton* observations used in this paper.

this case is worsened by Δ C = 37 for 1 d.o.f. with respect to the fit shown in Table 2.5. This indicates that the change in ionization parameter and column density between observations 1 and 3 is significant.

Using the *RXTE* monitoring data of Mrk 509 taken with the PCA, we in principle can know what the continuum flux history is for this source before and after the three *XMM − Newton* observations. However, the gap during the first few months of 2006, prevents us from obtaining a more accurate timescale for the changes detected in the spectrum than the time between the 2nd and 3rd observation, namely half a year. If we make the assumption that the change in column density and ionization parameter we see are due to recombination of the component 3 gas due to the minimum, then we can get an estimate for the distance of this component using the relation:

$$\xi = \frac{L}{nR^2}, \tag{2.3}$$

where ξ is the ionization parameter, L the $1 - 1000$ Rydberg luminosity, n the density of the gas, and r the distance from the ionizing source. The $1 - 1000$ Rydberg luminosity of Mrk 509 is 4.9×10^{37} W (as taken from the first observation). If we know the density of the gas, then we can constrain the location of the gas, since ξ and L are known from observations. To determine n, we must know the recombination or ionization timescale of the gas, which is given by (Krolik & Kriss 1995, Bottorff

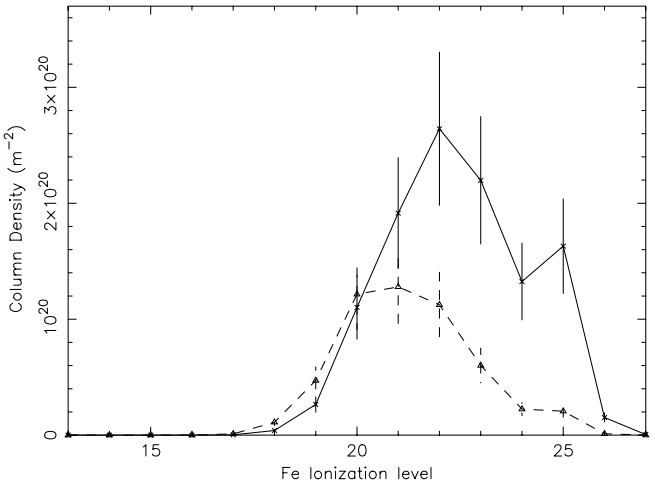

Figure 2.5: Column densities for the different ionization levels of iron for the high ($\log \xi = 3.2$) component. The solid line represents the first observation, while the dotted line represents the third observation.

et al. 2000):

$$\tau_{\rm rec}(X_i) = \left(\alpha_{\rm r}(X_i) n \left[\frac{f(X_{i+1})}{f(X_i)} - \frac{\alpha_{\rm r}(X_{i-1})}{\alpha_{\rm r}(X_i)}\right]\right)^{-1}, \tag{2.4}$$

where $\alpha_{\rm r}(X_i)$ is the recombination rate from ion X_{i+1} to ion X_i and $f(X_i)$ is the fraction of element X in ionization state i. From the time between observations 2 and 3, we get an upper limit to $\tau_{\rm rec}$ of 0.5 years. If we then take the Fe XXII ion as an example (since this is where the ionization level of iron peaks in column density for this component, see Fig 2.5), we get a lower limit to the density n of 1.3×10^{11} m^{-3}. From this we can constrain the location of this outflow component to within 0.5 pc of the central source. This does not allow us to distinguish between a scenario where the warm absorber is launched from the accretion disk (i.e. located at BLR distances) or from the dusty torus. Oxygen, neon, carbon, and nitrogen are not produced in significant column densities by this high ionization component, so the only ions for which the column densities show any significant change are Fe XXII to Fe XXV. If we perform the same exercise for the other ions, we obtain less strict upper limits (up to 4 pc for Fe XXV).

For the other two components that do not vary between the three observations, the non-variability can be due to two reasons.

- The density is low, so that the recombination time of the gas is longer than the

time between observations 3 + 4 and observation 5, i.e. $\tau_{\rm rec} \geq 0.5$ years.

- The density is high enough to track the short time variability of the source, say, on a timescale of a few days, as the fluxes of all observations are within 10 % of each other.

2.6.2 Comparison with previous results

Cappi et al. (2009) have found evidence of a highly ionized and variable outflow component using the same pn data as we used. In the RGS data, there is no evidence of such an absorber with a mildly relativistic outflow velocity. As the main goal of this paper is on the cross-calibration of RGS and pn, we focused our attention of the pn analysis only in the 7−38 Å wavelength range. This highly ionized, fast outflowing absorber might represent an extreme part of the outflow described here or it might be disconnected given its high outflow velocity.

If we compare the outflow components in our present spectra with those analyzed by S07, we see that the ionization parameters are consistent, although we find slightly lower values. The column density of the low ionized gas ($\log \xi \approx 0.6$) is a factor of 10 higher in the S07 observations. However, the velocity broadening v they find is 0 instead of the 105 km s^{-1} that we find. Another difference is the outflow velocity. We find the highest outflow velocity (−425 km s^{-1}) for the highly ionized ($\log \xi \sim 3.1$) component, while S07 find the highest outflow velocity for the component with $\log \xi \sim 0.9$.

These differences may stem from a combination of several effects:

1. Systematic uncertainty of 7 mÅ (50−200 km s^{-1}) in the RGS wavelength scale.
2. A different continuum modeling in our paper compared to S07.
3. Lower S−N ratio in the S07 data.
4. An almost similar fit obtained by lowering the velocity broadening, and increasing the column density, for components dominated by saturated lines.
5. True time variability of the source.

All this argues for a monitoring campaign where high data quality is obtained and the variations of the source are continuously monitored. Such a campaign is now underway.

2.6.3 Cross-calibration between RGS and pn

This is a first attempt to model the relative calibration between pn and RGS to be able to detect small changes in outflow properties. Our method for modeling the relative calibration is a relatively simple one, but a cursory glance at the differences between Figs. A.1 and A.2 shows the clear improvements for the fit to the pn spectrum. If we

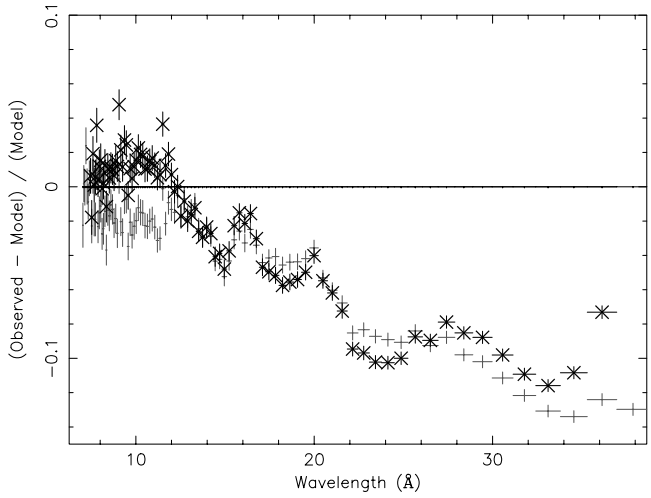

Figure 2.6: Comparison of the ratios *R* for both methods (see Fig A.2) for the stacked spectrum. The thin points are the *R* values for method 1, while the thick crosses are the *R* values for method 2.

compare the cross-calibration residuals for both the first method (RGS model for pn spectrum) and the second one (fluxed RGS spectrum folded through pn response), we see that, apart from a difference for the first observation below 10 Å, the residuals for both methods are almost identical (see Fig. 2.6). However, there is a difference at long wavelengths, particularly from 22 Å onwards. The same wave-like pattern can be seen between 22 and 32 Å in Fig 2.2. The difference is about 1.5 % between the fluxed and the fitted data. The difference between the RGS fluxed and the fitted spectrum can only be due to slight modeling inaccuracies, not to any calibration offsets in the effective area of RGS or pn, as both methods use the same effective area. This means that, by comparing the fluxed and the fitted residuals in the pn, we can separate the inaccuracies due to modeling and those from uncertainties in the effective area calibration of RGS in the residuals seen in Fig. 2.2. These residuals are only apparent when the spectra are heavily rebinned. At higher resolution, these residuals would not have been detected. From the comparison of the fluxed and fitted pn residuals we find that about 1.5 % comes from modeling inaccuracies in the RGS fit. The strong wiggle in Fig. 2.6 between 22 and 26 Å with an amplitude of about 5 % may be related to uncertainties in the pn model. Similar features can be seen in the residuals of, for instance, 3C273 orbit 1381 (see the calibration review tool[7]).

[7]http://xmm2.esac.esa.int/cgi-bin/ept/preview.pl

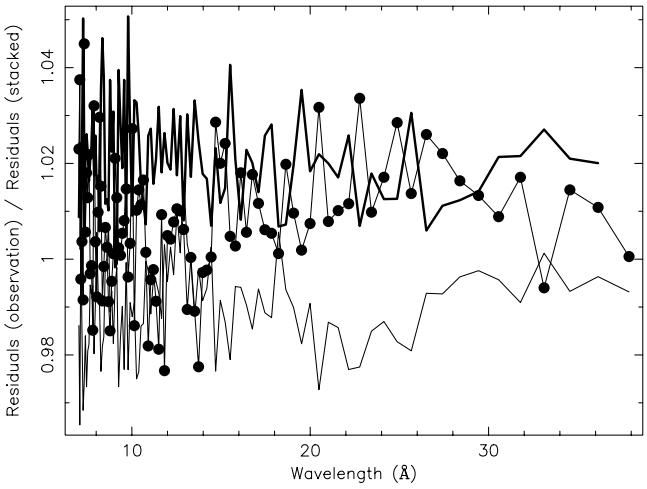

Figure 2.7: Ratio of the pn residuals for each observation compared to the stacked spectrum. Observation 1 is indicated by the thin black line, observation 2 by the thin black line with dots, and observation 3 by the thick black line.

Both methods show the same general trend for the pn residuals. There is a sharp drop around 23 Å, which is where the oxygen edge is located, possibly indicating that the modeling of this instrumental edge has some uncertainties. Comparing the residuals in Figs 2.7 and A.1 between observations, we see that the general shape is exactly the same for each observation. There only appears to be a slight shift of ~ 3 % between observations 1 and 3. The reason for this shift is the difference in flux in the RGS1 and RGS2 spectra of observation 3. Based on the comparison between the *knak* parameters, see Table 2.2, the RGS2 spectrum is the correct one. This means that in Fig. A.2 the residuals in observation 3 should be shifted by 1−2 % downwards, which brings it into agreement with the previous observations. The reason for this 2 % flux difference is unknown. We checked for possible differences in exposure times or background filtering criteria between the two RGS, and there is no difference between both RGS exposure times. The difference remains, independent of the exact criteria used for background filtering. As another check, we varied the spectral extraction region for the third observation (90, 95 and 98 % of the cross-dispersion PSF respectively). The difference between RGS1 and RGS2 remains here, too. At this moment we have no good explanation for this flux difference. It may, however, be a rare statistical variation at the 3.5 sigma level.

If we compare the residuals with other cross-calibration investigations, as shown on the calibration review tool website for *XMM-Newton*, we find identical features in

similar sources, such as PKS 2155-304 and 3C273, which show that below 0.5 keV the RGS flux is about 10 % higher than the pn flux. This gives us additional confidence that out method and our results are correct and can be applied to other sources. However, sources like Mrk 509 are the best for studying the cross-calibration, as the pn data are not piled-up, but the source is still bright enough in the RGS to obtain a high-quality spectrum.

The main application for this modeling of the relative calibration is the increased sensitivity to changes in the outflow column densities and the ionization parameter the simultaneous fit provides. A comparison of Table 2.5 shows that performing a simultaneous fit improves the accuracy of the measurements (column density and ionization state) by almost a factor of two. Without correcting for the relative calibration, this would not have been possible.

Our method has several assumptions. The first is that the RGS data give us the best fit for the warm absorber and the emission lines. Also we assume that the RGS continuum fit gives the correct continuum. But since we are only interested in the relative calibration, we did not draw any conclusions as to which of the two instruments is better calibrated in an absolute sense. We used the RGS to determine the best fit to the spectrum, because of the high-resolution needed for precisely determining the outflow properties. However as can be seen from Fig. 2.2, the RGS spectrum shows broad band fluctuations on the order of 3−4 %. As already mentioned earlier, this sets a limit on how good our relative calibration modeling can get. Also the exact *knak* model we have is strictly valid at this moment for sources with the same spectral type as Mrk 509, since there are indications that the relative calibration differences appear to be source and pn mode dependent[8]. This indicates that the redistribution of pn is partly responsible for the differences in the RGS and pn flux, since a different spectral slope will have a strong effect on the exact redistribution of photons in the pn spectrum. This is also what has been reported to the *XMM-Newton* Users Group[9]. Applying this method to other sources (including non-AGN sources) and looking at the exact differences between the obtained relative calibration residuals (i.e. the exact values of the *knak* model for example) gives us an opportunity to determine the exact origin of the differences between RGS and pn.

2.7 Conclusions

We have investigated the cross-calibration differences between *XMM* pn and RGS. By modeling the cross-calibration differences, which are consistent for all three observations and the stacked spectrum, we were able to improve the calibration for pn and RGS to within 4% of each other. Using this method, we can detect small variations in the outflow column density and ionization state more accurately. For Mrk 509 we used this method in combination with the *RXTE* lightcurve to constrain the location of the highly ionized component ($\log \xi \approx 3.2$) to within 4 pc of the central

[8] http://xmm2.esac.esa.int/external/xmm_sw_cal/calib/cross_cal/index.php
[9] http://xmm.esac.esa.int/external/xmm_user_support/usersgroup/20090506/index.shtml

source. The other components do not show any significant variability, despite the source varying in flux between the 2005 and 2006 observations. With this improvement to the relative calibration of the XMM instruments, we can use the advantage of simultaneous pn and RGS observations to detect and model small changes in the outflow of AGN. This will allow us to expand outflow studies to sources that vary more slowly and have a smaller amplitude, thereby increasing the number of Seyfert 1 galaxies that can be studied in this way. This method can also be expanded to other types of sources, as the method itself is source-independent.

Chapter 3

Multiwavelength campaign on Mrk 509 III. The 600 ks RGS spectrum: unravelling the inner region of an AGN

R.G. Detmers, J.S. Kaastra, K. Steenbrugge, J. Ebrero, G.A. Kriss, N. Arav, E. Behar, E. Costantini, G. Branduardi−Raymont, M. Mehdipour, S. Bianchi, M. Cappi, P. Petrucci, G. Ponti, C. Pinto, E.M. Ratti and T. Holczer

Published in Astronomy & Astrophysics, volume 534, A38, 2011

3.1 Abstract

We present the results of our 600 ks RGS observation as part of the multiwavelength campaign on Mrk 509. The very high quality of the spectrum allows us to investigate the ionized outflow with an unprecedented accuracy due to the long exposure and the use of the RGS multipointing mode. We detect multiple absorption lines from the interstellar medium and from the ionized absorber in Mrk 509. A number of emission components are also detected, including broad emission lines consistent with an origin in the broad line region, the narrow O VII forbidden emission line and also (narrow) radiative recombination continua. The ionized absorber consists of two velocity components ($v = -13 \pm 11$ km s^{-1} and $v = -319 \pm 14$ km s^{-1}),

which both are consistent with earlier results, including UV data. There is another tentative component outflowing at high velocity, -770 ± 109 km s^{-1}, which is only seen in a few highly ionized absorption lines. The outflow shows discrete ionization components, spanning four orders of magnitude in ionization parameter. Due to the excellent statistics of our spectrum, we demonstrate for the first time that the outflow in Mrk 509 in the important range of $\log \xi$ between 1−3 cannot be described by a smooth, continuous absorption measure distribution, but instead shows two strong, discrete peaks. At the highest and lowest ionization parameters we cannot differentiate smooth and discrete components.

3.2 Introduction

One of the main reasons to study active galactic nuclei (AGN) is to learn about feedback from the AGN to the galaxy and its direct environments. Feedback is a combination of enrichment (the spreading of elements into the interstellar and inter galactic media (ISM and IGM), momentum feedback (due to winds), and direct kinetic feedback (i.e. energy ejection into the ISM or IGM by jets). From recent observations on cooling clusters of galaxies (see e.g. McNamara & Nulsen 2007, for an overview), as well as from recent insights into galaxy and AGN co-evolution (Di Matteo et al. 2005, Elvis 2006, Bower 2009, Fabian 2010), it has become clear that feedback from AGN is a crucial ingredient the evolution of galaxies and clusters of galaxies. This is also seen in the so-called M-σ relation, which links the velocity dispersion of stars in the bulge to the mass of the Super-Massive Black Hole (SMBH) (Ferrarese & Merritt 2000, Gebhardt et al. 2000). While we have a reasonable qualitative understanding of the feedback from relativistic jets (as observed in clusters of galaxies, see e.g. Fabian et al. 2003), we still lack a quantitative picture of the feedback of the AGN on the galaxy and on its surroundings.
There is a broad ongoing effort to improve this, and recent work on broad absorption line (BAL) quasars shows that the mass outflow rates in these systems are 100s of solar masses per year and the kinetic luminosity involved is a few percent of the total bolometric luminosity (Moe et al. 2009, Dunn et al. 2010). There have also been indications that some AGN harbor a highly ionized, massive, ultra-fast outflow, with velocities reaching up to 60 000 km s^{-1} (Reeves et al. 2003, Pounds & Reeves 2009, Ponti et al. 2009, Tombesi et al. 2010b,c). These outflows are hard to detect, however, and appear to be variable (because they are only present in some observations of a single source). These are extreme cases of outflows that are present in only a fraction of the total number of AGN. Whether feedback from less extreme outflows, such as those that are present in about 50 % of the local Seyfert 1 galaxies is also important, remains an unsolved question.

If we can establish the impact that the outflow has on the galaxy in these local Seyfert 1 galaxies, this should allow us to extend the feedback estimates that we obtain to higher redshifts to the more powerful AGN, which we are unable to investigate with the current generation of X-ray grating spectrometers. However we first need

to deal with the two main uncertainties concerning the outflows. These are the geometry of the inner region of an AGN and the location or origin of the outflow (see e.g. Murray & Chiang 1997, Krolik & Kriss 2001, Gaskell et al. 2007). Earlier work has placed the outflow at various distances, and also the estimates for feedback can vary wildly (see e.g. Behar et al. 2003, Blustin et al. 2005, Krongold et al. 2007, and 4 for some examples). Therefore answering these two questions is the main goal of the Mrk 509 multiwavelength campaign.

Multiwavelength campaigns on AGN are crucial for gaining a complete understanding of the inner regions of these sources. Earlier multiwavelength campaigns focused mainly on abundance studies of the outflow (see Mrk 279, Arav et al. 2007) or on determining the outflow structure and location by combining UV and X-ray data e.g. NGC 5548 (Steenbrugge et al. 2005); NGC 3783 (Netzer et al. 2003, Gabel et al. 2003). Our dedicated multiwavelength campaign on Mrk 509 is much more extensive than previous attempts. Our more intensive observations are ideal for locating the outflow, using the variability of the source and response of the ionized gas to determine its location (the use of variability to locate gas has been very successfully used in reverberation mapping of the BLR, see e.g. Peterson & Wandel 2000, Denney et al. 2010, for an overview of the method and for the latest results).

Apart from the location and kinematics, one of the other important questions regarding the outflow is what the ionization structure is. Earlier studies have reported different results. The outflow in NGC 5548 appears to be a continuous distribution of column density vs. $\log \xi$ (Steenbrugge et al. 2005). NGC 3783, on the other hand, shows different separate ionization components, all in pressure equilibrium (Krongold et al. 2003). In Mrk 279 the situation appears to be more complex, because a non−monotonous, continuous distribution provides the best description to the data (Costantini et al. 2007b). Recently, Holczer et al. (2007) and Behar (2009) have shown that for most local Seyfert 1 galaxies with an outflow, a continuous distribution of column density vs. ionization parameter is the best description of the data. What they also show is that there are distinct ξ values where no is gas present. They interpret these gaps as thermal instabilities that cause the gas to rapidly cool or heat and then shift to other ionization parameters. What is clear from these studies is that there is no single model that describes all the observed outflows. High−quality, high−resolution spectra of the outflows are crucial for investigating the structure, since it can be the case (as in Mrk 279) that some components of the outflow have very low column density, which would otherwise escape detection.

Mrk 509 is one of the best studied local AGN, and due to its large luminosity ($L(1-1000\,\mathrm{Ryd}) = 3.2 \times 10^{38}$ W), it is also considered to be one of the closest QSO/Seyfert 1 hybrids. Earlier work on the outflow in the X-ray regime has revealed that it consists of a wide range of ionization components, but lacks the very high and also very low ionized gas (weak Fe UTA and no Si XIV Lyα, Yaqoob et al. 2003). The outflow has been described using three ionization components, each with a different outflow velocity (Smith et al. 2007); however, the exact outflow velocities differ between different publications, most likely due to a limited signal−to−noise ratio. In Chapter 2 we have analyzed three archival observations of Mrk 509 with *XMM-Newton*. They

also find three components for the outflow, although with different velocities than Smith et al. (2007). Including the EPIC-pn data and improving the relative calibration between RGS and EPIC-pn achieved increased sensitivity. With this improvement they were able to detect variability in the highest ionization component, constraining the distance of that component to within 0.5 pc of the central source. Another point of interest is that there have been indications of an ultra-high velocity outflow as seen through the Fe K line (Cappi et al. 2009, Ponti et al. 2009). This outflow could make a potentially large contribution to feedback, as the velocity is very high, although it appears to be transient (Ponti et al. 2009).

This work is the third in a series of papers analyzing the very deep and broad multiwavelength campaign on Mrk 509. The complete campaign details are presented in Kaastra et al. (2011c), hereafter Paper I. Here we present the main results obtained from the stacked 600 ks *XMM-Newton* RGS spectrum. With this spectrum, we are able to characterize the properties of the ionized outflow in great detail (velocities, ionization states, column densities, density profile, etc.). Other features detected in the spectrum (emission lines, Galactic absorption, etc.) will not be discussed in detail here. Because different physics are involved, we will discuss them in future papers in this series.

This article is organized as follows. Section 3.3 briefly describes the data reduction for obtaining the stacked spectrum, and we show the spectral models that we use to describe the data. The spectral analysis and the results are presented in Sect. 3.4. We discuss our results in Sect. 3.5 and present our conclusions in Sect. 3.6.

3.3 Data reduction and modeling

3.3.1 Data reduction

The RGS data reduction used here is much more complex than the standard pipeline processing using the *XMM-Newton* Science Analysis System (SAS), the main reasons among others being the use of the RGS multi-pointing mode, a variable source and a nonstandard procedure of filtering for bad pixels. The full details of the data reduction and all the necessary steps are found in Kaastra et al. (2011b), hereafter paper II. In short, we used the SAS 9.0 software package to reduce all the individual observations. Then we created a fluxed spectrum for each observation and stacked those taking the effects of the multi-pointing mode into account. This way a fluxed RGS spectrum was created by stacking both RGS 1 and 2 and both spectral orders. We used this fluxed spectrum for fitting our data. Figure 3.1 shows the full fluxed spectrum with some of the strongest lines indicated.

3.3.2 Setup

We used data between 7 and 38 Å when fitting the RGS spectrum. As the fluxed spectrum consists of both the RGS 1 and 2 data in both spectral orders, we binned

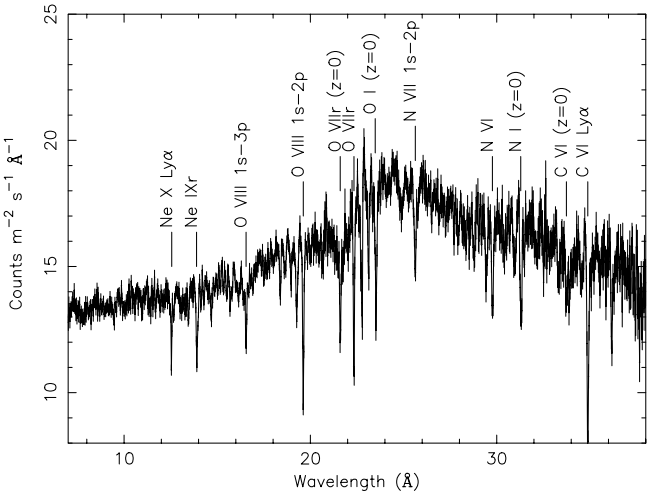

Figure 3.1: The fluxed stacked RGS spectrum in the 7 - 38 Å range. The strongest lines are indicated and the O I ISM edge can be clearly seen around 23 Å.

the data between 7 and 38 Å in 0.01 Å bins. The average number of counts per 0.01 Å bin is approximately 900 (i.e. a signal−to−noise−ratio of about 30). We therefore used χ^2 statistics when fitting the spectrum. All errors are given for $\Delta\chi^2 = 1$. We used the SPEX 2.03.00[1] spectral fitting package to fit the spectrum. We updated the wavelengths of some important transitions for our study (see Appendix).

We constructed the spectral energy distribution (SED) for Mrk 509, using the EPIC-pn and OM data to obtain the necessary flux points for the *XMM-Newton* observations and extending it with other data. This SED is an average of the Mrk 509 SED during the time of observations (roughly two months time). The full procedure on how the SED was derived can be found in Kaastra et al. (2011c). The ionization balance calculations needed for our spectral modeling (the *xabs* components, see Sect. 3.4.2) were based on this SED and performed using version C08.00 of Cloudy[2](Ferland et al. 1998) with Lodders & Palme (2009) abundances.

3.3.3 Spectral models

The unprecedented quality of the spectrum requires a rather complex spectral model to be described accurately. We describe each component in more detail in separate sections, but we give a short overview of the total model here.

[1] see http://www.sron.nl/spex
[2] http://www.nublado.org/

We model the continuum with a spline (see Fig. 3.2). The main reason for doing so is that a spline can accurately describe the (complex) continuum shape without having to make any physical assumptions about the origin of the shape of the continuum (powerlaw, blackbody, Comptonization, or reflection, for example). We use a redshift $z = 0.03450$, which combines the cosmological redshift (Huchra et al. 1993) with the orbital velocity of the Earth around the Sun, which is not corrected for in the standard *XMM-Newton* analysis (see Kaastra et al. 2011c). Galactic absorption ($N_H = 4.44 \times 10^{24}$ m^{-2}, Murphy et al. 1996) is also taken into account. We use three distinct phases for the Galactic ISM absorption, a neutral (kT = 0.5 eV) phase, a warm (kT = 4.5 eV) slightly ionized phase, and a hot (kT = 140 eV) highly ionized phase (Pinto et al. 2010). Additionally we model the neutral oxygen and iron edges of the ISM by including a dusty component. Details about the Galactic foreground absorption are given by Pinto et al. (in prep).

The ionized outflow is modeled with three different models, each with multiple (two or three) velocity components to account for the separate outflow velocities observed. All models take a wide range of ionization states into account. These models are described in more detail in Sect. 3.4.2. We also included eleven broad and narrow emission lines, which are modeled with a Gaussian line profile. Radiative recombination continua (RRCs) are also included using an ad-hoc model that takes the characteristic shape of these features into account .

3.4 Spectral analysis

3.4.1 Continuum, local absorption, and emission features

The continuum is modeled with a spline with a logarithmic spacing of 0.075 between 5 and 40 Å. We show the spline model in Fig. 3.2 and in Table 3.1. The continuum is smooth, so the spline does not mimic any broad line emission features. The softening of the spectrum at longer wavelengths can be seen clearly.

The neutral Galactic absorption is responsible for the narrow O I (23.5 Å) and N I (31.3 Å) absorption lines. To fit the Galactic O II absorption line we add a slightly ionized component with a temperature of 4.5 eV and with a column density that is 4 % of the cold, neutral gas (Pinto et al., in prep). To properly model the O I edge, we take the effects of depletion into dust into account. This same depletion is also responsible for the lack of a strong neutral iron absorption blend around 17.5 Å. We use dust that consists of pyroxene and hematite.

The sightline to Mrk 509 passes through a high-velocity cloud located in the Galactic halo (see e.g. Sembach et al. 1995). The hot gas as seen in the C VI, O VII, O VIII, and Ne IX absorption lines at $z = 0$ could either be from ISM absorption in our Milky Way or from this high-velocity cloud (which has an LSR velocity of around -250 km s^{-1}). A more detailed multiwavelength analysis and comparison of all these local components will be presented in a follow-up paper (Pinto et al. ,in prep).

The spectrum shows some emission lines, most of which are broadened (Table

Table 3.1: Spline continuum parameters.

Wavelength (Å)	Flux (photons m^{-2} s^{-1} $Å^{-1}$)
5.00	0
5.95	0.7 ± 0.6
7.07	13.95 ± 0.09
8.41	14.28 ± 0.06
10.00	15.10 ± 0.04
11.89	15.92 ± 0.09
14.14	17.27 ± 0.09
16.82	19.36 ± 0.16
20.00	21.31 ± 0.11
23.78	25.15 ± 0.08
28.28	27.83 ± 0.11
33.64	33.62 ± 0.19
40.00	9.80 ± 0.18

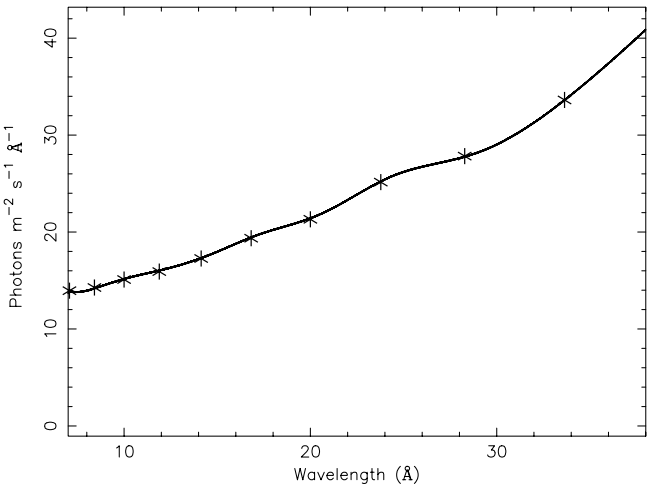

Figure 3.2: The unabsorbed spline continuum model used for the Mrk 509 observations.

3.2). In this table we also show the change in χ^2 when the line is omitted from the model. The broad emission lines are visible as excesses on both sides of the corresponding absorption lines (see Fig. 3.3). In our modeling we fix the width of the lines to an FWHM of 4200 ± 200 km s^{-1} as measured for the Balmer lines

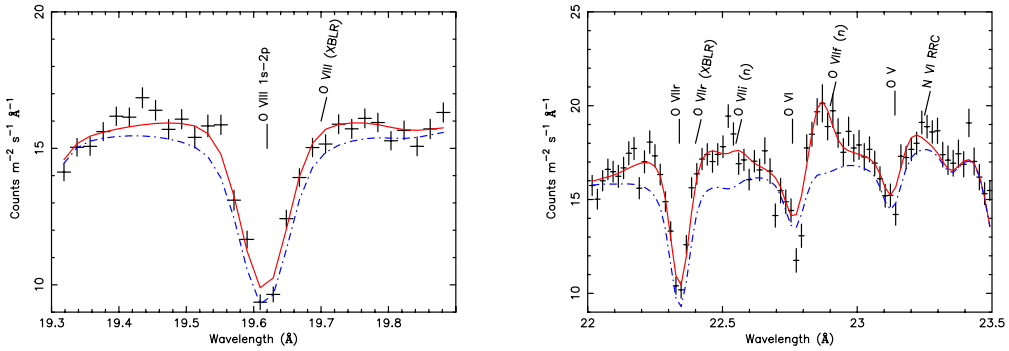

Figure 3.3: Broad and narrow X-ray emission lines of O VIII Ly α (left) and O VII (right). The model without any broad lines is shown as the dashed-dotted line, while the model (model 2) with the lines and RRC included (marked as XBLR and n) is shown as a solid line.

Table 3.2: Broad emission line parameters for the combined spectrum, where fluxes are corrected for Galactic and intrinsic absorption.

Line	Wavelength (Å)	Flux (ph m^{-2} s^{-1})	$\Delta\chi^2$
O VII r	21.602	1.00±0.09	82
O VII i	21.802	< 0.56	0
O VII f	22.101	< 0.7	0
O VIII Lyα	18.967	0.42±0.04	46
N VII Lyα	24.780	0.09±0.06	1
C VI Lyα	33.736	0.25±0.10	3
Ne IX r	13.447	0.26±0.03	40

[1] All the wavelengths were fixed to the laboratory wavelength.

simultaneously by the OM optical grism (Mehdipour et al. 2011). We assume that these lines originate in the BLR (Costantini et al. 2007b).

We also detect the narrow O VII f emission line with an absorption−corrected flux of 0.46 ± 0.06 ph m^{-2} s^{-1}, as well as a weaker intercombination line with a flux of 0.13 ± 0.04 ph m^{-2} s^{-1} and an Ne IX f emission line with a flux of 0.09 ± 0.02 ph m^{-2} s^{-1}. The narrow resonance line cannot be separated from the absorption line, so we have assumed a ratio of 3:1 for photoionized gas for the forbidden−to−recombination line ratio (Porquet & Dubau 2000). We do not detect any other narrow emission lines. In our spectral modeling we adopt an FHWM of 610 km s^{-1} for these narrow emission lines, based on the width of the optical [O III] emission line (Phillips et al. 1983). We assume here that these lines are produced in the NLR (Guainazzi & Bianchi 2007). Radiative recombination continua (RRC) have been detected in other Seyfert

Table 3.3: RRC parameters.

Ion	Wavelength (Å)	Flux ph m^{-2} s^{-1}
O VII	16.78	0.08 ± 0.04
O VIII	14.23	< 0.01
C V	31.63	0.18 ± 0.14
C VI	25.30	0.16 ± 0.08
N VI	22.46	0.41 ± 0.18
N VII	18.59	< 0.08
Ne IX	10.37	0.06 ± 0.03
Ne X	9.10	< 0.01

1 spectra (see e.g. NGC 3783 or Mrk 279, Kaspi et al. 2002, Costantini et al. 2007b), so we checked whether they are present in Mrk 509. The RRCs are weak and hard to detect (Table 3.3). We modeled them using the *rrc* model of SPEX and obtain a temperature of 5.4 ± 2.5 eV for the RRC. This low temperature is a direct indication of photoionized gas.

3.4.2 Ionized outflow

We use three different models for characterizing the ionized outflow. We describe each model separately and then compare the results obtained by all three models. By comparing the results for the different models for the ionized outflow, we can investigate its ionization structure and density profile.

The first model (Model 1 from here on, Table 3.4) contains two *slab* components. The *slab* model of SPEX calculates the transmission of a slab of material with arbitrary ionic column densities, outflow velocity v, and r.m.s. velocity broadening σ as free parameters. We assume a covering factor of unity for both components. The *slab* components have a different outflow velocity and velocity broadening. However, we assign each ion to one of the components based on the ionization parameter ξ, which is defined in the following way:

$$\xi = \frac{L}{nr^2}, \tag{3.1}$$

where L is the $1 - 1000$ Rydberg luminosity, n the hydrogen number density of the gas and, r the distance from the ionizing source. For Mrk 509 we obtain an ionizing luminosity of $L = 3.2 \times 10^{38}$ W from the SED. All ions with $\log \xi < 2.1$ are assigned to the first component, while the others are in the second component. The division is based on a preliminary fit where the outflow velocity of individual ions was a free parameter. The first component has an outflow velocity v of -57 ± 8 km s^{-1} and a velocity broadening $\sigma = 158 \pm 5$ km s^{-1}, while the second component has an outflow velocity $v = -254 \pm 40$ km s^{-1} and $\sigma = 133 \pm 30$ km s^{-1}. The ionization parameters

are given in Table 3.4 and are those for which the ion fraction peaks for that ion. The fit gives χ^2 = 3643 for 3109 degrees of freedom (*dof*). We also show in Table 3.4 the best-fit velocities for individual ions when we leave the velocity free compared to the velocities of all the other ions.

The second model (Model 2 from here on, Table 3.4) is an extension of Model 1. Instead of separating the ions according to their ionization parameter, we include all ions for both velocity components. Additionally we add a third velocity component to account for a high−velocity ($v = -770$ km s^{-1}) component (tentatively detected in the Chandra HETGS spectrum, see Yaqoob et al. 2003) mainly to get the appropriate line centroid for the Fe XXI and Mg XI absorption lines. This model is more realistic than Model 1 because it assumes a multivelocity structure for every absorption line, which is consistent with what has been observed in earlier UV observations of Mrk 509 (Kriss et al. 2000, Kraemer et al. 2003). The fit gives χ^2 = 3589 for 3070 *dof*.

The third model (Model 3 from here on, Table 3.6) is based on multiple photoionization components (*xabs*). In each *xabs* component the ionic column densities are related through the ionization parameter ξ. Free parameters are the hydrogen column density $N_{\rm H}$, ionization parameter ξ, r.m.s. velocity width σ, and outflow velocity v. Based on the results of Model 2, we start with one *xabs* component for each of the two main velocity components detected. We add extra *xabs* components until the fit no longer improves. A fit with only one *xabs* component for each velocity results in a fit of χ^2 = 4261 for 3145 *dof*. Adding an additional *xabs* component for each outflow velocity improves the fit by $\Delta\chi^2$ = 264/4 *dof*. We use the same outflow velocity and r.m.s. velocity for the *xabs* components of each velocity component. If we add a third pair of *xabs* components we again improve the fit significantly resulting in a further improvement of $\Delta\chi^2$ = 138/4 *dof*. As a last step, we leave the outflow velocity and the r.m.s. velocity width for each component free. This then improves the fit by $\Delta\chi^2$ = 32/4 *dof*. The best fit we obtain this way has χ^2 = 3827 for 3157 *dof*. The results for the final fit are shown in Table 3.6, however the component with the highest ionization parameter (component E2 in Table 3.6) shifts to a much higher outflow velocity, namely 492 km s^{-1}. We therefore add it to the fast velocity group, so that the slow outflow can now be described properly with two *xabs* components, while the fast outflow is described by four components. We label each component according to its ionization parameter (A to E for increasing ξ) with index 1 or 2 for low and high outflow velocity, respectively.

As a test we also fit a fourth model, the so-called *warm* model, essentially a power-law distribution of *xabs* components. This is similar to the model used by Steenbrugge et al. (2005) in NGC 5548 (model D in that paper) and akin to the absorption measure distribution (AMD) method used by Holczer et al. (2007). We first defined a range of ionization parameters, between which we fit our model. In our case we fit the model between $\log\xi = -2$ and 4. We used a grid of 19 points in order to accurately describe the total AMD. At every grid point a value f_i was determined, which is defined as $f_i = d\,N_{\rm H}\,/d\log\xi$. This way we obtained the distribution of $N_{\rm H}$ versus $\log\,\xi$. We did this for both velocity components (ignoring the very fast −770 km s^{-1} outflow at the moment). The best fit we obtain has χ^2 = 3822 for 3120 *dof*. However due to the

correlation between the two warm component parameters (especially the factors f_i), calculating the exact error on every parameter is very difficult.

We therefore use the *warm* model only to check whether we have missed any ions in our *slab* fit. With a continuous model like *warm*, weaker lines that otherwise might be hard to detect are taken into account. In this way we have identified several ions, which are predicted to be present based on the *warm* model, but were not included in the *slab* fit since they produce only weak lines. These are Ne VII and Si X - Si XII. All these ions, however, have very weak lines in the Mrk 509 spectrum, and the fitted ionic column densities (using the *slab* model) only yield upper limits. We therefore are confident that Models 2 and 3 are accurate representations of the data.

3.4.3 Spectral fit

The RGS spectrum and the best−fit model (Model 2) are shown in Figs. 3.4 − 3.8. All the strongest absorption lines are labeled. Galactic lines are indicated with $z = 0$. The spectrum has been re-binned to 0.02 Å bins for clarity. The model reproduces the data very well. We detect the O VIII Lyman series and the O VII resonance transitions up to the 1s−5p transition, as well as the C VI Lyman series up to the 1s−6p transition. We also detect the O VII and O VIII series from the local $z = 0$ component. The only features that are not reproduced well are the N VI ISM absorption line at 28.78 Å, a feature around 32.5 Å, and another near the C V absorption line at 33.9 Å. The 32.5 Å feature is most likely due to small residuals in the RGS calibration, because it is much sharper and narrower than the other emission / absorption features. Its wavelength does not correspond to known major transitions. Also the O VI absorption line at 22.8 Å is not well-fitted, possibly due to blending with the O VII f narrow emission line.

3.4.4 Absorption measure distribution (AMD)

There has been a debate in the literature about whether the absorption measure distribution defined here as $A(\xi) \equiv \mathrm{d}N_\mathrm{H}/\mathrm{d}\xi$ is a smooth distribution spanning several decades in ξ (see e.g. Steenbrugge et al. 2005) or consists of a limited number of discrete components (see e.g. Costantini et al. 2007b, Krongold et al. 2003).

We tested both alternatives as follows. We considered the total ionic column densities derived from Model 1 (see Table 3.4), regardless of their velocity, and fit them to a model using discrete components and to a model with a continuous distribution. We simultaneously solved for the abundances of the elements.

For Model 1, there is some arbitrariness in the assignment of ions to the two velocity components, in particular near the ionization parameter $\log \xi = 2.1$ at the division, as for those ions both velocity components will contribute. Thus the observed column densities near that division are higher than the column density of a single velocity component. This could result in the introduction of spurious ionization components or artificially enhanced abundances. We tried to also do this analysis with the results for each velocity component separately, but that is problematic. For Model 2, the error bars on the column densities for individual velocity components

Table 3.4: Predicted and measured Ionic column densities for the most important ions of the outflow for model 1 and model 2.

log ξ^a	ion^b	$N^c_{i,obs}$	$N^d_{i,pred}$	$\Delta\chi^e$	A^f	B^g	C^h	D^i	E^j	$N^k_{i,obs,v1}$	$N^l_{i,obs,v2}$	$N^m_{i,obs,v3}$	v^n_i
−8.50	H I		1.20		79	20	1	0	0				
−8.50	Fe I	< 1.0	0.00		0	0	0	0	0	< 0.1	< 0.1		
−8.50	Fe II	< 0.6	0.00		0	0	0	0	0	< 0.5	< 0.3		
−2.10	Fe III	< 0.1	0.00		100	0	0	0	0	< 0.3	< 0.1		
−1.65	H II		604980		0	1	8	9	81				
−1.48	O III	< 0.3	0.09		99	1	0	0	0	< 0.2	< 0.3		
−1.45	C III		0.10		97	3	0	0	0				
−1.42	Fe IV	< 0.1	0.00		100	0	0	0	0	< 0.1	< 0.2		
−0.95	Fe V	< 0.3	0.01		99	1	0	0	0	< 0.1	< 0.1		
−0.65	O IV	0.9 ± 0.2	0.86	0.1	90	10	0	0	0	0.7 ± 0.2	< 0.1		270 ± 170
−0.60	C IV		0.25		80	20	0	0	0				
−0.55	N IV	0.2 ± 0.2	0.09	0.4	85	15	0	0	0	0.1 ± 0.3	< 0.1		
−0.55	Fe VI	< 0.2	0.03		86	14	0	0	0	< 0.2	< 0.1		
−0.05	O V	1.3 ± 0.2	1.24	0.1	41	59	0	0	0	0.5 ± 0.2	1.0 ± 0.5		− 160 ± 60
0.00	N V	< 0.4	0.11		39	61	0	0	0	< 0.1	< 0.5		
0.05	Fe VII	< 0.1	0.09		28	72	0	0	0	< 0.1	0.2 ± 0.1		
0.15	C V	1.8 ± 0.3	2.01	−0.7	19	78	3	0	0	2.0 ± 0.3	< 0.1		− 10 ± 50
0.42	O VI	1.8 ± 0.2	1.76	0.1	7	91	2	0	0	1.0 ± 0.2	0.7 ± 1.8		− 120 ± 60
0.75	N VI	0.6 ± 0.1	0.62	0.0	3	76	21	0	0	0.6 ± 0.1	0.1 ± 0.1		− 10 ± 50
0.85	Fe VIII	< 0.3	0.17		3	94	3	0	0	< 0.2	< 0.04		
0.92	Ar IX	0.1 ± 0.1	0.01	0.8	0	97	3	0	0	< 0.1	< 0.1		
1.15	O VII	8.5 ± 0.6	8.55	−0.1	0	38	60	1	0	8.1 ± 1.0	1.2 ± 0.3		− 80 ± 20
1.20	C VI	3.6 ± 0.3	3.53	0.4	0	28	63	6	3	3.1 ± 0.4	0.6 ± 0.1		− 50 ± 20
1.22	Ne VIII	0.3 ± 0.3	0.38	−0.4	0	34	66	0	0	0.2 ± 0.1	< 0.1		
1.35	Ar X	0.4 ± 0.2	0.01	1.9	0	34	66	0	0	< 0.5	< 0.1		
1.37	Fe IX	< 1.3	0.09		0	32	68	0	0	< 0.1	< 0.1		

[a] Ionization parameter where the ion has its peak concentration in 10^{-9} W m.
[b] Element and ionization degree.
[c] Observed column density in 10^{20} m^{-2} for model 1.
[d] Predicted column density in 10^{20} m^{-2} for model 1.
[e] Difference in $\Delta\chi$ between predicted and observed column density.
[f] Percentage of ionic column density produced by component A (see Table 3.7).
[g] Percentage of ionic column density produced by component B (see Table 3.7).
[h] Percentage of ionic column density produced by component C (see Table 3.7).
[i] Percentage of ionic column density produced by component D (see Table 3.7).
[j] Percentage of ionic column density produced by component E (see Table 3.7).
[k] Observed column density in 10^{20} m^{-2} for model 2, velocity component 1 ($v = -13 \pm 11$ km s^{-1}) and velocity broadening $\sigma = 125 \pm 8$ km s^{-1}.
[l] Observed column density in 10^{20} m^{-2} for model 2, velocity component 2 ($v = -319 \pm 14$ km s^{-1}) and velocity broadening $\sigma = 107 \pm 9$ km s^{-1}.
[m] Observed column density in 10^{20} m^{-2} for model 2, velocity component 3 ($v = -770 \pm 109$ km s^{-1}) and velocity broadening $\sigma = 160 \pm 120$ km s^{-1}.
[n] Outflow velocity for the individual ion in km s^{-1}. Only ions with a solid measure of the column density are included (i.e. no upper limits).

Table 3.5: Same as Table 3.4 but for more highly ionized ions.

log ξ^a	ion^b	$N^c_{i,o}$	$N^d_{i,p}$	$\Delta\chi^e$	A^f	B^g	C^h	D^i	E^j	N^k_{v1}	N^l_{v2}	N^m_{v3}	v^n_i
1.60	N VII	1.5 ± 0.1	1.51	0.0	0	5	80	10	5	0.9 ± 0.1	0.6 ± 0.1		-120 ± 40
1.65	Fe X	0.2 ± 0.1	0.20	0.5	0	2	98	0	0	< 0.1	0.3 ± 0.1		-350 ± 220
1.71	Ar XI	< 0.1	0.04		0	1	99	0	0	< 0.1	< 0.1		
1.75	Ne IX	5.0 ± 0.6	5.00	0.0	0	1	92	7	0	2.2 ± 0.7	2.0 ± 0.7	0.3 ± 0.2	-160 ± 40
1.85	Fe XI	0.1 ± 0.1	0.29	−1.6	0	0	100	0	0	0.1 ± 0.1	< 0.1		
1.88	O VIII	21.9 ± 2.1	22.0	0.0	0	1	75	16	8	13.5 ± 2.4	5.1 ± 1.5		-100 ± 20
1.97	Fe XII	0.1 ± 0.1	0.26	−2.4	0	0	100	0	0	< 0.1	0.2 ± 0.1		
2.00	Ca XIII	< 0.1	0.18		0	0	96	4	0	< 0.1	< 0.1		
2.04	Fe XIII	0.3 ± 0.1	0.19	1.7	0	0	100	0	0	0.3 ± 0.2	< 0.1		-20 ± 190
2.05	Ar XII	< 0.1	0.06		0	0	98	2	0	< 0.1	< 0.1		
2.10	Fe XIV	0.3 ± 0.1	0.11	3.7	0	0	100	0	0	< 0.1	< 0.1		-370 ± 400
2.15	Fe XV	< 0.1	0.05		0	0	99	1	0	< 0.5	0.2 ± 0.4		
2.20	S XII	0.1 ± 0.1	0.20	−1.1	0	0	95	5	0	0.2 ± 0.1	< 0.1		10 ± 110
2.21	Fe XVI	0.2 ± 0.2	0.04	0.8	0	0	95	5	0	0.1 ± 0.1	< 0.1		-60 ± 230
2.25	Mg XI	1.7 ± 0.5	1.74	0.0	0	0	69	29	2	< 0.6	< 12.6	1.8 ± 1.1	-640 ± 210
2.30	Fe XVII	0.2 ± 0.1	0.27	−1.5	0	0	59	41	0	< 0.1	0.2 ± 0.1		-400 ± 130
2.35	Ca XIV	0.1 ± 0.1	0.13	0.0	0	0	71	29	0	< 0.1	0.2 ± 0.1		-400 ± 150
2.42	S XIII	0.2 ± 0.1	0.09	2.2	0	0	61	39	0	0.1 ± 0.1	0.2 ± 0.1		-230 ± 180
2.42	Ne X	7.9 ± 2.3	7.71	0.1	0	0	34	38	28	< 0.6	9.5 ± 1.4	< 0.3	-270 ± 50
2.51	Fe XVIII	0.6 ± 0.1	0.45	2.0	0	0	11	89	0	< 0.1	0.4 ± 0.1		-360 ± 110
2.60	S XIV	0.1 ± 0.1	0.10	0.2	0	0	10	86	3	< 0.1	0.1 ± 0.2		
2.77	Fe XIX	0.6 ± 0.1	0.66	−0.7	0	0	1	98	1	< 0.5	0.7 ± 0.1		-210 ± 100
3.01	Fe XX	0.5 ± 0.1	0.41	0.8	0	0	0	90	10	0.3 ± 0.1	0.4 ± 0.3		-680 ± 300
3.20	Fe XXI	0.3 ± 0.1	0.30	−0.3	0	0	0	35	65	< 0.1	< 0.1	0.4 ± 0.1	-800 ± 220
3.31	Fe XXII	< 0.3	0.60		0	0	0	3	97	0.2 ± 0.3	< 0.2		
3.41	Fe XXIII	< 0.4	1.39		0	0	0	0	100	< 0.4	< 0.4		
3.52	Fe XXIV	< 2.5	2.83		0	0	0	0	100	< 0.3	< 0.8		

are relatively high, because RGS only partially resolves the lines of each component. This then gives too much uncertainty to deduce conclusive results.

The first model we tested is a discrete model:

$$A(\xi) = \sum_{i=1}^{m} H_i \delta(\xi - \xi_i), \tag{3.2}$$

Where H_i are the total hydrogen column densities of the m components with ionization parameter ξ_i.

From our runs with Cloudy we obtain for each ion j curves for the ion concentration $f_j(\xi)$ relative to hydrogen as a function of ξ, assuming Lodders & Palme (2009) abundances. Given a set of values for ξ_i and H_i, it is then straightforward to predict

Table 3.6: Parameters for model 3.

Comp	log ξ^a	N_H^b	σ^c	v^d	log U^e
B1	0.81 ± 0.07	0.8 ± 0.1	124 ± 20	25 ± 30	−0.73
C1	2.03 ± 0.02	2.6 ± 0.2	193 ± 14	− 43 ± 20	0.49
A2	−0.14 ± 0.13	0.4 ± 0.1	79 ± 26	− 180 ± 41	−1.68
C2	2.20 ± 0.02	4.4 ± 0.5	29 ± 6	− 267 ± 31	0.66
D2	2.62 ± 0.08	1.8 ± 0.5	34 ± 19	− 254 ± 35	1.08
E2	3.26 ± 0.06	6.3 ± 1.2	37 ± 19	− 492 ± 45	1.72

[a] Ionization parameter in 10^{-9} W m.
[b] Column density in units of 10^{24} m^{-2}.
[c] r.m.s. velocity broadening in km s^{-1}
[d] Outflow velocity in km s^{-1}, a negative velocity corresponds to a blueshift.
[e] ionization parameter (as used in UV spectroscopy).

the ionic column densities N_j:

$$N_j = \int_0^\infty A(\xi) B_j f_j(\xi) \mathrm{d}\xi, \tag{3.3}$$

with B_j the abundance in solar units of the parent element of ion j. We solve this system by searching grids of models for different values of ξ_i, and determine the corresponding best-fit column densities H_i from a least-squares fit to the data. The abundances are solved iteratively. We start with solar abundances and solve for H_i. Then for each element we determine its best-fit abundance from a least squares fit of its ionic column densities to the predicted model of the last step. This procedure is repeated a few times and converges rapidly.

It should be noted that since we do not measure hydrogen lines, the hydrogen column densities that we derive are nominal values based on the assumption of on average solar metal−to−hydrogen abundance for the ions involved. In fact, we derive only accurate *relative* metal abundances. Truly absolute abundances should be derived using UV data, but we defer the discussion on abundances to later papers of this series (Steenbrugge et al. 2011, and Arav et al., in prep).

It appears that we obtain the best solution if we take five ionization components into account. Adding a sixth component does not improve the fit significantly, and by deleting one, two or three components χ^2 increases by 6, 16 and 200, respectively (refitting in each case). Our best fit then has $\chi^2 = 42.5$ for 29 ions included in our fit. The predicted model is shown in Table 3.4, together with the individual contributions $\Delta\chi_j$ to χ^2 for each ion (i.e., $\chi^2 = \sum \Delta\chi_j^2$). Negative values for $\Delta\chi_j$ indicate lower observed ionic column densities than the model and positive values higher observed ionic columns. The best−fit parameters are shown in Table 3.7.

We did not include upper limits in our fit, and we also excluded the argon lines because the predicted model is well below the marginal "detections" of Ar IX and Ar X.

Table 3.7: Parameters for the discrete distribution.

Component	$\log \xi^a$	N_H^b
A	-0.33 ± 0.49	0.23 ± 0.09
B	0.71 ± 0.12	0.84 ± 0.10
C	2.01 ± 0.02	4.8 ± 0.4
D	2.79 ± 0.06	5.7 ± 0.9
E	3.60 ± 0.27	54 ± 73

[a] Ionization parameter in 10^{-9} W m.
[b] Column density in units of 10^{24} m^{-2}.

For further discussion, we also include predicted column densities for hydrogen and C III and C IV, although we cannot measure lines from these ions in the RGS band.

Next we consider a continuous AMD. It is impossible to make no a priori assumptions for the shape of $A(\xi)$, but we minimize this as follows. We assume that $\log A(\xi)$ is described by a cubic spline for $\log \xi$ between -3 and 4 with grid points separated by 0.2 in $\log \xi$. The use of logarithms guarantees that $A(\xi)$ is non-negative; the spacing of 0.2 corresponds to the typical scale on which ion concentrations change (making it much smaller causes oversampling with unstable, oscillatory solutions), and the range in ξ covers the ions that are detected in the spectrum. Free parameters of the model are the hydrogen column densities H_i at the grid points and the abundances. We solve for this system using a genetic algorithm (Charbonneau 1995).

We made 200 runs with the algorithm, and kept the 117 runs that resulted in $\chi^2 < \chi^2_{\rm min} + 1$ with $\chi^2_{\rm min} = 39.6$ the best solution. In Fig. 3.9 we show the median of all these 117 good solutions. The figure shows two strong, isolated peaks at $\log \xi = 2.0$ and 2.8, corresponding to components C and D of Table 3.7. At a higher ionization parameter ($\log \xi > 3$), the range of component E of Table 3.7, there is also some AMD, but the detailed structure is essentially unknown: there is a wide spread between the individual solutions that are acceptable. At a lower ionization parameter ($\log \xi < 1$), there is also some AMD but again not a well-determined structure. A hint for the presence of component B is that the median of the acceptable solutions is closer to the upper limit in the range of ξ between $0.4 - 0.8$.

As a final test, we extended the model with discrete components and searched how broad the discrete components are. Replacing the δ-function by a Gaussian in (3.2), we get an upper limit to the σ of the Gaussians of 0.06 and 0.13 in $\log \xi$ for the components C and D, corresponding to a FWHM of 35 and 80%. For the other components, there is no useful constraint.

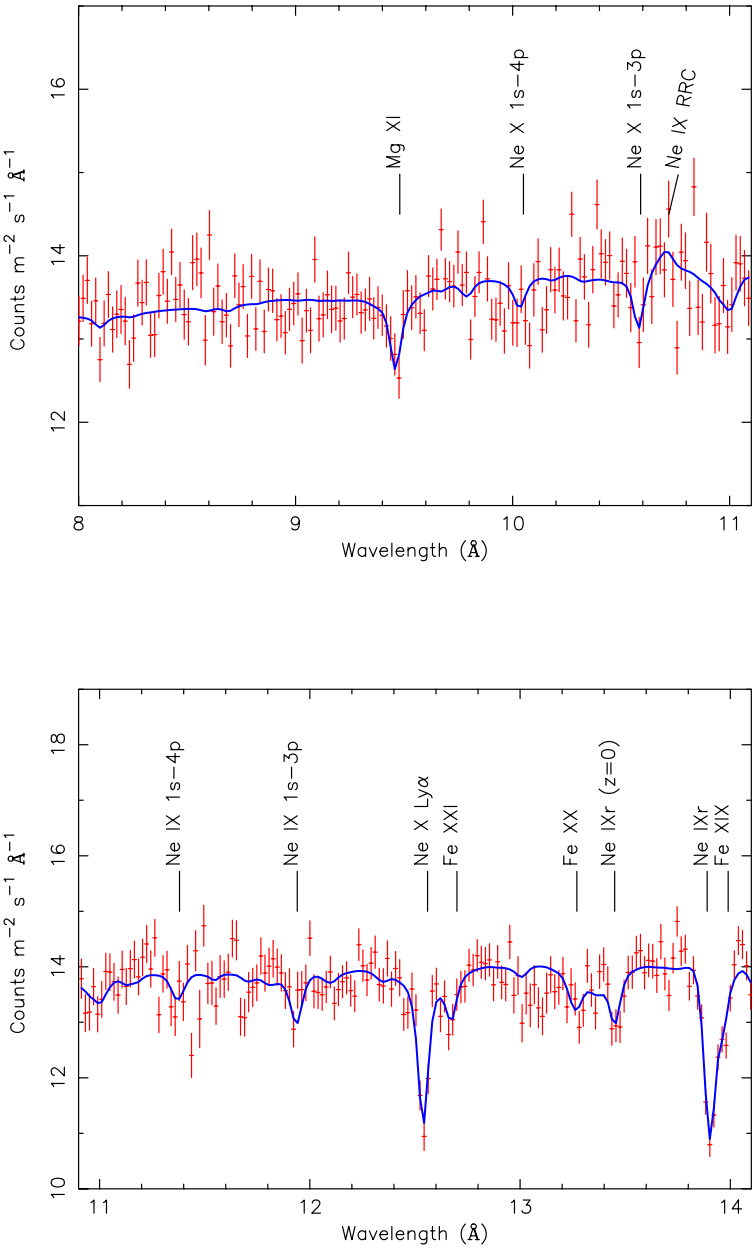

Figure 3.4: The data and the best fit to the RGS spectrum (model 2). The wavelengths shown are the observed wavelengths.

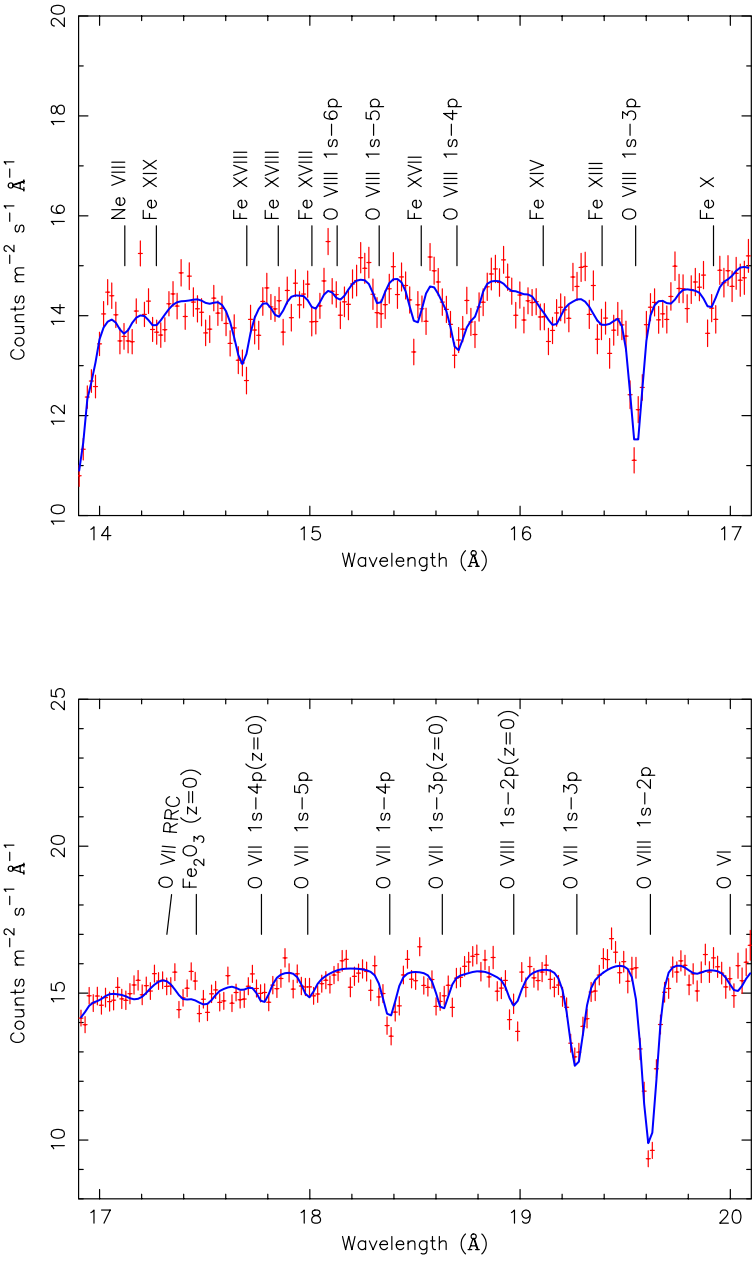

Figure 3.5: RGS spectrum continued.

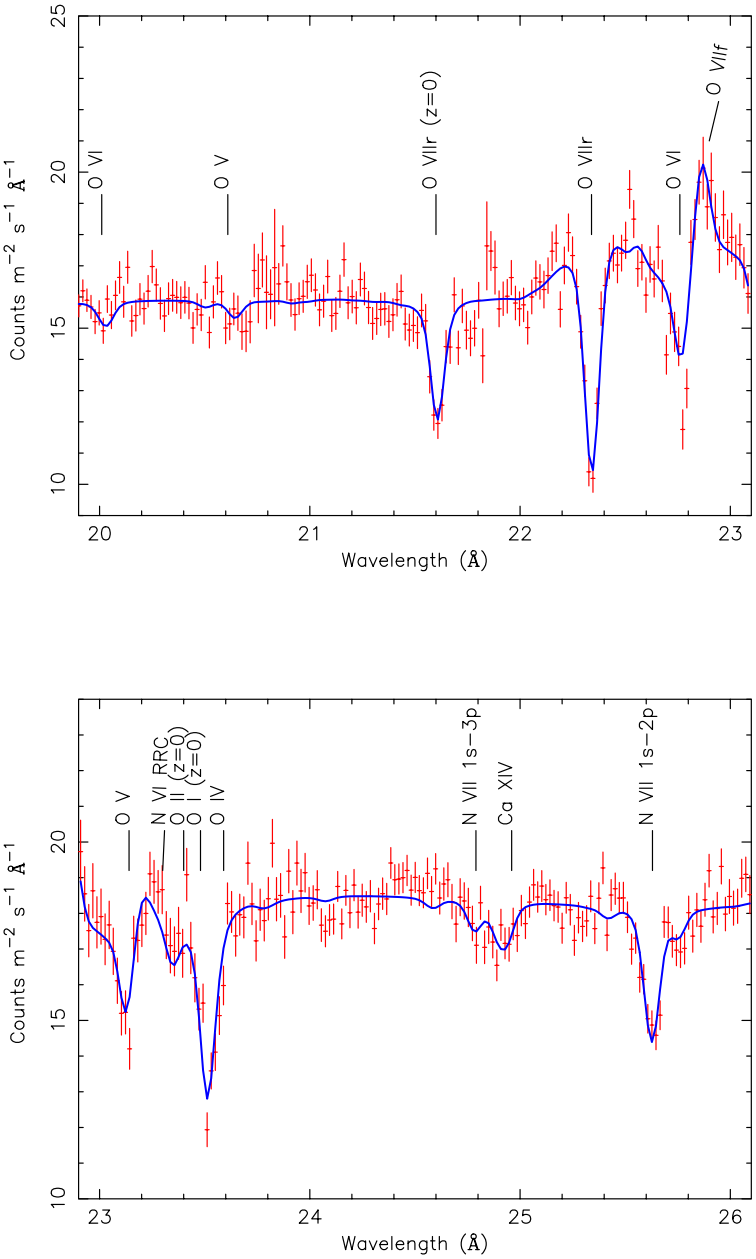

Figure 3.6: RGS spectrum continued.

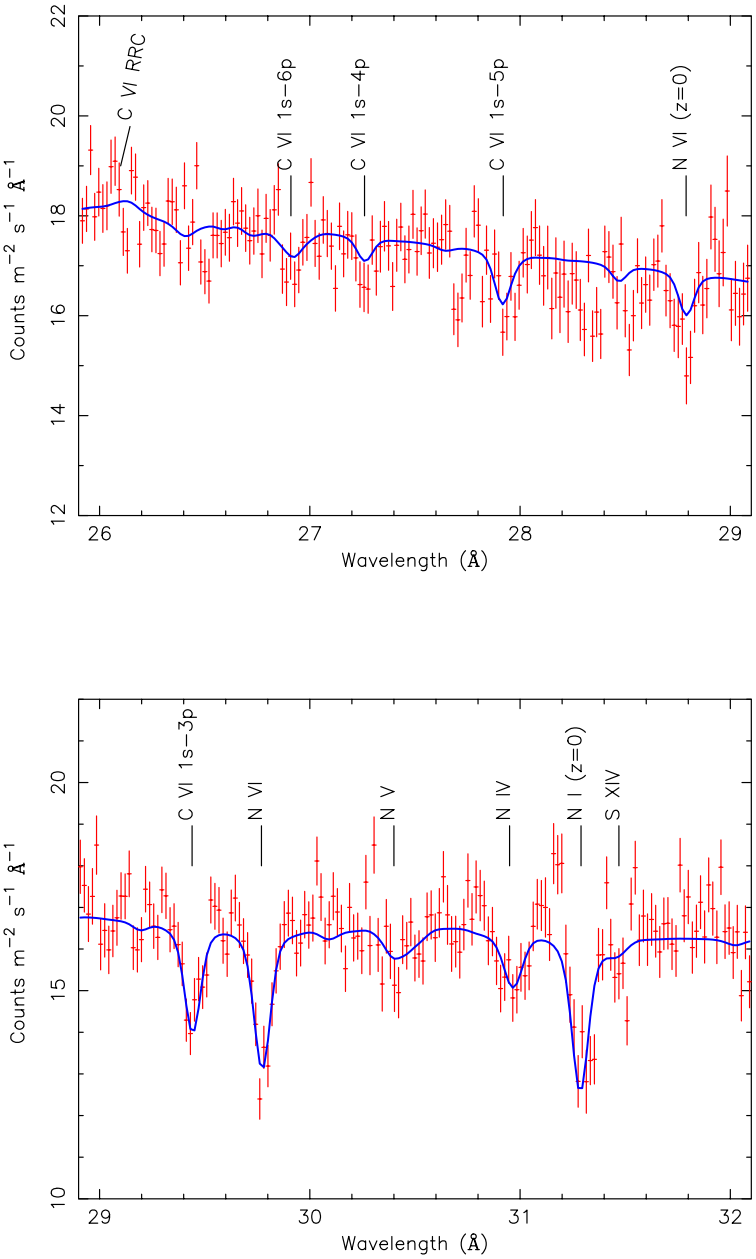

Figure 3.7: RGS spectrum continued.

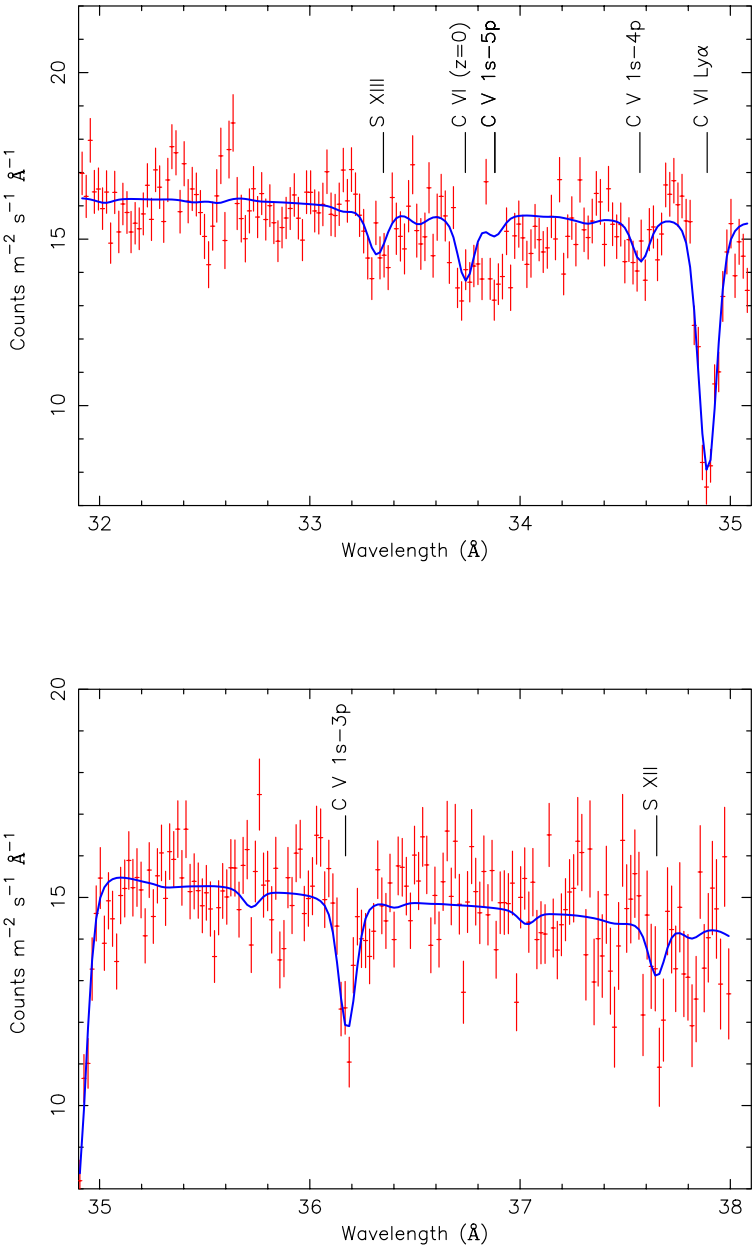

Figure 3.8: RGS spectrum continued.

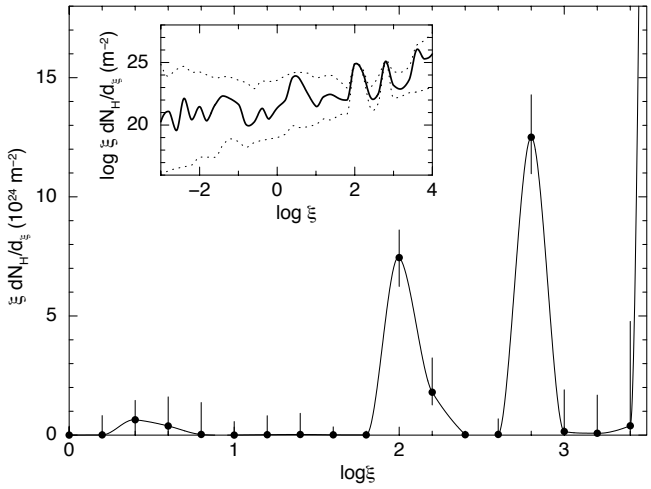

Figure 3.9: Continuous absorption measure distribution plotted as $\xi A(\xi)$ for Mrk 509. Shown is the median of the 117 runs with $\chi^2 < \chi^2_{\rm min} + 1$. Error bars correspond to the minimum and maximum value of the AMD at each value of ξ for those runs with acceptable χ^2. Note the two strong and isolated peaks at $\log \xi = 2.0$ and 2.8, respectively. The inset shows our results on a logarithmic scale for a broader range of ionization parameter; dotted lines connect the minimum and maximum values of all acceptable solutions.

3.5 Discussion

3.5.1 Foreground and emission features

This paper focuses on the properties of the ionized outflow in Mrk 509, but given the quality of the data, a full description and discussion of all the features present in the spectrum is beyond the scope of this paper and will be given in a series of subsequent publications. The only clear detections of narrow emission lines are the O VII forbidden emission line at 22.101 Å, the O VII intercombination line at 21.802 Å, and a narrow Ne IX forbidden emission line at 13.70 Å. The fluxes are consistent with earlier observations (see Chapter 2). We also searched for RRC features of the most prominent ions (C, N, and O) and found several possible weak RRCs. We do not detect any significant absorption due to neutral gas in the host galaxy. This means that we are observing the nucleus directly, which could indicate that we observe Mrk 509 almost face-on, as suggested in previous papers (Phillips et al. 1983, Kriss et al. 2000, Kraemer et al. 2003).

3.5.2 Outflow models

The warm absorber in Mrk 509 (O VIII column density of $\simeq 2 \times 10^{21}$ m^{-2}) is deeper than the one seen in Mrk 279 (3×10^{20} m^{-2}, Costantini et al. 2007b) but shallower with respect to those in NGC 5548 for instance (3×10^{22} m^{-2}, see e.g. Steenbrugge et al. 2005) or NGC 3783 (4×10^{22} m^{-2}, see e.g. Behar et al. 2003). Nevertheless the high quality of this dataset allows for a thorough investigation of the outflow properties. While the main goal of the campaign is to localize the outflow, which requires investigating the ten individual observations, the integrated 600 ks spectrum is crucial for a full description of the properties (such as outflow velocity and ionization structure) of the outflow. To obtain the most accurate information about the true structure of the outflow we now compare the different models of the outflow.

The first model (Model 1) is a very simple description, with only one velocity component for each ion. The velocity dispersion we obtain for the component that includes the O VII and O VIII ions is 158 km s^{-1}. This is larger than what is obtained from the curve of growth analysis using a single velocity component for these ions (96 and 113 km s^{-1}, respectively, Kaastra et al. 2011b). The reason for this difference is that having only one velocity component for these lines is an oversimplification. Adding a second velocity component for all ions (Model 2), improves the fit of the strong oxygen lines (O VII and O VIII), with the sum of the velocity dispersions larger than for the single component case, but the total column density similar (Kaastra et al. 2011b). Thus the total ionic column densities for models 1 and 2 are consistent with each other.

To compare the *slab* models with model 3 we first need to convert the ionic column densities we measure into an equivalent hydrogen column density. There are two ways to do this. One is to assume that every ion occurs at the ionization parameter where its concentration peaks as a function of $\log \xi$. This holds for some ions, but for others there is a wide range of ionization parameters where the ion makes a significant contribution. The alternative is that we take the full AMD method described in Sect. 3.4.4. It is useful to compare these two methods so that we can see if there are major differences in the results and if these possible differences affect our conclusions. The results for the first method using Model 2 are shown in Fig. 3.10, for both the slow and fast velocity components. Only ions for which we have a significant column density measurement are shown. The results for the AMD method are shown in Fig. 3.9. What can be seen is that the AMD method clearly shows a discrete distribution of column density as a function of the ionization parameter. There is a clear minimum between the peaks at $\log \xi = 2.0$ and 2.8, where the column density is more than an order of magnitude less than at the two surrounding peaks. This indicates that there is almost no gas present at those intermediate ionization states. The simplified method (the one where we assume that every ion occurs at a single ξ value) does show enhancements near the mean peaks of $\log \xi = 2$ and 2.8, but there are no clear minima in the distribution, although for the fast component there seems to be some hint for a minimum near $\log \xi = 0.5$. What is clear from this comparison is that the simplified method is unable to uncover essential details in the AMD. This is because

not all ions are found at their peak ionization parameters.

Another main difference between the models is that the *slab* models (in contrast to Model 3) yield completely model-independent ionic column densities (i.e. no SED or ionization balance or abundances are assumed). This is an advantage if the atomic data for certain ions are uncertain, as the fit will not try to correct for this by changing the overall fit parameters or by poorly fitting this particular ion. From the measured ionic column densities we then can obtain the distribution of total hydrogen column density as a function of the ionization parameters. However at this step it requires the input of an ionization balance, hence an SED.

Model 3 is a direct fit using the ionization balance to predict the ionic column densities. The advantage of this model compared to Models 1 and 2 is that all ions, including those with a small column density are taken into account, and all the ionic column densities are connected through a physical model. There are fewer free parameters, so in principle a more accurate determination of the following parameters: N_H, ξ, σ and v can be obtained. The AMD method is a good combination of both models because the ionic column densities are determined model independently by the *slab* models. Then the ionization balance is used to produce an AMD and obtain the number and parameters of *xabs* components that are needed to describe the data properly.

Model 3 and the AMD method make use of the ionization balance as determined from the SED. The resulting stability curve for the photoionized gas is shown in Fig. 3.11. Components with the same Ξ (in units of) are in pressure equilibrium. Here Ξ is defined in the following way:

$$\Xi = 9610 \times \xi/T, \tag{3.4}$$

where T is the temperature and ξ is the ionization parameter in 10^{-9} W m. The sections of the curve with a negative slope are unstable to perturbations. Not all components appear to be in pressure balance. For both velocity components the low-ionization gas (A2, B1) is not in pressure equilibrium with the higher ionization gas. This could indicate that the different gas phases are not col−ocated or that other forces (i.e. magnetic) are involved to maintain pressure equilibrium. It appears that most of the outflows in Seyfert 1 galaxies show gaps in the AMD (Behar 2009). This is probably due to (thermal) instabilities in the gas (Holczer et al. 2007). The exact nature of these apparent instabilities is still unclear (although a thermal scenario indeed seems plausible at the moment, based on the cooling curves, such as shown in Fig. 3.11).

3.5.3 Structure of the outflow

Much work has already been done investigating the structure of the ionized outflows in other AGN (see e.g. Steenbrugge et al. 2005, Holczer et al. 2007, Costantini et al. 2007b, for some examples). In most cases a wide range of ionization states has been detected, sketching the picture of a continuous distribution of the hydrogen column density as a function of ξ. However, there are also indications of a lack of ions in

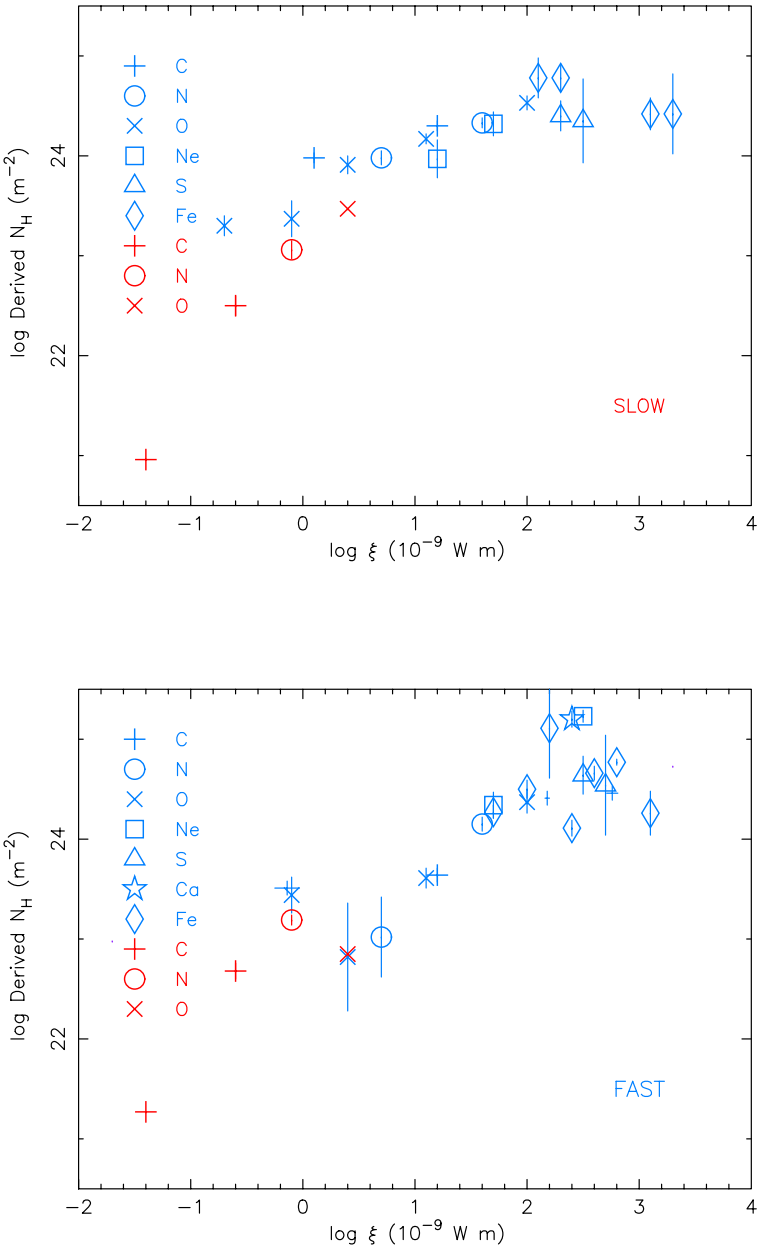

Figure 3.10: The derived hydrogen column density for every detected ion (see Table 3.4). We added archival UV data for C III, C IV, N V, and O VI for comparison (shown in red). The top figure shows the distribution for the slow component, the bottom one shows the same for the fast component.

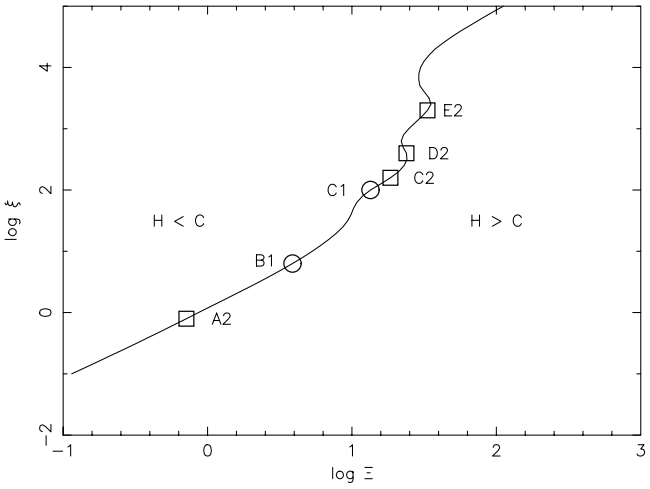

Figure 3.11: The cooling curve derived for the SED with the ionization parameters obtained from Model 3 over-plotted. The circles indicate the ionization parameters for the slow velocity component, while the squares shown are for the fast outflow. Regions where heating (H) or cooling (C) dominate are also indicated.

a certain temperature regime, where the ionized gas is in an unstable region of the cooling curve. In Mrk 509 such unstable regions occur for log ξ between 2.4 and 2.8 and between 3.5 and 4. We have determined that the outflow in Mrk 509 is not continuous, but has discrete components, at least in the range of log $\xi = 2 - 3$. There are two main components, one at log $\xi = 2.0$ and one at 2.8. We also see a clear trend toward increasing column density for higher ionization states.

We first discuss the ionization structure. The most pronounced component in our spectrum is component C (Table 3.7). The ionization parameter and total column density derived from our *slab* fit (Table 3.7), as well as the direct *xabs* fit (Table 3.6), are fully consistent. From the analysis in Sect. 3.4.4 we find that this component is discrete and spans a very narrow range in ionization parameter: the FWHM is 35%. Interestingly, according to our model (Table 3.4) component C contributes 50% or more to the total ionic column density of 17 of the detected ions in our data set. Those ions span a range of log $\xi = 1.15$ (O VII) to 2.42 (S XIII) in ionization parameter (see first column of Table 3.4).

The next most important component is component D at log $\xi = 2.79$. It is responsible for the more highly ionized iron (up to Fe XX) and the sulfur ions. It is mainly visible in the high−velocity component. Again the direct *xabs* fit and the derived ionization parameter are fully consistent with each other, but the column

density obtained from the *xabs* fit is smaller by a factor of 3. This could be due to *xabs* component C2 ($\log \xi = 2.2$), which also produces ions present in component D ($\log \xi = 2.79$). The other important component is B, which is responsible for most of the lower ionized carbon, nitrogen and oxygen ions. The ionization parameter and column density are fully consistent for both the derived model and the direct *xabs* fit.

Components A and E are also fully consistent with our Model 3, however they are only based on a few ions, so their exact column densities and ionization parameters are uncertain. Especially for the low-ionized gas, the lack of a strong UTA in Mrk 509 means that we only have upper limits on the column densities of the low ionized iron ions, up to Fe x. This is also why the AMD distribution shown in Fig. 3.9 has large uncertainties below $\log \xi = 0$.

Earlier observations have detected only a few of the five components shown in Table 3.7, owing to the poorer quality of the data. Using the Chandra HETGS, Yaqoob et al. (2003) detected mainly component C, since the sensitivity of the HETGS is limited at longer wavelengths and component C is the strongest component. Smith et al. (2007) detected mainly component B2, C (mixture C1 and C2), and D2 (possibly blended with E2). The outflow velocities in their analysis are different, as mentioned before, and they observe an inverse correlation between the outflow velocity and the ionization parameter. This analysis was based on the 2000 and 2001 archival data. Detmers et al. (2010) analyzed earlier archival data (2005 and 2006) of Mrk 509 and found component B (possible mixture of the velocity components), C1, and D2 (possibly blended with E2). It is clear from these comparisons that, although all these earlier observations detected the main components of the outflow, in order to obtain a more complete picture of the outflow, we need a high−quality spectrum, like the one shown in this paper.

Two of the three velocity components that we detected are consistent with earlier results, including the UV data (Kriss et al. 2000, Yaqoob et al. 2003, Kraemer et al. 2003), and they correspond to the two main groups of UV velocity components, one at systemic velocity and the other at $-$ 370 km s^{-1}. Also in the X-ray regime, there is evidence of multiple ionization states for the same outflow velocity, such as components C2 and D2 in Table 3.6. Also there are components that show a similar ionization state, but different outflow velocity, i.e. components C1 and C2 in Table 3.6. Due to the almost zero outflow velocity of components B1 and C1, one could argue that these may be related to the ISM of the host galaxy. The UV spectra, with their much higher spectral resolution, can unravel the outflow, ISM, and redshifted high−velocity clouds (Kriss et al. 2011).Generally speaking, the ionization parameter of the UV components is much lower than those of the X-ray components detected here. This could indicate that the UV and X-ray absorbers are co−spatial, but have different densities. A full discussion of the connection between the UV and X-ray absorbers, as well as the geometry of the absorber, will be presented in Ebrero et al. (2011), where the simultaneous HST COS and Chandra LETGS data will be compared. We do not clearly detect the 200 km s^{-1} redshifted component, which was found in the UV data (velocity component 7 of Kriss et al. 2000). There is some indication that there could be an O vi component at that velocity. There is some extra absorption at

the red side of the line in Fig 3.6 at 22.78 Å. We only obtain an upper limit for the O VI column density in this velocity component of 10^{20} m^{-2}. However, this is consistent with the lower limit from the UV data, which is 10^{19} m^{-2}.

The highest velocity outflow component is only significantly detected in two ions (Mg XI and Fe XXI). Figure 3.12 shows the two absorption lines fitted with a − 770 km s^{-1} velocity and a − 300 km s^{-1} velocity (just as component two in model 2). The improvement using the − 770 km s^{-1} component is $\Delta\chi^2 = 16$. We checked whether this component is also detected in other ions, but most of them (apart from Ne IX) only yield upper limits to the ionic column density. We checked that the line profiles are the same for the separate RGS 1 and RGS 2 spectra and also for the first and second order spectra. In all cases the line profile is consistent with a 770 km s^{-1} blueshift. Also a possible Mg XI forbidden emission line cannot play a role here, because it is too far away (about 0.3 Å) to influence the line profile in any way. This velocity component is consistent with an earlier Chandra HETGS observation, where there was an indication of this velocity component (Yaqoob et al. 2003). A proper explanation of why this component is only clearly detected in these two ions and not in other ions with a similar ionization parameter is currently lacking. A trend visible in Table 3.4 and Fig. 3.13 is that the higher ionized ions have a higher outflow velocity. Fitting a constant outflow velocity to the data yields a value of 70 ± 9 km s^{-1} with χ^2 = 72 for 24 d.o.f. A linear fit to the points gives a slope of 0.62 ± 0.07 and improves the χ^2 to 46 for 24 d.o.f. If we instead fit a powerlaw, a relation of $v \simeq \xi^{0.64\pm0.10}$ is obtained, with a total χ^2 of 34 for 24 d.o.f. The MHD models of Fukumura et al. (2010) predict $v \simeq \xi^{0.5}$, which is consistent with the relation found here. However, it has to be noted that due to the blending of multiple velocity components (including gas that might not be outflowing at all), additional uncertainties are introduced that could affect the results. selecting only those ions, which clearly show blueshifts as well as more accurate outflow velocities, would be needed to investigate this trend further. The O IV ion shows a large redshifted velocity, undetected in the other ions. Most likely this is due to the blending of the O IV absorption line with the O I line from the Galactic ISM at $z = 0$. This blend makes it difficult to determine the centroid of the O IV line exactly (Kaastra et al. 2011b).

3.5.4 Density profile

A recent study has used the observed AMD to construct the radial density profile of the outflow in a number of sources (Behar 2009). Such an analysis is justified as long as the AMD is a smooth, continuous function of ξ, with the possible exception of unstable branches of the cooling curve, where gas may disappear to cooler or hotter phases. However in our case such an analysis is not justified, at least not for the range of log ξ between ∼ 2 and 3 (components C and D). Here we clearly see narrow peaks in the AMD. At least for these components, this hints at rather localized regions with a limited density range, rather than to a large−scale outflow. At lower ionization parameters (components A and B), we cannot exclude a continuous distribution, owing to the limitations imposed by the line detection from the relevant ions. For

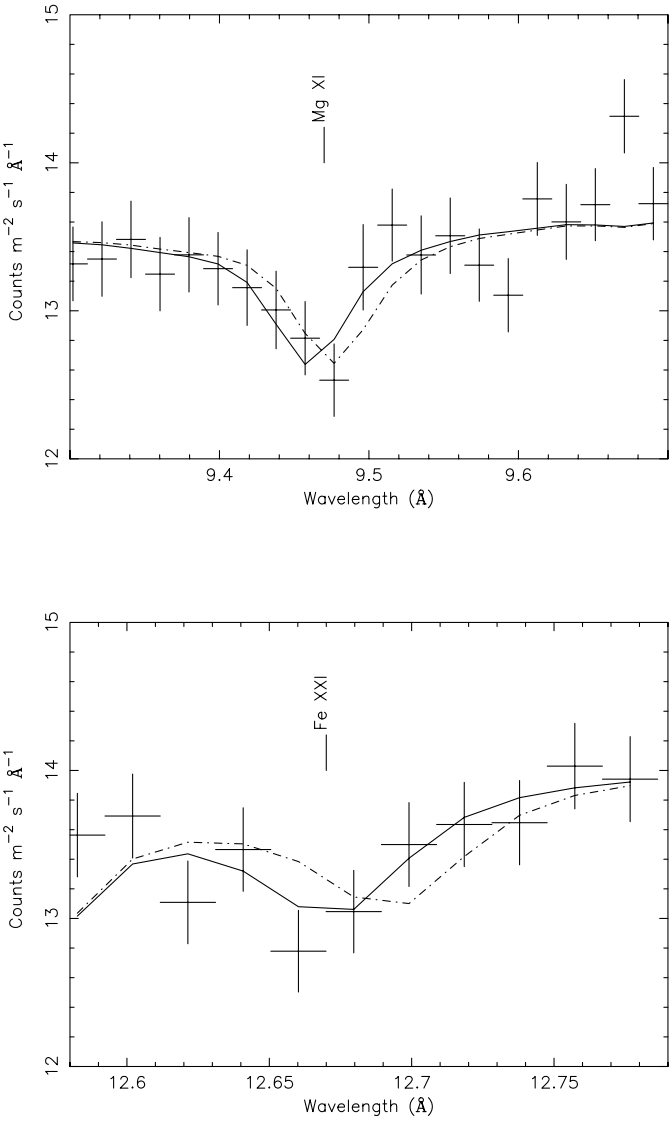

Figure 3.12: The absorption lines of Mg XI and Fe XXI, which show a blueshift of 770 km s^{-1}. The dashed-dotted line shows a model with a blueshift of 300 km s^{-1} and the solid line shows the model with a blueshift of 770 km s^{-1}.

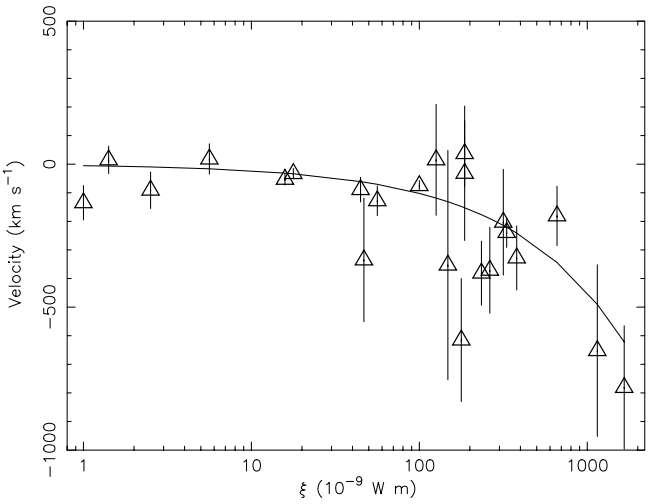

Figure 3.13: Outflow velocity vs. ξ. A general trend of increasing outflow velocity for ions with a higher ionization parameter can be seen. A negative velocity indicates outflow.

these components, the situation is more complex due to the presence of both higher and lower velocity gas. Similarly, based on our analysis we cannot distinguish whether component E has a single component or a broader distribution on the second stable branch of the cooling curve (Fig. 3.11). Gas on the third stable branch, at a very high ionization parameter, escapes our detection completely because of the lack of suitable lines in the RGS band. At best it could show strong lines from Fe XXV or Fe XXVI in the Fe−K band near 6.7 − 7.0 keV, but the limited spectral resolution of EPIC combined with the likely moderate column densities prohibit us from detecting such a component in our data.

3.6 Conclusions

We have presented one of the highest signal-to-noise RGS spectra of an AGN. With the almost unprecedented detail in this dataset, we could detect multiple absorption systems. The ionized absorber of Mrk 509 shows three velocity components, one at -13 ± 11 km s^{-1}, one at -319 km s^{-1}, and a tentative high−velocity component at -770 km s^{-1}. The first two components are consistent with the main absorption troughs in the UV. Thanks to the high−quality spectrum and the accurate column densities obtained for all ions, for the first time it has been shown clearly that the outflow in Mrk 509 in the important range of log ξ between 1−3 cannot be described

by a smooth, continuous absorption measure distribution, but instead shows two strong, discrete peaks. At the highest and lowest ionization parameters, we cannot distinguish between smooth and discrete components. We also have found indications of an increasing outflow velocity versus ionization parameter. Large, dedicated multiwavelength campaigns such as this are the way forward, as this is currently the best method to investigate and characterize the outflows in the local Seyfert galaxies.

Chapter 4

The warm absorber in NGC 5548: The lean years

R.G. Detmers, J.S. Kaastra, E. Costantini, I.M. McHardy and F. Verbunt

Published in Astronomy & Astrophysics, volume 488, pages 831-839, 2008

4.1 Abstract

We study the variability of the warm absorber and the gas responsible for the emission lines in the Seyfert 1 galaxy NGC 5548 to constrain the location and physical properties of these components. Using X-ray spectra acquired using the *Chandra*−LETGS in 2002 and 2005, we study the variability of the ionic column densities and line intensities. We measure a lower O VII forbidden emission line flux in 2005, while the Fe Kα line flux remains constant. The warm absorber is less ionized in 2005, which enbles its location to be constrained to within 7 pc of the central source. Using both the observed variability and the limit on the FWHM of the O VII f line, we constrain the location of the narrow line region to a distance of 1 pc from the central source. The apparent lack of variability in the Fe Kα line flux does enable a unique explanation to be derived.

4.2 Introduction

Active Galactic Nuclei (AGN) have been studied for decades since their discovery over 60 years ago. Mass loss from the nucleus has been known for a long time to

exist in the form of radio jets (see e.g. Peterson 1997) or in outflows showing broad absorption lines (Weymann et al. 1981). However, X-ray and UV observations have shown the presence of outflows in a majority of the moderately luminous Seyfert galaxies (Crenshaw et al. 1999). These outflows are important because they probe the inner regions of AGN and during the lifetime of an AGN they can produce a significant mass loss (Blustin et al. 2005). They can provide us with an understanding of the accretion process onto the supermassive black hole the enrichment of the intergalactic medium (Hamann & Ferland 1999). The physical structure of these outflows and their connection to the other AGN components, such as the supermassive black hole, the accretion disk and the broad and narrow line region (BLR, NLR), is not understood. To learn more about these outflows and the other components of the AGN, variability studies are very important. They enable us to observe how the warm absorber and the emission lines respond to a variable flux from the central source. In addition they place constraints on the locations of the gas in which they originate, and provides us with information about their physical state.

A good object for the study of these processes is the Seyfert 1 galaxy NGC 5548. It is a relatively nearby AGN (z = 0.01676, Crenshaw & Kraemer 1999) and has a relatively high X-ray brightness. Previous UV and X-ray observations have shown the presence of a warm absorber in NGC 5548 (Steenbrugge et al. 2005, Crenshaw et al. 2003). From the kinematics it was concluded that the UV and X-ray absorption lines are part of the same outflow. By comparing a *Chandra*−HETGS and LETGS observation of NGC 5548 in 2002 with an earlier one in acquired 1999, Steenbrugge et al. (2005) conclude that there was no evidence for long-term variability, except for the O v absorption line strength.

We present results derived from a followup *Chandra*−LETGS observation of NGC 5548 acquired in April 2005, which we compare with previous *Chandra*−LETGS and XMM-*Newton* RGS observations (Kaastra et al. 2002c, Steenbrugge et al. 2003, 2005). In all previously mentioned high resolution observations, the variability in the continuum flux was at most a factor of two and no significant variations were detected in the emission line strengths. During our new observation, the source was at a very low flux level from at least March 1 until May 10, as determined using *Swift* observations (Goad & Page 2006), optical observations (Bentz et al. 2007), and this LETGS observation. During this time, the continuum flux was a factor five lower than in 2002. This enabled us to analyze the source for the first time at a very low flux level, and determine changes in spectral features, such as the warm absorber, narrow emission lines, and the iron Fe Kα line. The *Rossi X-ray Timing Explorer (RXTE)* monitoring data of NGC 5548 from 1996 until 2007 are also presented to measure the long-term variability far more accurately than using only spectral observations, which have large gaps in coverage. We discuss the observation and data reduction in Sect. 4.3. Section 4.4 is used to describe the spectral analysis and the variability of the spectral components. We discuss our results in Sect. 4.5 and present our conclusions in Sect. 4.6.

4.3 Data reduction

NGC 5548 was observed for 141 ks with the *Chandra* LETGS (Brinkman et al. 2000) on April 15 and 17 in 2005. The data were reduced as described by Kaastra et al. (2002c). In summary, the data were reduced using the standard CXC pipeline up until the level 1.5 event files. For the steps leading to the final event file, level 2, we followed an independent procedure, which is described in the aforementioned article. The resolution of the LETGS is 0.05 Å and it spans a wavelength range of 1 − 180 Å. Because of the low signal to noise ratio and the Galactic absorption towards NGC 5548, we ignored the data above 80 Å and below 1 Å. The spectrum was analyzed using the SPEX software package (Kaastra et al. 1996)[1]. We used H_0 = 70 km s^{-1} Mpc^{-1}, Ω_m = 0.7 and Ω_Λ = 0.3. Because of the low count rate we calculated the errors using C-statistics (see the XSPEC online manual[2]; we use the form provided by Castor. See also Cash 1979). All errors indicated are 1σ errors, computed for ΔC = 1. The RTXE data were reduced as described by McHardy et al. (2004).

4.4 Spectral Features

Figure 4.1 presents the spectra from the 1999, 2002, and 2005 observations. The flux levels are much lower in the 2005 data, with a 2 − 10 keV continuum flux of 1.47 × 10^{-14} W m^{-2}. To make sure that the spectral lines were analyzed using an adequate local continuum, we fitted the continuum with a spline model. A spline model enabled us to model the continuum between two boundaries b_1 and b_2 using a cubic spline. The limits were 1 Å and 80 Å in our case. The continuum flux y_i is then given on 159 evenly spaced grid points x_i between b_1 and b_2 with a spacing of 0.5 Å between the grid points. The continuum model between the grid points was determined by cubic spline interpolation. The y values of the grid points were derived by spectral fitting. The use of a spline model implies that we did not assume an a priori shape for the continuum, for example a power law or black body continuum. We apply a redshift of 0.01676 to NGC 5548 and correct for Galactic extinction, where the H I column density was fixed to 1.65 × 10^{24} m^{-2} (Nandra et al. 1993). We add various absorption components and narrow emission lines to this continuum (see Sect 3.1 − 3.3). The best fit (including all of the features) has C = 3228 for 2833 degrees of freedom.

4.4.1 Warm Absorber

To model the warm absorber, we use the *slab* model in SPEX (Kaastra et al. 2002a), which calculates the transmission of a thin, irradiated slab of matter with a set of adjustable ionic column densities. We model the optical depth of the absorption lines using Voigt profiles. Our models consist of 3 slab components, for which the ionic

[1] See also http://www.sron.nl/spex

[2] http://heasarc.gsfc.nasa.gov/docs/xanadu/xspec/manual/XSappendixCash.html

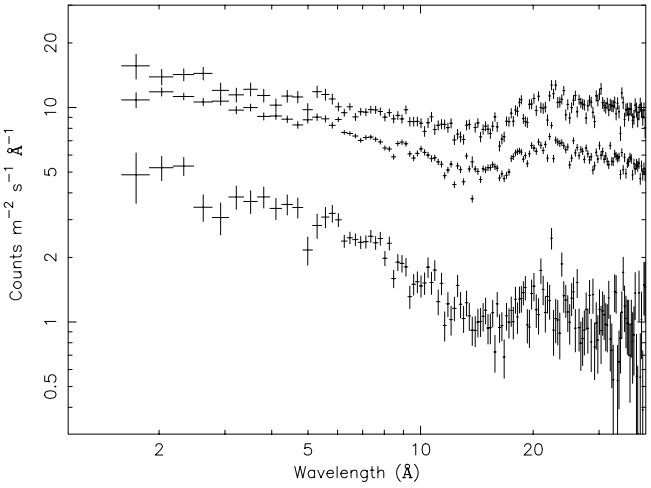

Figure 4.1: The rebinned spectrum of NGC 5548 as taken with the LETGS instrument in 1999 (upper) 2002 (middle) and 2005 (lower).

column densities are allowed to vary and the outflow velocities v fixed to the values given in the previous LETGS study (Steenbrugge et al. 2005). Simultaneous UV observations of NGC 5548 (Crenshaw et al. 2003) provide evidence for five different warm absorber outflow velocities, but due to the lower spectral resolution in the X-ray, only three outflow velocities could be measured reliably by Steenbrugge et al. (2005), namely −1040, −530 and −160 km s^{-1}.

A change in the optical depth of an absorption line can be due to a change in the velocity broadening σ or a change in the ionic column density $N_{\rm ion}$. Alternatively a change in the covering factor of the absorbing gas can also explain the variations in the absorption lines. We assume a covering factor of unity for the absorbing gas (see Sect. 4.5 for discussion). To be certain that the changes we observe in the absorption lines are indeed due to column density changes and not only due to a possible change in σ, we performed two fits, one in which σ was allowed to vary, the other in which σ was fixed to the values reported by Steenbrugge et al. (2005). Figure 4.2 shows the 2002 and 2005 total column densities for both models. The O VIII column density has decreased, while the O IV − O VI column densities have increased. The total column densities are similar for both models. In Table 4.1, we display the 2005 oxygen column densities for both models.

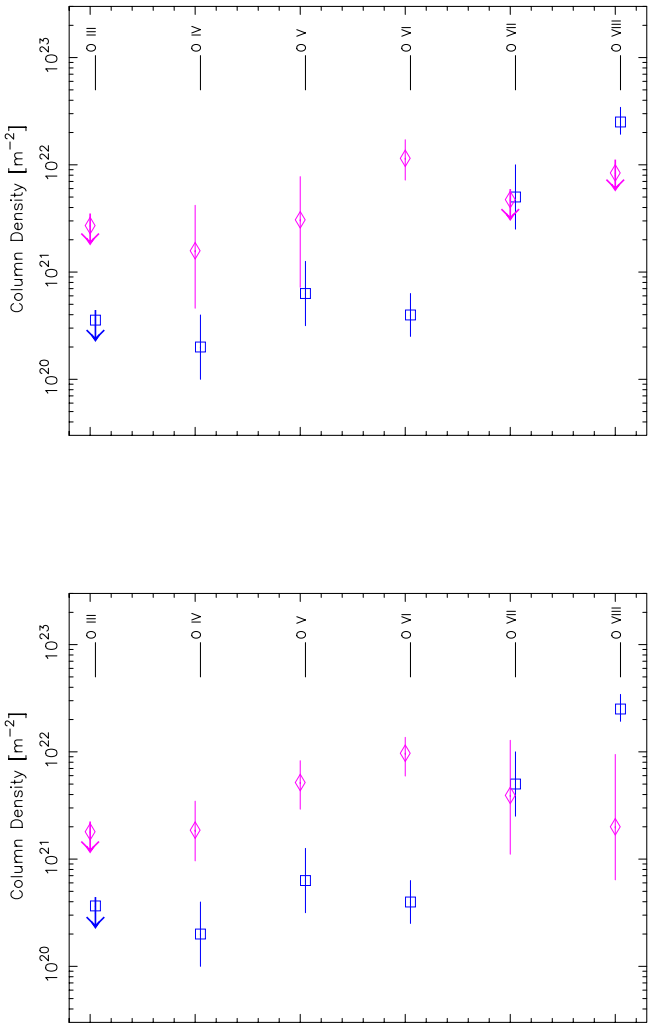

Figure 4.2: Total oxygen column densities as measured with the LETGS instrument in 2002 (rectangles) and 2005 (diamonds). 1σ errors are shown as well, apart from ions for which an upper limit to the total column density can be measured (arrows). The upper panel shows the total column densities for which the velocity broadening σ was allowed to vary , the lower panel where σ was fixed to the values of Steenbrugge et al. (2005).

Table 4.1: Oxygen column densities for the 2005 observation. The logarithms of the column densities are listed in m^{-2}.

v (km s^{-1})	-1040	-530	-160	total
σ (km s^{-1})	127 ± 28	62 ± 21	120 ± 34	
Ion				
O III	< 20.5	< 20.6	< 21.2	< 21.4
O IV	20.8 ± 0.5	< 20.9	21.0 ± 0.5	21.2 ± 0.5
O V	20.9 ± 0.6	< 21.3	21.4 ± 0.5	21.5 ± 0.5
O VI	22.1 ± 0.2	< 20.9	< 21.4	22.1 ± 0.2
O VII	< 21.0	< 20.4	21.1 ± 0.5	< 21.6
O VIII	< 21.1	< 21.7	21.2 ± 0.5	< 21.9
σ (km s^{-1}, fixed)	40	100	90	
O III	< 20.4	< 20.4	< 21.1	< 21.2
O IV	20.6 ± 0.6	< 21.0	21.1 ± 0.4	21.3 ± 0.3
O V	21.3 ± 0.4	20.5 ± 0.7	21.4 ± 0.3	21.7 ± 0.2
O VI	21.9 ± 0.2	< 21.3	21.1 ± 0.4	22.0 ± 0.2
O VII	21.5 ± 0.9	< 20.6	21.0 ± 0.5	21.6 ± 0.5
O VIII	<21.5	< 21.5	21.1 ± 0.9	21.3 ± 0.6

4.4.2 Narrow emission lines

The O VII forbidden line at 22.101 Å is clearly visible in the spectrum of the 2005 observation. We also searched for the Ne IX forbidden line at 13.699 Å, since that line was also detected in earlier observations. Table 4.2 indicates the strengths of both lines in the new spectrum and in earlier observations. We measure a flux of 0.35 ± 0.06 ph m^{-2} s^{-1} for the O VII forbidden emission line and detect a blueshift of -250 ± 70 km s^{-1} for the O VII f line. For the Ne IX forbidden emission line, we measure an upper limit of 0.04 ph m^{-2} s^{-1}, if we assume that the Ne IX line has the same blueshift as the O VII f line. Earlier observations, as described in Sect. 4.4 reported blueshifts of -150 ± 70 km s^{-1} (Steenbrugge et al. 2005, HEG) and -70 ± 100 km s^{-1} (Kaastra et al. 2002c). The LETGS has a wavelength scale uncertainty of 0.01 Å, or 140 km s^{-1} at the O VII f emission line. Taking this and the error on the outflow velocity into account, the blueshift that we detect is negligible, but it is however consistent with the HEG measurement (Steenbrugge et al. 2005). The decrease in flux with respect to previous observations is consistent for both lines, although we are only able to measure an upper limit for the Ne IX f line.

4.4.3 The narrow Fe Kα line

The low continuum flux facilitates the detection of a clear Fe Kα emission line at 6.39 ± 0.03 keV in the spectrum of our LETGS data (Fig. 4.3). Using a Gaussian fit, we measure a flux of 0.55 ± 0.18 ph m^{-2} s^{-1}, which agrees with previous values from

Table 4.2: The unabsorbed flux in ph m^{-2} s^{-1} for the O VII and Ne IX forbidden emission lines for all high resolution spectral observations of NGC 5548. All errors are calculated at a 68 % confidence level.

Year (month)	Instrument	O VII	Ne IX	Reference[1]
1999 (December)	LETGS	0.81±0.13	0.25±0.07	1
2000 (February)	MEG	0.82±0.18	0.09±0.03	1
2000 (December)	RGS	0.65±0.18	0.14±0.07	2
2001 (July)	RGS	0.70±0.16	0.22±0.07	2
2002 (January)	LETGS	0.88±0.08	0.14±0.04	3
2005 (April)	LETGS	0.35±0.06	<0.04	4

[1] References for previous observations: (1) Kaastra et al. (2002c);
(2) Extracted from the public archive, errors include uncertainty due to continuum level;
(3) Steenbrugge et al. (2005); (4) present work

Table 4.3: Fe Kα line parameters. All errors are calculated with 68 % confidence.

	HEG(2000)	EPIC(2001)	HEG(2002)	LETGS(2005)
E (keV)	6.40±0.02	6.39±0.01	6.39±0.01	6.39±0.03
EW (eV)	130±30	60±9	47±11	420±140
FWHM (km s^{-1})	4500±1600	6500±1300	1700±1100	7300±5100
Flux (ph m^{-2} s^{-1})	0.36±0.10	0.38±0.06	0.24±0.06	0.55±0.18
Reference[1]	1	2	3	4

[a] References for previous Fe Kα detections:
(1) Yaqoob et al. (2001); (2) Pounds et al. (2003);
(3) Steenbrugge et al. (2005); (4) present work

Yaqoob et al. (2001), Pounds et al. (2003), and Steenbrugge et al. (2005) as shown in Table 4.3. The equivalent width of the line is 420 ± 140 eV, much larger than measured in those previous observations. There is no evidence for a relativistically broadened Fe Kα emission line profile in our spectrum. We measure a FWHM of 7300 ± 5100 km s^{-1}, which agrees with previous measurements.

4.5 Discussion

4.5.1 The location of the warm absorber

Figure 4.2 shows that the O VIII column density has decreased, while the O IV – O VI column densities have increased between 2002 and 2005, both for σ fixed and σ set free. Some errors in the oxygen column densities in the 2005 spectrum are large, due to a combination of the low statistics and saturation of some of the absorption lines. As shown in Fig. 4.4 there are additional indications that the column density of the lower ionized oxygen ions has increased from 2002 to 2005. The O V absorption line

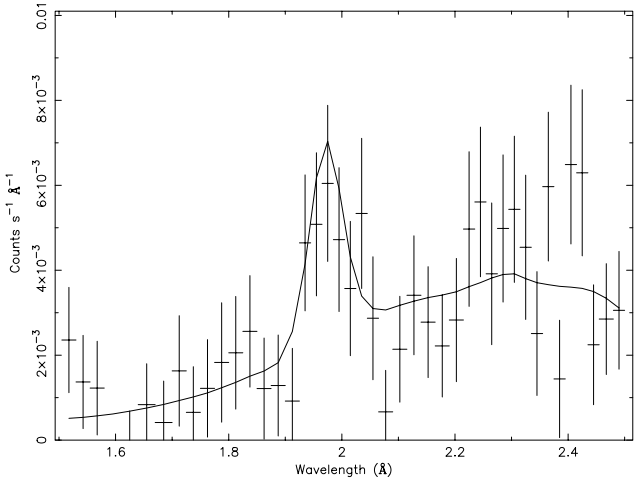

Figure 4.3: The Fe Kα emission line fit for the 2005 observation.

at 22.354 Å is indeed much stronger and broader than in either 1999 or 2002. The equivalent width of the absorption line is 140 ± 30 mÅ, compared to 44 ± 6 mÅ in 2002 and 22 ± 9 mÅ in 1999. Allowing the velocity width σ to vary, the column densities of the individual velocity components do change, but the total column densities do not change significantly (see Table 4.1). This is a further indication that the observed changes in the absorption lines are indeed due to variations in the column density and not only due to a possible change in σ.

In principle, this still leaves open the possibility of a varying covering factor of the X-ray absorbing gas. As shown in UV spectral observations of NGC 5548 (Crenshaw et al. 2003), the covering factor for the various components is not unity. In the UV, it is possible to resolve the different velocity components of the absorber, which is difficult, if not impossible to achieve at the resolution of current X-ray instruments. The size of the X-ray emitting region (10 R_g is estimated to be far smaller than the size of the UV emitting region. Also, the BLR region is measured to be larger in the optical / UV than in the X-rays (see e.g. Costantini et al. 2007a). This, and the fact that column densities for the highly ionized oxygen species have decreased, while column densities of the lowly ionized species have increased, allows us to be confident that the assumption of a covering factor of unity for the X-ray absorbing gas is an accurate one. Therefore the large increase in O VI can be explained by recombination of O VIII and O VII.

The ionization parameter ξ is determined by the ratio of the ionizing flux and the

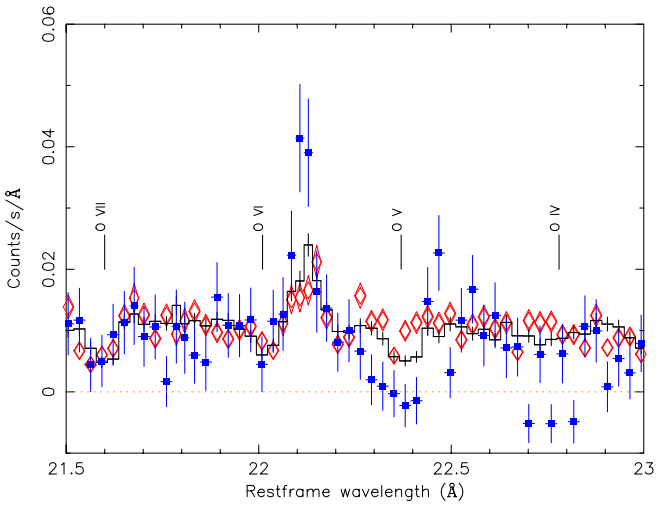

Figure 4.4: Comparison of the 1999 (diamonds), 2002 (solid line) and 2005 (rectangles) spectra, close to the forbidden O VII emission line at 22.101 Å. The deep O V absorption line is visible at 22.354 Å. The 1999 and 2005 spectra have been scaled to the 2002 flux.

density of the gas (Tarter et al. 1969):

$$\xi = \frac{L}{nR^2}. \tag{4.1}$$

Here L is the $1 - 1000$ Rydberg luminosity, n is the density of the gas and r is the distance from the ionizing source. We are only able to determine the product of the density and distance squared, nR^2, from the luminosity and ξ. The luminosity $L = 9.0 \times 10^{36}$ W was measured for the 2002 LETGS observation (Steenbrugge et al. 2005). We first consider changes in the O VIII column density to obtain a lower limit for the density n. The column density of O VIII in the 2002 LETGS observation is 3.39×10^{22} (See model B, Steenbrugge et al. 2005). We assume that the value for the ionization parameter is the one at which the column density of the ion peaks, such that $\log \xi = 1.65$ for O VIII, using the XSTAR code[3] for photoionization modeling. For determining n, we assume that the changes that we detect are due to recombination. The density n scales inversely with the recombination time $\tau_{\rm rec}$ of the gas and depends on the recombination rate of the specific ion (Krolik & Kriss 1995, Bottorff et al. 2000):

$$\tau_{\rm rec}(X_i) = \left(\alpha_{\rm r}(X_i) n \left[\frac{f(X_{i+1})}{f(X_i)} - \frac{\alpha_{\rm r}(X_{i-1})}{\alpha_{\rm r}(X_i)} \right] \right)^{-1}, \tag{4.2}$$

[3]http://heasarc.gsfc.nasa.gov/xstar/xstar.html

where $\alpha_r(X_i)$ is the recombination rate from ion $X_{i=1}$ to ion X_i and $f(X_i)$ is the fraction of element X in ionization state i. If τ_{rec} is positive, it implies that the amount of O VIII increases, by recombination of O IX. If τ_{rec} is negative, then this means that more O VIII is destroyed by recombination to O VII than created by recombination of O IX.

Since the change in column densities occurred between Jan 21 2002 and April 15 2005, the upper limit to τ_{rec} is 1160 days (in the rest frame of the source). The $f(X_{i+1})$ to $f(X_i)$ for i = O VIII ratio can be determined from the ionization parameter ξ. For log ξ = 1.65, the fraction of O IX to O VIII is 0.48. From ξ we derive a temperature of 86 000 K. With this value of T, α_r(O VII) = 8.65×10^{-18} m^3 s^{-1} and α_r(O VIII) = 1.31×10^{-17} m^3 s^{-1} (Nahar 1999). Using these values, we find a lower limit to the density of 4.2×10^9 m^{-3}. Using this limit for n and (4.1), we get an upper limit to the distance of $R < 7$ pc. If we instead use O V to determine the distance, using log ξ = -0.2 and T = 19 000 K, we derive an upper limit of $R < 19$ pc The main uncertainty causing the large upper limits is of course the large gap in the spectral data between 2002 and 2005.

4.5.2 The variable O VII f narrow emission line

The line flux of the O VII f line has decreased from 0.88 ± 0.12 to 0.35 ± 0.06 ph m^{-2} s^{-1} between 2002 and 2005 (Table 4.2). This immediately provides us an upper limit to the distance, namely the light travel distance of 1 pc. A lower limit to the distance of the NLR gas can be obtained from the velocity dispersion and the mass of the supermassive black hole as shown by Netzer (1990):

$$M = \frac{3rV_{FWHM}^2}{4G}, \tag{4.3}$$

where M is the mass of the supermassive black hole, V_{FWHM} is the FWHM of the line and r is the distance of the line emitting region. This assumes an isotropic velocity distribution, which is reasonable, since we cannot obtain any detailed line profile information for the NLR region. Using $M = (6.54 \pm 0.26) \times 10^7$ M$_\odot$ (Bentz et al. 2007) and an upper limit to V_{FWHM} of 560 km s^{-1} obtained by using a Gaussian line model for the O VII f line instead of a delta line, we obtain a lower limit of 1.2 pc for the location of the NLR. If the NLR instead has the same velocity distribution as the BLR in AGN (Peterson et al. 2004), then the lower limit would be 0.9 pc. A similar limit of $\sim$ 1 pc was also derived by Kaastra et al. (2003). Although this lower limit can vary by a factor of a few, depending on the exact velocity distribution and the upper limit can be smaller as it is based on sparse temporal sampling, both limits used constrain the location of the NLR to be about 1 pc. This is the first time that a well-constrained location has been determined, using the combination of variability and line width limits. Optical measurements (Kraemer et al. 1998) indicate that the optical narrow line emission originates in a region within 70 pc, with a high ionization component at 1 pc, in agreement with our findings.

We have ascertained whether $\tau_{\rm rec}$ was much smaller than $\tau_{\rm lt}$, so that the total delay is determined only by $\tau_{\rm lt}$:

$$\tau_{\rm delay} = \tau_{\rm lt} + \tau_{\rm rec}, \tag{4.4}$$

where $\tau_{\rm delay}$ is the total delay time between changes in the continuum flux and changes in the emission line flux, $\tau_{\rm lt}$ is the light travel time through the emitting region, and $\tau_{\rm rec}$ is the recombination timescale. Using Eq. (4.1) with $\log \xi = 1$ (where the O VII fraction in the gas peaks) and $R = 1$ pc, we dervie a lower limit to n of 1 $\times 10^{12}$ m^{-3}. From ξ we can determine the temperature for the gas with $\log \xi = 1$, which is 33000 K. The fraction O VIII / O VII = 0.25 for $\xi = 1$.

Using the O VII and O VI recombination rates from Nahar (1999, $\alpha_{\rm r}$(O VII) = 1.65 $\times 10^{-17}$ m^{3}s^{-1} and $\alpha_{\rm r}$(O VI) = 0.98 $\times 10^{-17}$ m^{3}s^{-1}), the upper limit to $\tau_{\rm rec}$ is 3 days, far less than the 1160 days limit from variability arguments. This implies that the total delay time $\tau_{\rm delay}$ is dependent only on the light travel time $\tau_{\rm lt}$.

4.5.3 The origin of the Fe Kα line

Due to the low continuum flux, we are able to detect the Fe Kα emission line using the LETGS data, even though the LETGS is not optimized for the wavelength range where the line is present, since its spectral resolution is 50 mÅ. The interesting result is that the line flux is in agreement with earlier observations, even though we would have expected a decrease in line flux if the line flux correlates with the continuum flux. Because of the low continuum flux and the constant line flux the equivalent width (EW) of the line is large, 420 ± 140 eV.

Using both HEG measurements of the Fe Kα line (Table 4.3), the weighted average of the FWHM is 2600 ± 900 km s^{-1}. Once again using Eq. (4.3), the line is formed at 0.06 ± 0.04 pc from the central source, assuming again a mass of $\sim 6.54 \times 10^7$ M$_\odot$. At this distance, one would expect that the iron line would also have responded to the lower ionizing flux, since the light travel time is far less than 3 years.

There are at least five possible explanations for the constant flux and corresponding larger EW of the emission line. The first one that can be immediately dismissed is the light-bending close to a black hole (Miniutti & Fabian 2004). The derived distance from the FWHM of the line (0.06 pc, or 19 000 R$_{\rm g}$) is much too large for any light-bending to play a role.

The second reason why the iron line is unaffected by the lower continuum could be that the line consists of multiple unresolved components originating in a broad range of distances from the central source. If we assume that this is the case, then at least part of the emission could originate from a region further away from the central source than 1 pc, for instance the torus structure on a parsec-scale (Antonucci 1993). However, Suganuma et al. (2006) performed infrared reverberation mapping of NGC 5548 and found a time-lag of 47−53 days between the continuum flux in the V band and the IR emission (dust). This would place the dust at $\sim$ 0.04 pc. The dust may of course extent much further outward; so the possibility that Fe K emission is produced by reflection on dust further than 1 pc away from the central source should

therefore be considered. However, if the bulk of the Fe Kα line originated in a source of size close to the pc-scale, the line would be far narrower than observed.

Another explanation is that the continuum was affected by a peak in flux just before our observation was acquired, such that the Fe Kα line had already responded to this increase in continuum flux, but the warm absorber and the narrow emission lines had not. From the LETGS observation alone this cannot be ruled out, although optical observations were also acquired (March 1 till April 10, Bentz et al. 2007) for NGC 5548 just before the LETGS observation. They detected a very low continuum and a weaker Hβ emission line. Since the Hβ line has a time-lag of 6.3 days, any peak in continuum flux should have been evident during the analysis of the optical observations. The RXTE monitoring also did not detect a peak in the months prior to our observation.

The fourth possibility is related to the variation in continuum flux and its effect on the gas, which is studied using the Fe K line. Matt et al. (1993) demonstrated that the strength of the Fe Kα line depends on the ionization parameter ξ of the reflecting gas. They showed that if $\xi \leq 100$, the line strength increases as ξ decreases. Since the continuum flux has decreased suddenly, it is not unreasonable to assume that the ionization state of the gas producing the Fe Kα line will be lower. This implies that the line flux could remain constant while the continuum flux drops.

The final possibility is that, while the continuum flux in the $2 - 10$ keV band has decreased dramatically, the reflection component above 10 keV, which produces the Fe Kα line, may have been far less variable than the continuum. This behavior was in fact detected in several AGN with *Suzaku* (Reeves et al. 2006). The reason for the lack of strong variability in the reflection component is still unknown. Due to the errors in the Fe Kα line flux and the instrumental resolution of the LETGS, we are, however, unable to distinguish among these explanations.

4.5.4 Constraints from RXTE monitoring

Figure 4.5 shows the long timescale light curve of NGC 5548 as observed by *RXTE* from 1996 until 2007. The data have been rebinned into time intervals of one month. As can be seen, the variability on a timescale of a few months can be larger than on longer timescales of years. Long-term changes are still visible. From 2002 onward, the average count rate is $20 - 25$ % lower than that of the earlier years. Applying the information we have on the continuum flux of NGC 5548 between 2002 and 2005, we can refine our estimate of the upper limit to the recombination timescale of the warm absorber.

For an upper limit to the variability timescale of the warm absorber, we currently use an upper limit of 1160 days. Based only on the analysis of two LETGS spectra, this timescale is uncertain. We note that the *RXTE* continuum flux was at approximately the same level in mid-2004 as during the 2002 LETGS observation. If the ionization timescale is short, the ionization state in mid-2004 might have been the same to that in 2002; in which case a more accurate estimate for the recombination timescale may be one year, and even that may be far too long. There is a peak in the X-ray flux

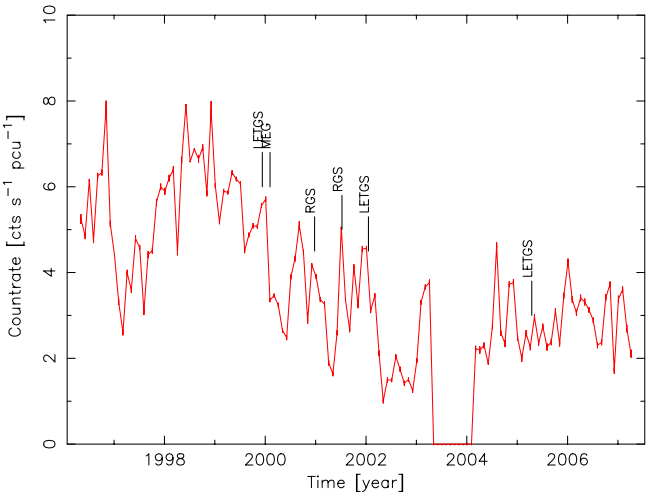

Figure 4.5: *RXTE* lightcurve of NGC 5548, rebinned to one month intervals, spanning from 1996 till 2007. The count rate shown is per PCU detector of the *RXTE*. All 6 spectral observations (see Table 4.2) are shown as well. There is a gap in the data from the beginning of 2003 till 2004, when the source was not monitored by *RXTE*. The errors in the count rates are at the 1 % level.

only a few months before our 2005 observation, so an upper limit of a few months may be even a more accurate estimate indeed. If the recombination timescale is 4 months instead of 1160 days, the upper limit to the warm absorber distance would instead be 2 pc. Since the recombination timescale is so uncertain and probably seriously overestimated, we therefore conclude that the warm absorber is probably much further in than the 7 pc we derived as an upper limit. Further studies, taking time-dependent ionization into account, will enable the changes in the warm absorber to be modeled more accurately as it reacts to the continuum variations observed by *RXTE*.

Concerning the changes in the emission lines, previous observations have measured no observable change in flux for both lines (see Tables 4.2 and 4.3), even though the continuum varied substantially between those observations. This is a clear indication that both emission lines respond to the continuum changes on a long timescale, of years not weeks or months. For the Fe Kα line this would imply that any correlation between the continuum flux and the line flux is more complex than a linear relation between the two. Possible correlations between the emission lines and continuum flux will be investigated further in a future paper.

4.6 Conclusions

This is the first detailed X-ray analysis of NGC 5548 at an extremely low flux level. The warm absorber, which showed little signs of change in previous observations, shows clear signs of recombination to a lower ionized state. We have constrained its location to within 7 pc of the central source, although this is most likely a serious overestimate. The narrow forbidden O VII line has decreased in flux, which along with the limit on the line width, places its location at ~ 1 pc from the central source. This location also agrees with previous estimates for this source. Only the Fe Kα emission line has not responded linearly to the lower continuum flux, the line flux is consistent with earlier observations. The most likely explanations are a change in the ionization state of the reflecting gas or a constant reflection component that is not related closely to the $2 - 10$ keV continuum.

Chapter 5

X-ray narrow line region variability as a geometry probe: The case of NGC 5548

R.G. Detmers, J.S. Kaastra and I.M. McHardy

Published in Astronomy & Astrophysics, volume 504, 409, 2009

5.1 Abstract

We study the long time scale variability of the gas responsible for the X-ray narrow emission lines in the Seyfert 1 galaxy NGC 5548, in order to constrain the location and geometry of the emitting gas. Using X-ray spectra taken with the *Chandra*−LETGS and HETGS instruments and with XMM−*Newton* RGS and combining them with long-term monitoring observations of the *Rossi X-ray Timing Explorer* (RXTE), we perform a correlation analysis in order to try constrain the time scale on which the narrow line emitting gas responds to variations of the continuum flux. With the inclusion of the 2007 *Chandra*−LETGS observation we have an additional observation at an historically low flux level. We conclude that the NLR in NGC 5548 is in the form of an ionization cone, compact in size, and located between 1 and 15 pc from the central source, depending on the exact geometry of the NLR.

5.2 Introduction

Variability in Active Galactic Nuclei (AGN) is currently one of the best methods to study the properties of the gas surrounding super-massive black holes (SMBH). Whether it is the optical Broad-Line Region (BLR) studied by reverberation methods (see e.g. Peterson et al. 2004) or the warm absorber as studied in the UV (for example Kraemer et al. 2006) and X-ray bands (see e.g. Netzer et al. 2003, Krongold et al. 2007), variability allows us to investigate the physical properties and location of the gas without directly resolving the inner regions of AGN.

The narrow line region (NLR) is the region responsible for the narrow forbidden and coronal lines as observed by optical and UV observations (see e.g. Kraemer et al. 1998). The density of this gas is much lower (10^{10-12} m^{-3}) than that of the BLR (10^{16} m^{-3}) and the width of the lines is also much smaller, less than 1000 km s^{-1}. The exact origin of this gas is unknown. The X-ray narrow line region is well known from the observations of various Seyfert 2 galaxies (Kinkhabwala et al. 2002, Bianchi et al. 2006) which show that it consists of photoionized gas in a cone-like geometry of sizes on the order of 100 pc. This gas may be the 'warm absorber' gas seen in emission, although the emission lines show a blueshift in some sources, e.g. NGC 1068 (Kinkhabwala et al. 2002), but not in others, e.g. Mrk 3 (Bianchi et al. 2005).

In Seyfert 1 galaxies it is much harder, with respect to the emission line spectrum observed in Seyfert 2 galaxies, to detect the different narrow emission lines due to the bright continuum which washes out the weaker lines. The strongest line visible in a typical Seyfert 1 high-resolution X-ray spectrum is the O VII forbidden emission line, although other lines are also detected depending on the quality of the spectrum (among others Ne IX f and C V f). No significant blueshift is detected in the emission lines of NGC 5548 (Kaastra et al. 2002c), while NGC 3783 shows evidence of redshifted emission lines, which could be an indication of a P-Cygni like wind (Kaspi et al. 2002, Behar et al. 2003).

Recent work on Mrk 335 (Longinotti et al. 2008), done while the source was in a low state, revealed the presence of emission lines, which the authors place at the location of the optical BLR clouds, which indicates that the emitting region is very compact in size. This a good example of why studying the X-ray NLR in Seyfert 1 galaxies is important. Our understanding of the location and geometry of the X-ray NLR is lacking at the moment, so constraining these is important for determining the origin of the NLR and whether it is connected to the warm absorber. The best method to do this in Type 1 AGN is to take advantage of variability and combine that with high-resolution X-ray spectroscopy.

NGC 5548 is one of the best studied AGN, with optical observations spanning 30 years (Sergeev et al. 2007), seven high-resolution X-ray observations and 11 years of monitoring with the *RXTE* satellite. This makes it one of the best AGN for studying the intrinsic variability of the X-ray NLR. In Chapter 4 we previously constrained the location of the narrow emission line region to within 1 pc of the central source (assuming a spherical NLR). This was based on the line flux change between 2002 and 2005, yielding an upper limit to the size of the emitting region of 3 lightyears. With

the addition of the new 2007 observation we decided to perform a correlation analysis between the emission line fluxes and the continuum flux in order to see if the upper limit of 1 pc could be further refined and how it depends on the geometry of the NLR. We therefore present results derived from seven high-resolution X-ray observations taken by the XMM−*Newton* RGS and the *Chandra*−LETGS and HETGS instruments. These observations give us precise flux measurements for the narrow emission lines. The continuum flux history of NGC 5548 is determined using the *RXTE* observations, which span the period of 1996 to 2007. NGC 5548 has dropped in flux, on average, by a factor of two in the 2 – 10 keV band since 2002. This low "state" lasts up until the last measurement in September 2007. The LETGS observation of 2007 caught the source at the lowest flux level observed so far, providing us with two observations when NGC 5548 was at a low flux level (2005 being the other observation). The long *RXTE* lightcurve gives us the opportunity to search for correlations between the strength of the narrow emission lines and the continuum flux. We discuss the observations used and the data reduction briefly in Sect. 5.3. Sect. 5.4 contains the correlation analysis for the continuum and the emission lines. In Sect. 5.5 we derive the geometry of the NLR. We discuss our results in Sect. 5.6 and present our conclusions in Sect. 5.7.

5.3 Data reduction

We have used data from all 7 observations of NGC 5548 as taken with *Chandra*−LETGS and HETGS and with XMM−*Newton* RGS. Table 5.1 shows the date and the instruments used for each observation. Except for the 2007 LETGS data, all data have been previously published, as indicated in Table 5.1. The LETGS data were reduced as described in Chapter 4 and we have followed the same procedures for fitting the data and error analysis. Briefly, the data were reduced using the standard CXC pipeline up until the level 1.5 event files. After that we follow an independent procedure up to the level 2 event files. For the two RGS observations we have obtained the data using the public archive and used SAS version 8.01 to reduce the data. We use C-statistics for fitting the spectrum. Spectral fitting is done using the SPEX package (Kaastra et al. 1996).

5.4 Data analysis

For all observations we used the following method to obtain the O VII f line parameters. We model the spectrum with a power-law and blackbody component, absorbed by three photoionized components that are modeled using the *xabs* model of SPEX. Also the cosmological redshift and Galactic absorption are taken into account. We model the O VII f line with a Gaussian line, which we put outside the range of the warm absorber gas, so it is only affected by the cosmological redshift and the neutral interstellar absorption. This is the same model which was used in Chapter 4 to model the spectrum.

Table 5.1: High resolution X-ray observations of NGC 5548.

Year (month)	Instrument	Reference[1]
1999 (Dec)	LETGS	1
2000 (Feb)	HETGS	1 + 2
2000 (Dec)	RGS	6
2001 (Jul)	RGS	3 + 6
2002 (Jan)	LETGS + HETGS	4
2005 (Apr)	LETGS	5
2007 (Aug)	LETGS	6

[1] References for observations: (1) Kaastra et al. (2002c); (2) Yaqoob et al. (2001); (3) Steenbrugge et al. (2003); (4) Steenbrugge et al. (2005); (5) Chapter 4; (6) Present work.

Table 5.2: The unabsorbed flux in ph m^{-2} s^{-1} for the O VII forbidden emission line for all high resolution spectral observations of NGC 5548. All errors are calculated at a 68 % confidence level.

Year (month)	O VII
1999 (Dec)	0.81±0.16
2000 (Feb)	0.82±0.18
2000 (Dec)	1.3±0.2
2001 (Jul)	1.1±0.1
2002 (Jan)	0.75±0.07
2005 (Apr)	0.35±0.06
2007 (Aug)	0.27±0.06

The 2007 LETGS observation was taken when the source was at a historically low flux level ($F_{2-10\,keV} = 8.5 \times 10^{-15}$ W m^{-2}), which unfortunately prevented any detailed analysis of the warm absorber due to low statistics. The detected O VII f line is listed in Table 5.2 along with previous detections in the other observations. The O VII f line flux is different with respect to Chapter 4 for the two RGS measures. This is due to the fact that the analysis in Chapter 4 was a preliminary one, which was done using the online RGS BIRD[2] archive. The new fluxes were obtained by using the above method.

5.4.1 Method and Results

Reverberation mapping methods use the cross-correlation of the continuum light curve with the emission line lightcurve. However due to the sparse sampling of the

[2] http://xmm.esac.esa.int/BiRD

emission line data we have chosen another method to address this specific problem.

The observed emission line flux does not respond instantaneously to the continuum flux changes, but due to delay effects in the source region the signal will be smeared out over a time $\tau_{\rm var}$. Therefore we calculated the average continuum flux before each spectral observation at each of a series of time scales. For example, at the 16 days time scale the average flux between the time of an observation and 16 days before that observation is used. We assume that any variability at $\tau \ll \tau_{\rm var}$ is washed out. So we have seven O VII f snapshots and a corresponding average continuum flux for different timescales.

Then we checked for possible correlations at different time scales, the shortest time scale being 7 days and the longest 1280 days. These timescales were chosen because below 7 days the *RXTE* lightcurve does not have enough data points in most of the bins. The upper timescale was chosen to correspond to approximately 3 years, which is the upper limit to the variability timescale (the time between the 2002 and 2005 observations). For the longest timescales, the continuum fluxes derived for some observations (basically the first five) are no longer independent of each other, due to overlap. For example, for the 1999(Dec) and 2000(Feb) observations the average continuum flux on a timescale larger than a few months will be the same, because the *RXTE* data points are the same.

In order to see if there is any correlation between the O VII f fluxes and the average continuum flux on a certain timescale, we perform a Spearman rank coefficient analysis for each timescale. The results are shown in Fig. 5.1. For all timescales the correlations are not significant. Only at the 1280 day timescale do we find a somewhat significant (95 %) correlation, but this method does not include the errors on the average fluxes.

5.4.2 Short term variability

For one of the spectral observations we have a whole week of observing time, namely the 2002 LETGS + HETGS observation (Kaastra et al. 2004, Steenbrugge et al. 2005). As discussed in Kaastra et al. (2004), the source experienced a large flare during the LETGS observation, which allows us to check the short term variability of the O VII f line during that week. During different time segments before, during and after the flare (Kaastra et al. 2004), we fitted a powerlaw between 17 and 24 Å and used a Gaussian line to fit the O VII f emission line. Fig. 5.2 shows the 5 different measurements as well as the fitted average line flux (solid line). All measurements are consistent with the line flux being constant. Despite the factor of 3 variation in continuum flux, the line did not change significantly (less than 25 %). This gives us a lower limit of 3 days for the variability time scale of the emission line region, which is consistent with the lower limit derived from the width of the line (Chapter 4).

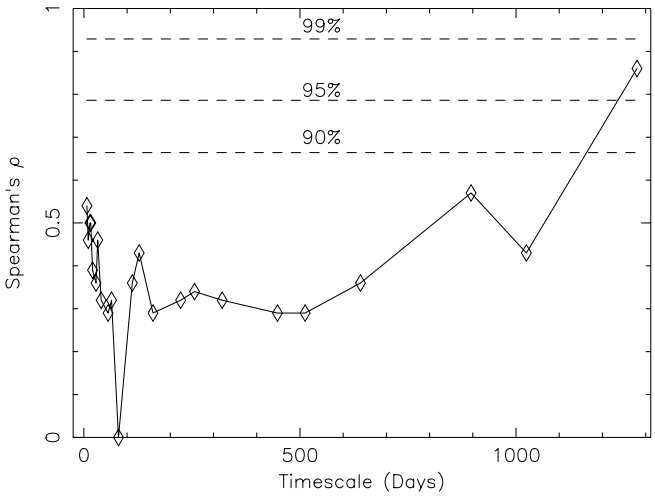

Figure 5.1: Spearman's ρ for different timescales. The timescales tested are indicated by the diamonds, the three dashed lines are the 90, 95 and 99 % probability curves for the correlation degree.

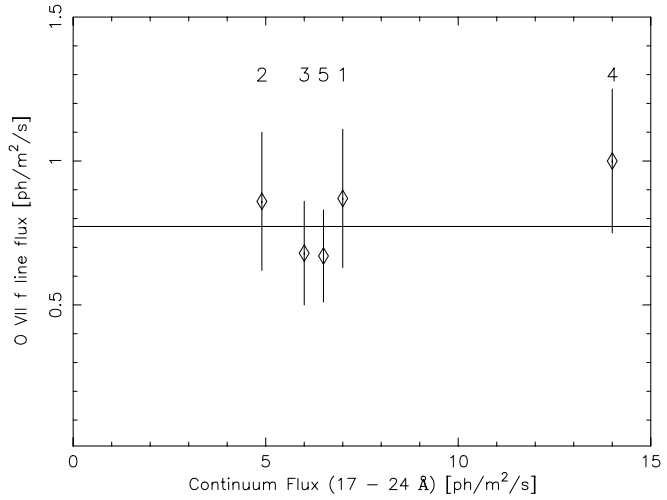

Figure 5.2: The short time scale variability of the O VII f emission line. Labels indicate the time sequence of the data points. The solid line shows the average line flux of all five observations.

5.5 Location and geometry of the NLR

There are four observational quantities based on the O VII f line properties that can be used to constrain the location of the X-ray NLR:

- The variability time $\tau_{\rm var}$
- The velocity width $V_{\rm FWHM}$
- The emission measure Y
- The ratio between the narrow O VII f and O VIII Lyα line flux.

In order to constrain the location of the NLR, we make the following assumptions. First, we assume that the emission arises from a cone-shaped region, between radii R and $R + \Delta R$. The cone has a half opening angle α. Secondly we assume that the ionization parameter ξ can be determined from the ratio of the narrow O VII f and O VIII Lyα lines. The fluxes for these lines are taken from the February 2000 HETGS observation. We therefore make the assumption that the ionization state of the gas is similar in January 2002, since the O VII f line fluxes are similar in 2000 and 2002. From the observed line ratio and using XSTAR photoionization models, we determine that both lines (O VIII and O VII) can be produced by gas with $\log \xi = 1.2 \pm 0.2$. Further we assume that the density drops rapidly with distance from the center (for instance $n \sim R^{-2}$). There are two reasons for making this assumption. First, for a spherical outflow the mass outflow is $\dot{M} \sim n R^2 v$. Most outflow models do not predict a broad range of values for v, implying approximately $n \sim R^{-2}$. The other argument is based on studies of Seyfert 2 ionization cones by Bianchi et al. (2006). They show that density laws similar to $n \sim R^{-2}$ are preferred in order to explain the soft X-ray emission and the [O III] profiles. Since the emission scales as $n^2 V$, this implies that most of the emission comes from a limited range of radii, even when $R \ll R + \Delta R$. Thus in general we can approximate the thickness of the region $\Delta R \ll R$, or in the worst case ΔR and R are of the same order of magnitude. Finally we take the inclination angle i of the cone to be zero, i.e. we look straight into the cone. This approximation is sufficiently accurate for our order of magnitude estimates. Fig. 5.3 shows a sketch of the geometry of the X-ray NLR in NGC 5548.

5.5.1 Analysis

There are several basic equations which are needed in order to constrain the location and geometry of the NLR. First the variability time scale $\tau_{\rm var}$ which is the sum of the recombination time scale and the light travel time:

$$\tau_{\rm var} = \tau_{\rm lt} + \tau_{\rm rec} \tag{5.1}$$

Secondly, the ionization parameter ξ is determined by the ratio of the ionizing flux and the density of the gas (Tarter et al. 1969):

$$\xi = \frac{L}{n R^2}. \tag{5.2}$$

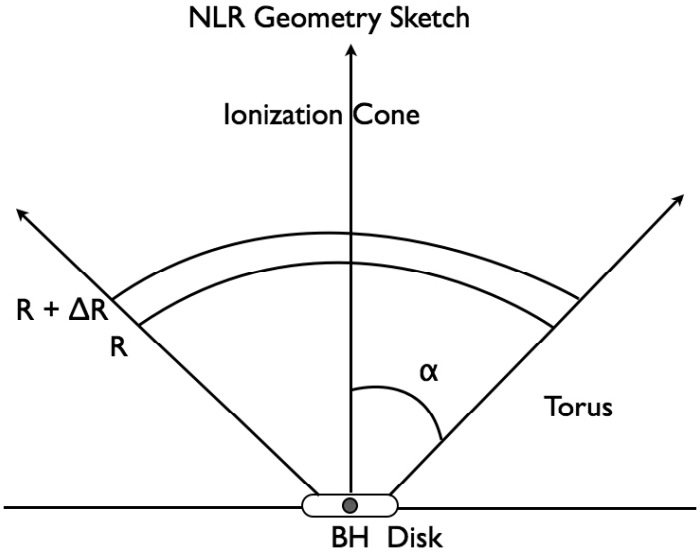

Figure 5.3: A sketch of the geometry of the X-ray NLR region in NGC 5548. The ionization cone has a half-opening angle α and is confined by the torus. The X-ray NLR gas is located in a slab with thickness ΔR at a distance R from the central black hole.

Here L is the $1 - 1000$ Rydberg luminosity, for which we use the value of the 2002 observation (see Table 5.3), R is the distance to the gas and n is the electron density.

Third, the recombination time $\tau_{\rm rec}$ scales inversely with the density n of the gas and depends on the recombination rate of the specific ion (Krolik & Kriss 1995, Bottorff et al. 2000):

$$\tau_{\rm rec} = \left(\alpha_{\rm r}(X_i)\, n\,(X_i) \left[\frac{f(X_{i+1})}{f(X_i)} - \frac{\alpha_{\rm r}(X_{i-1})}{\alpha_{\rm r}(X_i)} \right] \right)^{-1} \equiv a\,(T, \xi)\, n^{-1} \tag{5.3}$$

where $\alpha_{\rm r}(X_i)$ is the recombination rate from ion X_{i+1} to ion X_i and $f(X_i)$ is the fraction of element X in ionization state i.

The light travel time $\tau_{\rm lt}$ depends on the opening angle α in the following way, where we assume that the inclination angle i of the cone with respect to our line of sight is zero, i.e. we are looking straight into the cone:

$$\tau_{\rm lt} = \frac{\frac{1}{c} \int_0^{2\pi} \int_0^{\alpha} \int_R^{R+\Delta R} r(1 - \cos\theta) r^2 \sin\theta \, dr \, d\theta \, d\phi}{\int_0^{2\pi} \int_0^{\alpha} \int_R^{R+\Delta R} r^2 \sin\theta \, dr \, d\theta \, d\phi}. \tag{5.4}$$

Which results in the following expression for the light travel time in the ionization cone:

$$\tau_{\rm lt} = \frac{R}{c} \left(1 - 0.5 \left(\frac{\sin^2 \alpha}{1 - \cos\,\alpha} \right) \right). \tag{5.5}$$

Table 5.3: Important parameters of NGC 5548.

Parameter	Description	Value	Reference[3]
L	Luminosity (1–1000 Ryd)	6.6×10^{36} W	1
$\log \xi$	Ionization parameter	1.2	1
a	Parameter defined in Eq. 5.3	1.64×10^{17} m^{-3} s	1
$M_{\rm BH}$	Black hole mass	6.54×10^{7} M$_\odot$	2
Y	Emission measure	4.3×10^{70} m^{-3}	1

[3] References for parameter values: (1) Present Work; (2) Bentz et al. (2007)

The emission measure Y depends on the hydrogen density n and the emitting volume V as

$$Y = 1.2 n^2 V. \tag{5.6}$$

Where the factor of 1.2 is a consequence of $n_{\rm h} = 0.85\, n_{\rm e}$. The volume V depends on the half-opening angle α in the following way, with the assumption that $\Delta R \ll R$ (see discussion in Sect. 5.6):

$$V \simeq 2\pi\,(1 - \cos\alpha) f \frac{\Delta R}{R} R^3, \tag{5.7}$$

with f the filling factor of the emitting gas.

If we assume that the NLR gas is moving in random Keplerian orbits and has an isotropic velocity distribution, we can determine the minimum distance from the upper limit on the line width of the O VII f emission line using the following equation (Netzer 1990):

$$V_{\rm FWHM} = \left(\frac{4GM}{3R}\right)^{0.5}, \tag{5.8}$$

with M the mass of the supermassive black hole and $V_{\rm FWHM}$ the FWHM of the line.

We use the observed luminosity of the O VII f line ($L_{\rm O\,VII\,f} = 5 \times 10^{33}$ W) to determine Y. This is done using an XSTAR run with $\log \xi = 1.2$, $L = 6.6{\times}10^{36}$ W and a temperature $T = 35\,000$ K (Steenbrugge et al. 2005). We obtain $Y = 4.3 \times 10^{70}$ m^{-3}.

Inserting the observed parameter values as listed in Table 5.3 into (5.2) - (5.1), these equations can be rewritten as functions of R and α only:

- $n\,(\mathrm{m}^{-3}) = 4.4 \times 10^{11}\, R^{-2}$
- $\tau_{\rm rec}\,(\mathrm{yr}) = 0.012\, R^2$
- $\tau_{\rm lt}\,(\mathrm{yr}) = 3.3 \left(1 - 0.5 \left(\frac{\sin^2\alpha}{1-\cos\alpha}\right)\right) R$
- $V\,(\mathrm{pc}^3) = 0.0064\, R^4$

- $f\,\frac{\Delta R}{R} = 1.02 \times 10^{-3}\,\frac{R}{(1-\cos\alpha)}$
- $V_{\rm FWHM}\,({\rm km\,s^{-1}}) = 610\,R^{-0.5}$
- $\tau_{\rm var}\,({\rm yr}) = 3.3\,R\left(1 - 0.5\left(\frac{\sin^2\alpha}{1-\cos\alpha}\right)\right) + 0.012\,R^2$

Where R is in pc in these expressions.

The limits on the three observational quantities that can be used to constrain the location of the X-ray NLR are:

- $V_{\rm FWHM} \leq 560$ km s^{-1} (from Gaussian fit to emission line)
- $f\,\frac{\Delta R}{R} \leq 1$ (by definition due to density assumption)
- $\tau_{\rm var} \leq 3$ years (see Chapter 4)

From $V_{\rm FWHM}$ we obtain a lower limit of $R = 1.2$ pc. The $f\,\frac{\Delta R}{R}$ constraint leads to an upper limit of $R \leq 2041\,(1-\cos\alpha)$ pc. The limit on R based on $\tau_{\rm var}$ is a quadratic equation which depends on the opening angle α; it is shown in Fig. 5.4, together with all other constraints on R. The gray area shows the allowed geometry of the emitting gas, based on the above three constraints. These limits can in principal be tightened using additional information based on general properties of ionization cones in AGN.

We can further constrain the location of the NLR if we assume that the warm absorber and the narrow line emitting gas are one and the same. The average column density can be written as

$$N_H = n\,R\,f\,\frac{\Delta R}{R}. \tag{5.9}$$

Using the expression for $f\,\frac{\Delta R}{R}$ obtained earlier ((5.6) and (5.7)) we can rewrite (5.9) into

$$N_H = \frac{Y\,\xi}{2.4\,\pi\,L\,(1\,-\,\cos\alpha)} \tag{5.10}$$

For α between 3 degrees and 120 degrees (see Fig. 5.4), we find N_H values for the emitting gas between 10^{28} and 10^{25} m^{-2} respectively. By comparing this column density to the observed absorption column density we can determine if the NLR gas and the warm absorber gas could be the same. The observed column density of gas with $\log\,\xi = 1.2$ is 5×10^{24} m^{-2} (see fig. 5.4, Steenbrugge et al. 2005). So given the uncertainties (factor ~ 2–3) attached to the above method, we conclude that the warm absorber gas and the NLR gas could be one and the same, especially if we take into account that the covering factor f is likely less than one (only 50% of the Seyfert 1 galaxies have a warm absorber.)

If we make the assumption that the gas that produces the O VI narrow lines also produces the X-ray narrow lines, we get an immediate estimate of the distance from the FWHM of the O VI lines, since they are resolved in the UV. Depending on the

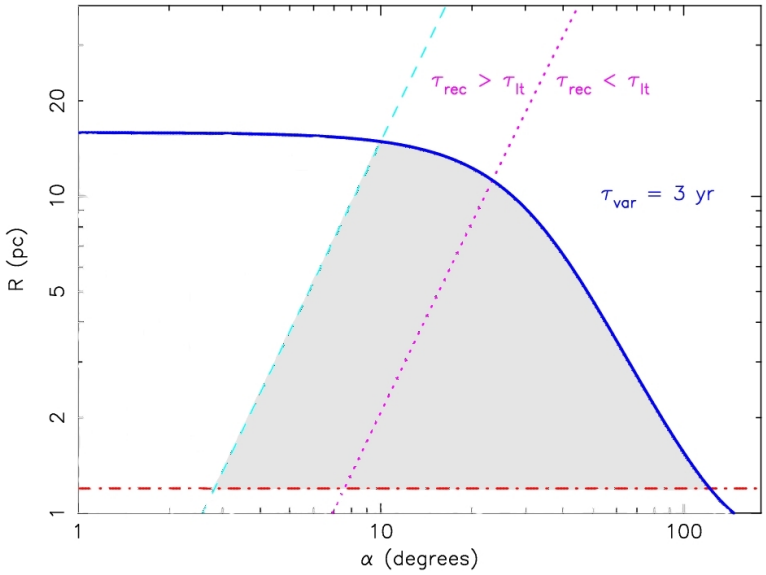

Figure 5.4: The geometry of the NLR, based on an ionization cone model with half opening angle α. The dotted-dashed line on the bottom is the lower limit to the distance as determined from the width of the O VII f line. The left dashed line is the limit on the filling factor of the emitting gas (Eq. 5.7). The thick solid line is the upper limit on the distance as derived from the variability time scale. The gray area indicates the allowed range for R and α. The dotted line on the right indicates where $\tau_{lt} = \tau_{rec}$. Due to the uncertainty in ξ, there is a typical formal uncertainty of 30 % in the R value of the solid curve.

assumed model (covered or uncovered NLR, see Brotherton et al. 2002), the FWHM is either 432 ± 12 km s^{-1} or 658 ± 9 km s^{-1}. These values lead to estimates of R of 2 pc or 0.9 pc, respectively.

From the minimum value for R of 1.2 pc, it follows that the recombination time scale of the O VII f emitting gas is at least 50 days. However from the lack of response of the O VII f line to the continuum flux on different timescales we can in principle refine the lower limit of response timescale τ_{var}. Even though the continuum for the first 5 observations can vary a factor 1.5 between each observation up to a timescale of 600 days, the O VII f line flux is consistent with being constant throughout these five observations. However the line flux for the two RGS observation is a factor of 1.5 higher than the others, if the errors are not considered. This is consistent with the picture that there can be small variations in the line flux on smaller timescales than 3 years, but that a large drop in average continuum flux for a long period is needed for the O VII f line to respond significantly (like in the last two observations in 2005 and 2007). There is also the question of whether the gas is in ionization equilibrium. The continuum of NGC 5548 varies on time scales as fast as ~ 1 day, with a relative amplitude of order unity (see also Sect. 5.4.2). Therefore, strictly

speaking, the gas cannot be in ionization equilibrium. However, it can be considered to be in quasi-equilibrium with the average continuum $\sim \tau_{\rm rec}$ earlier.

5.6 Discussion

From Fig. 5.4 we can already rule out several options for the geometry of the NLR. A spherical NLR is not possible, since the opening angle α is 180 degrees in that case. The upper limit on $\tau_{\rm var}$ along with the lower limit from $V_{\rm FWHM}$ rule out a half opening angle larger than $\sim$ 100 degrees, but anything larger than 90 degrees is unlikely, considering that the accretion disk is located at α = 90 degrees and thus blocks the line of sight to the other side. Therefore the most likely geometry for the NLR is an ionization cone, as observed in Seyfert 2 galaxies. The half opening angle of these ionization cones can typically vary between 20 and 45 degrees (Schmitt et al. 2001). Applying this additional constraint to the location of the NLR, we find that R is between 1.2 and 12 pc.

The above constraints on the location have been obtained with the assumption that $n \sim R^{-2}$. This assumption is based on a constant mass outflow rate and on Seyfert 2 ionization cone studies (Bianchi et al. 2006). Since we are not sure if the NLR is really outflowing, the second argument is the strongest indication that this assumption is correct as it is based on photoionization studies by comparing the optical [O III] emitting region to the soft X-ray emitting region. They conclude that constant density models are excluded and that a steep density profile ($n \sim r^{-2}$) is preferred. Another study of six Seyfert 1 galaxies in the optical show different results however for the density slopes (Bennert et al. 2006a). Some Seyfert 1 galaxies show a slope $\sim r^{-1}$, others a slope $\sim r^{-2}$. When compared to Seyfert 2 galaxies in their sample, the Seyfert 1's on average show a steeper slope, but given the fact that there are only six sources, the scatter for individual sources can be quite large. Also it is not certain that the extended NLR that they probe (scales of $\sim$ 100's pc) is the same gas as the high-ionization X-ray gas we detect in NGC 5548. A better method to investigate the NLR properties would be using a grid of photoionization models for NGC 5548, but given the fact that we only have two lines in the X-ray and two lines in the UV to model, this would be too detailed for the current data we have. A future article where this analysis can be extended to include other Type 1 AGN would be better suited for this level of detail.

The constraint on the NLR distance in NGC 5548 places it at a much greater distance than Longinotti et al. (2008) obtained in Mrk 335. However the line ratios of the oxygen triplet are different in Mrk 335 than in NGC 5548. The intercombination line is stronger than the forbidden line in Mrk 335, while in NGC 5548 this clearly is not the case. The line widths they find for the emission lines are also a factor of $\sim$ 3 greater than those of the O VII f in NGC 5548. These two clues tell us that the emitting gas most likely is not the same in both sources. The gas in Mrk 335, has much more in common with the BLR (high density, large velocity width) than the NLR which we observe in NGC 5548.

From the observed warm absorber column density, we conclude that the warm absorber and the NLR gas could be the same given the uncertainties on the column density of the absorber ($\sim$ 30%). However, the connection between absorber and emitter is still uncertain at this moment and will be hard to establish without first independently establish the geometry of both the absorbing and the emitting gas.

The connection between the narrow UV line emitting gas and the X-ray emitting gas is speculative at best at this moment, although the FWHM of both systems is similar and both the UV and X-ray line ratios can be produced by gas with a single ionization parameter ($\log \xi = 0.9$). A more detailed photoionization model, which takes into account the warm absorber and the line emission in both UV and X-ray, with the correct geometry and outflow velocities and time-dependent ionization effects, would be invaluable in comparing the UV and X-ray spectral information from the observations to the model predictions. However such a work is beyond the scope of this paper, since its main purpose is demonstrating the usage of variability as a geometry probe of the X-ray NLR. Recently, Crenshaw et al. (2009) have studied high-resolution UV spectra of NGC 5548, including one in an extremely low flux state in February 2004. This low flux spectrum reveals for the first time the presence of an intermediate line region (ILR) in NGC 5548. The C IV emission line of this component has a FWHM of 700 km s^{-1} and is located at $\sim$ 1 pc from the nucleus. Crenshaw et al. (2009) model this gas with $U = 10^{-1.5}$ ($\log \xi = 0.1$), $n = 10^{13}$ m^{-3}, a column density of 3×10^{25} m^{-2} and a global covering factor of 0.06. The FWHM and location of the O VII f line allow for the possibility that the X-ray emission comes from the same ILR region or only slightly further out. The main difference is that the X-ray emitting region has a $\sim$ 100 times lower density and a $\sim$ 10 times higher ionization parameter. This would be consistent with the UV emission coming from dense clumps that are embedded in a low density hotter gas which produces the X-ray emission. The O VII f line centroid as observed by the LETGS agrees with the surrounding continuum to within 0.217″, which corresponds to 106 pc at the distance of NGC 5548 (Kaastra et al. 2003), giving a independent upper limit to the size of the NLR.

We therefore conclude that the NLR in NGC 5548 is compact in size, is in the form of clouds with a small covering factor or a narrow stream, has a cone-like geometry and is located between 1 and 15 pc from the central source, which is much smaller than the observed extended emission cones in Seyfert 2 galaxies (Kinkhabwala et al. 2002, Guainazzi et al. 2008). One reason for this compactness could be that in Seyfert 2 galaxies, we can not observe the high density, high emissivity NLR gas that we observe here, since the torus blocks our view. So we are only seeing the lower density, low emissivity gas in Seyfert 2 galaxies, which is visible due to the very low continuum flux. From optical studies it is clear that the high-ionization as well as the high critical density lines tend to be stronger in Seyfert 1's, see e.g. Bennert et al. (2006a). This is consistent with the compact size of the NLR we find in NGC 5548.

5.7 Conclusions

This is the first time that the long-term variability of the X-ray narrow line region has been studied in an AGN. NGC 5548 is the best studied AGN in the X-rays on a long time scale and has the best sampled *RXTE* lightcurve which last 11 years. With this very rich set of data and the large change in flux after 2002, we are able to put a constraint on the location and geometry of the X-ray NLR. For NGC 5548 we favor a NLR which is located between 1 and 15 pc from the central source, is compact in the form of clouds or a narrow stream and has the geometry of an ionization cone. This is consistent with the picture sketched in Seyfert 2 galaxies, although the distance from the central source is much smaller by almost two orders of magnitude. The geometry and location of the NLR in Seyfert 1 galaxies can be further refined by a long-term monitoring program with regular (every few months) high resolution spectral observations of sufficiently variable sources. It will be interesting to study a larger sample of NLR emission lines in Seyfert 1 galaxies, to see if they all are of similar size or if NGC 5548 is unique with its compact NLR.

Chapter 6

Ionized outflows in absorption and emission? Investigating the Seyfert 1 X-ray narrow line region with variability

R.G. Detmers

Submitted to Astronomy & Astrophysics, 2011

6.1 Abstract

We study the long time scale variability of the gas responsible for the X-ray narrow emission lines in a sample of Seyfert 1 galaxies, in order to constrain the location and geometry of the emitting gas. Using X-ray spectra taken with the *Chandra* LETGS and HETGS instruments and with XMM−*Newton* RGS we tried to constrain the time scales on which the narrow line emitting gas responds to variations of the continuum flux. We detect possible variability of the emission lines in two sources in our sample, namely Ark 564 and NGC 4051. However the systematic uncertainties involved in the continuum and absorption modeling, make any significant detection of variability difficult. Higher quality spectra where the emission features are accurately detected are needed in order to constrain any variability.

6.2 Introduction

Active Galactic Nuclei (AGN) have been studied for over 60 years now and can affect the evolution of their host galaxy by injecting energy into the ISM and IGM and by enriching their surroundings (Schawinski et al. 2007, Morganti et al. 2007, Feruglio et al. 2010, Dunn et al. 2010). However we still know very little about the geometry and physics of their inner regions, especially in the X-ray regime. This is because we can not directly resolve the direct surroundings of an AGN, but are forced to use other means, such as variability to probe these regions. Only in some nearby Seyfert 2 galaxies (e.g. NGC 1068), we can directly resolve the ionization cone (the cone-shaped ionized gas) and see part of the narrow-line region (NLR) (Kinkhabwala et al. 2002, Guainazzi & Bianchi 2007, Crenshaw et al. 2010). These ionization cones are thought to be present in almost all AGN, as the dusty torus is a natural means of funneling the ionizing radiation into a cone-like shape. The NLR is well studied in the optical and the UV, as it stretches out over many hundred's of pc in those bands (Fischer et al. 2010, Mazzalay et al. 2010). What remains elusive however, is the connection between the emission seen in these narrow lines (mostly in type 2 AGN) and the ionizing outflow seen in about half of the type 1 AGN. Is the NLR the outflow seen in emission? Or are they completely unrelated and have a different origin? There has been some work done already on this issue (Guainazzi & Bianchi 2007, Crenshaw et al. 2010), but it is very hard to conclusively prove the connection between the two, due to the fact that the exact geometry of either the NLR or the ionizing outflow is unknown. Different sources (type 1 and type 2 AGN) and different studies point in different directions (Behar et al. 2003, Crenshaw & Kraemer 2007, Smith et al. 2008). Especially for Type 1 AGN, the geometry and physics of the X-ray NLR are not well known, mainly because of the bright continuum of the AGN that swamps out most of the emission lines. There are a few sources which have well-studied cases of NLR lines in the X-ray regime (NGC 4151, Kraemer et al. 2008) (Ark 564 Smith et al. 2008) (NGC 4051, Nucita et al. 2010), but for most of the other sources no systematic investigation of the X-ray NLR has been done.

Recently (see Chapter 5) we have found that the O VII f emission line in NGC 5548 varied within 3 years and used that variability to constrain the geometry and location of the X-ray NLR gas to within 15 pc from the central source. This was the first time that variability of the X-ray NLR in a Seyfert 1 galaxy has been used to constrain the location and the geometry. In principle this method can be extended to other sources as well, especially as the archives of *XMM-Newton* and *Chandra* are filled with multiple observations of Type 1 AGN.

We therefore have selected a sample of type 1 AGN from the archives and performed a systematic spectral analysis (or re-analysis in the case of previously studied sources), specifically looking for emission lines and for any signs of variability in those lines between different observations.

The goal is to constrain the geometry and location of the X-ray NLR in these sources and, determine the possible connection between the emission lines and the ionized outflow seen in most of them. This paper focuses on the variability of the

Table 6.1: The sample of Seyfert 1 galaxies.

Source	Obs	Date	Instrument	Net Exposure (ks)
Ark 564	1	2000-06-17	HETGS	49
	2	2000-06-17	RGS	51
	3	2001-06-19	RGS	26
	4	2005-01-05	RGS	101
	5	2008-08-26	HETGS	85
	6	2008-09-04/06	HETGS	164
IRAS 13349+2438[1]	1	2000-06-20	RGS	65
	2	2004-02-22/24	HETGS	299
	3	2006-07-15/17	RGS	117
MCG-6-30-15	1	2000-04-05	HETGS	64
	2	2000-07-11	RGS	129
	3	2000-08-21	HETGS	65
	4	2001-08-01/05	RGS	348
	5	2004-05-19/27	HETGS	485
Mrk 279	1[1]	2002-05-07	RGS	33
	2[1]	2002-05-18	HETGS	114
	3	2003-05-10/20	LETGS	340
	4	2005-11-16/20	RGS	138
Mrk 290[1]	1	2003-06-29	HETGS	85
	2	2003-07-15/17	HETGS	165
	3	2006-04-30	RGS	98
Mrk 335	1	2000-12-25	RGS	37
	2	2006-01-05	RGS	133
	3	2007-07-10	RGS	23
Mrk 766[2]	1	2001-05-07	HETGS	90
	2	2005-05-23/31	RGS	489
Mrk 841	1	2000-12-25	RGS	37
	2	2006-01-05	RGS	133
	3	2007-07-10	RGS	23
NGC 3227	1[3]	1999-12-30	HETGS	49
	2[3]	2000-11-28	RGS	40
	3	2006-12-03	RGS	108

[1] No emission lines detected for these sources or observations.
[2] There were two RGS observations for Mrk 766, where there were problems concerning the data reduction, so those are missing from the sample.
[3] This observation contained too few counts to produce a useful spectrum.

Table 6.2: Continued from Table 6.1.

Source	Obs	Date	Instrument	Net Exposure (ks)
NGC 3516	1	2001-04-09/10	HETGS	110
	2	2001-04-11	RGS	130
	3	2001-11-09	RGS	130
	4	2001-11-11	HETGS	88
	5	2006-10-06/12	RGS	258
	6	2006-10-09/14	HETGS	150
NGC 3783	1	2000-01-20	HETGS	60
	2	2000-12-29	RGS	40
	3	2001-02-24/27	HETGS	335
	4	2001-03-10	HETGS	166
	5	2001-03-31	HETGS	167
	6	2001-06-26	HETGS	26
	7	2001-12-19/21	RGS	275
NGC 4051	1	2000-03-24	HETGS	80
	2	2001-05-17	RGS	122
	3	2001-12-31	LETGS	92
	4	2002-11-22	RGS	52
	5	2003-07-23	LETGS	95
NGC 4151	1	2000-03-05	HETGS	47
	2	2000-12-22/23	RGS	118
	3	2002-05-07/09	HETGS	244
	4	2002-07-02	LETGS	84
	5	2003-05-25/27	RGS	57
	6	2006-05-16	RGS	40
	7	2006-11-30	RGS	53
	8	2007-03-19	HETGS	51
	9	2007-07-21	HETGS	49

observed emission lines and to use it to constrain the geometry and distance of the emitting gas. A comparison with the absorption features will also be made in the cases in which an ionized outflow is present.

We discuss the sample used and the data reduction in Sect. 6.3. Sect. 6.4 describes the models used for fitting the spectra. We discuss our results in Sect. 6.5 and present our conclusions in Sect. 6.6.

Table 6.3: Source properties

Source	Redshift	N_H^a	M_{BH}^b	L_{ion}^c
Ark 564	0.0249	6.2	37[1]	44
IRAS 13349+2438	0.107	1.1	800[3]	14
MCG-6-30-15	0.0079	4.1	2.9[4]	5.0
Mrk 279	0.0306	1.8	35[2]	2.4
Mrk 290	0.0296	1.8	24[5]	6.9
Mrk 335	0.0254	4.0	14[2]	9.0
Mrk 766	0.0127	1.8	1.7[6]	1.3
Mrk 841	0.0364	2.5	126[7]	0.9
NGC 3227	0.0037	2.2	7.6[5]	0.04
NGC 3516	0.0088	3.5	32[5]	0.4
NGC 3783	0.0096	8.3	30[2]	1.3
NGC 4051	0.0022	1.4	1.7[5]	0.02
NGC 4151	0.0033	2.1	46[8]	0.6

[a] The neutral ISM column density towards the source in 10^{24} m^{-2}. Values are taken from Dickey & Lockman (1990).
[b] Black hole mass in units of 10^6 $M_\odot$. References:
1. Romano et al. (2004), 2. Peterson et al. (2004),
3. Brandt et al. (1997), 4. McHardy et al. (2005),
5. Denney et al. (2010), 6. Bentz et al. (2010),
7. Woo & Urry (2002), 8. Denney et al. (2009).
[c] Ionizing luminosity between $1 - 1000$ Ryd in 10^{37} W.

6.3 Sample selection and data reduction

The sample consists of well-studied Seyfert 1 galaxies, which have at least three high-resolution X-ray spectroscopic observations, with at least one of the observations 1 year apart from the others. This in order to probe the variability on a longer timescale, as in at least one case (NGC 5548, see Chapter 5) the variability was only detected on a timescale of years.

For the *Chandra* HETGS observations we used the public TGCat archive[1] to obtain the spectra. For the LETGS spectra we have used the procedure described in detail by Kaastra et al. (2002c). In summary, the data were reduced using the standard CXC pipeline up until the level 1.5 event files. For the steps leading to the final event file, level 2, we followed the independent procedure described in the aforementioned article. For the RGS observations we have obtained the data using the public archive and used the procedure described in Kaastra et al. (2011a) to stack the RGS 1 and 2 data and both spectral orders. This way the data files are strongly reduced in size (by a factor of 50), making the analysis for RGS spectra much more manageable. As the NLR emission is thought to come from regions further away than the BLR (the lines

[1] http://tgcat.mit.edu

Table 6.4: Narrow emission lines used in the NLR model.

Line	Wavelength (rest) (Å)
Ne x Ly α	12.132
Ne IX f	13.698
O VIII Ly α	18.969
O VII r	21.602
O VII i	21.802
O VII f	22.101
N VII Ly α	24.779
N VI r	28.779
N VI i	29.083
N VI f	29.535
C VI Ly α	33.736

are not resolved), and previous results show indeed no variations on short timescales (at least in the case of NGC 5548, see Detmers et al. 2009), we stack any observations of a source taken with the same instrument within 2 weeks of each other. We have specifically excluded NGC 5548 and Mrk 509 from this sample, as they are described in great detail in separate papers (Detmers et al. 2009, 2011). We focus mainly on the RGS observations, as the spectral range is larger than that of the MEG, so that the nitrogen and carbon lines are also included. The MEG data are used to check for signs of variability in the emission lines and also to set a tighter constraint on the lower limit to the distance, as the resolution is better than the RGS in the 10-25 Å wavelength range. The full sample of sources is listed in Table 6.1 and 6.2. The source properties are listed in Table 6.3. All errors are given for $\Delta\chi^2 = 1$. We use the SPEX 2.03.00[2] spectral fitting package to fit the spectra.

6.4 Spectral modeling

For all observations we used the following method to obtain the emission line parameters. We model the continuum with a spline so that we can accurately describe the complex continuum shape without making any assumptions about the origin and shape of the continuum. The spline has a logarithmic spacing of 0.05 between 5 and 40 Å for the RGS and LETGS spectra and between 1 and 26 Å for the HETGS spectra. This continuum spline is absorbed by three photo-ionized components (i.e. the ionized outflow) that are modeled using the *xabs* model of SPEX. The free parameters in this model for each component are the hydrogen column density N_H, the ionization parameter ξ, the r.m.s. velocity broadening σ and the outflow velocity v. We choose three *xabs* components, as this allows for a good description of the most

[2] see http://www.sron.nl/spex

prominent absorption features seen in Type 1 AGN. In the case that a source does not have an outflow or it is only seen in one component, the column densities of some or all of the *xabs* components are zero. The ionic column densities are related through the ionization parameter ξ. The photo-ionization balance used is based on the SED of NGC 5548 (Steenbrugge et al. 2005), which to a first approximation is suitable for all of the sources in the sample. The SED of NGC 5548 is a good representative SED for these Type 1 Seyferts, and the deviations for individual sources will be small. Also the cosmological redshift and Galactic absorption are taken into account. We model all the emission lines with delta functions, for which we only correct for the cosmological redshift and the neutral interstellar absorption. We model the neutral ISM absorption with a collisionally ionized component, called *hot* in SPEX. We fix the neutral hydrogen column density to the column density reported in Table 6.3 and fix the temperature to 5 eV so that there is no ionized gas present in the absorber.

For two sources, we used a more complex model, as the absorption is more complicated. These are MCG −6-30-15 and Mrk 766. They are well-known NLS1 galaxies and there has been extensive discussion in the literature over the interpretation of the feature at 17.5 Å (Branduardi-Raymont et al. 2001, Lee et al. 2001, Ballantyne et al. 2003, Sako et al. 2003). We here assume the interpretation of neutral (dusty) matter in the host galaxy, which produces the Fe L edges at 17.5 Å and to a lesser extent the O I edge at 23.5 Å. Additionally there is clear evidence for absorption by hot, local ($z = 0$) gas, which we also take into account. The model for MCG-6-30-15 is based on the model obtained by Holczer et al. (2010), with the addition of a neutral absorption component with only the Fe I column density and the outflow velocity v as free parameters (to mimic possible shifts in wavelength of the L2 and L3 edges of Fe I). We therefore model the absorption in MCG-6-30-15 with a *warm* model, which is a power-law distribution of *xabs* components. We first define a range of ionization parameters, between which we fit our model. In our case we fit the model between $\log \xi = -1.5$ and 3.5 (this is what was used in Holczer et al. 2010). We use a grid of 19 points in order to accurately describe the total absorption measure distribution (AMD). At every grid point a value f_i is determined, which is defined as $f_i = \frac{d N_H}{d \ln \xi}$. This way we obtain the distribution of N_H versus $\log \xi$. In addition we include one *xabs* component to model a highly ionized ($\log \xi \simeq 3.8$), fast ($v = 1800$ km s^{-1}) outflowing component (see Holczer et al. 2010). A collisionally ionized absorption component (*hot* in SPEX) is used to account for the hot, local absorption, responsible mainly for the O VII r absorption at 21.6 Å. Finally we include the neutral absorption component to take the Fe I edges into account. The same model is used for Mrk 766, although the absorption parameters (ξ, N_H, v, σ) are kept free to account for the different source properties.

The emission lines included are based on the lines detected in the NGC 1068 spectrum (Kinkhabwala et al. 2002), as this well-known Seyfert 2 emission-line spectrum is a clear example of all the possible emission lines which could be present in the spectrum of these type 1 AGN. This way we are certain to include the most important lines. The lines we have included in our model are listed in Table 6.4. We only include the strongest lines, as we are interested in detecting variability, which requires

accurate line fluxes. We fix the wavelengths of the lines to the rest wavelength of the AGN (i.e. no blue- or redshifts).

6.4.1 Results

The detected emission lines for all the observations of the sources in the sample are shown in Table 6.5 and 6.6. There are two sources out of 14 which tentatively show variable emission lines. These are Ark 564 and NGC 4051. The detected emission lines in these sources are shown in Table 6.7 and 6.8. In both cases the lines appear to show a consistent variation in that they all experience a simultaneous increase or decrease of their flux. For Ark 564, both the Ne IX and the O VIII lines appear to experience a drop in luminosity by a factor of 2 between observations 3 and 4. For NGC 4051, the major changes took place between observations 2 and 3. The emission line luminosities appear to have increased by a factor of 3 to 4. However as can also be seen in Fig. 6.1 − 6.6 the continuum and absorption lines are not well determined due to either a noisy spectrum or systematic uncertainties. This prevents us from claiming any significant variability in the emission lines.

6.4.2 Absorption and emission lines

6.5 Discussion

We have systematically analyzed a sample of bright, nearby Seyfert 1 galaxies, looking for variability in the emission lines. Out of 14 sources analyzed, two sources appear to show variability in some of the emission lines, while the others do not. However due to systematic uncertainties, it is not possible to claim any significant variability. Although all of the sources in the sample show variability in their continuum on different timescales, there are several effects which could be responsible for the observed lack of variability in the emission lines. The first is that the emission lines could be located at large distances form the central source. The light travel time increases, so that any variability of the continuum on shorter timescales will be washed out and have little effect. A clear example is NGC 5548, where only due to a large drop in the continuum for several years, the O VII f emission line dropped by a factor of 3 in luminosity. Any variability on shorter timescales (as was checked in Chapter 5), did not produce a significant drop in the line luminosity. The second is that sufficient exposure times, (i.e. high signal-to-noise) are needed in order to accurately measure the line luminosities. Smaller changes in line luminosity might occur (and do occur in some of the sources in the sample), but due to the large error bars, the variability is not significant ($1\,\sigma$ only). NGC 4151 is a special case, as it is not a typical Seyfert 1 galaxy. It shows a rich emission line spectrum, but there is also a ionized absorber present. There have been multiple publications (Kraemer et al. 2005, Crenshaw & Kraemer 2007) on this source and both the absorber and the emission lines show a high level of complexity. In some observations, some of the

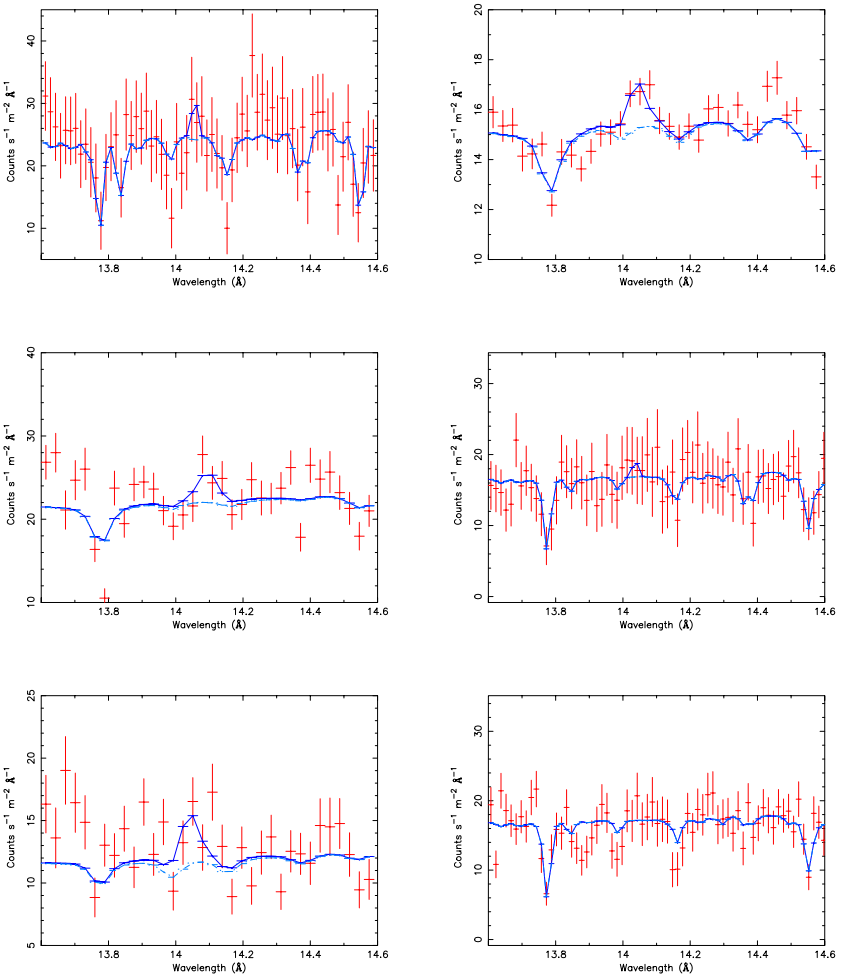

Figure 6.1: The Ne IX f emission line for the different observations of Ark 564. Left, from top to bottom, observation 1 to 3. Right, from top to bottom, observation 4 to 6. The light-blue dashed-dotted line shows the model without emission lines, while the dark blue line shows the model with the emission lines.

lines in Table 6.5, seem to vary. However there is no consistent trend visible between the different emission lines. If the lines respond to a change in the continuum flux, then we would expect multiple lines to respond, especially lines with a similar ionization parameter. Also our assumption of no red-or blueshifted emission lines is most likely an oversimplification for this source. The main problem with almost all

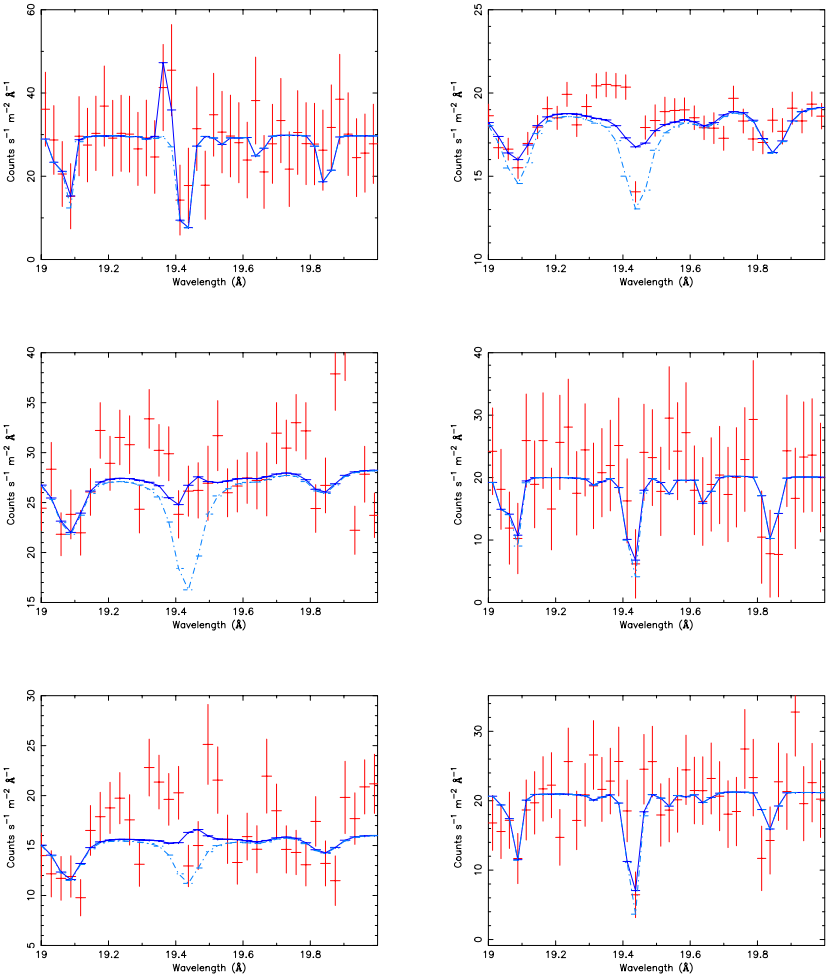

Figure 6.2: The same as Fig. 6.1, but for the O VIII emission line.

of these spectra is that the exposures are too short to obtain a high enough quality spectrum to accurately measure the emission lines along with the continuum and absorption lines. There are a few sources (NGC 3783 for example) which do have a good enough spectrum, but they do not show any variability in their emission lines.

So far there has been only one source where a significant variability of the emission lines was observed. That is NGC 5548 (Chapter 5), where due to a long-term drop in the continuum flux, changes in both the absorbing and emitting gas were detected. For NGC 5548 there have been 7 high resolution observations over a period of 8 years,

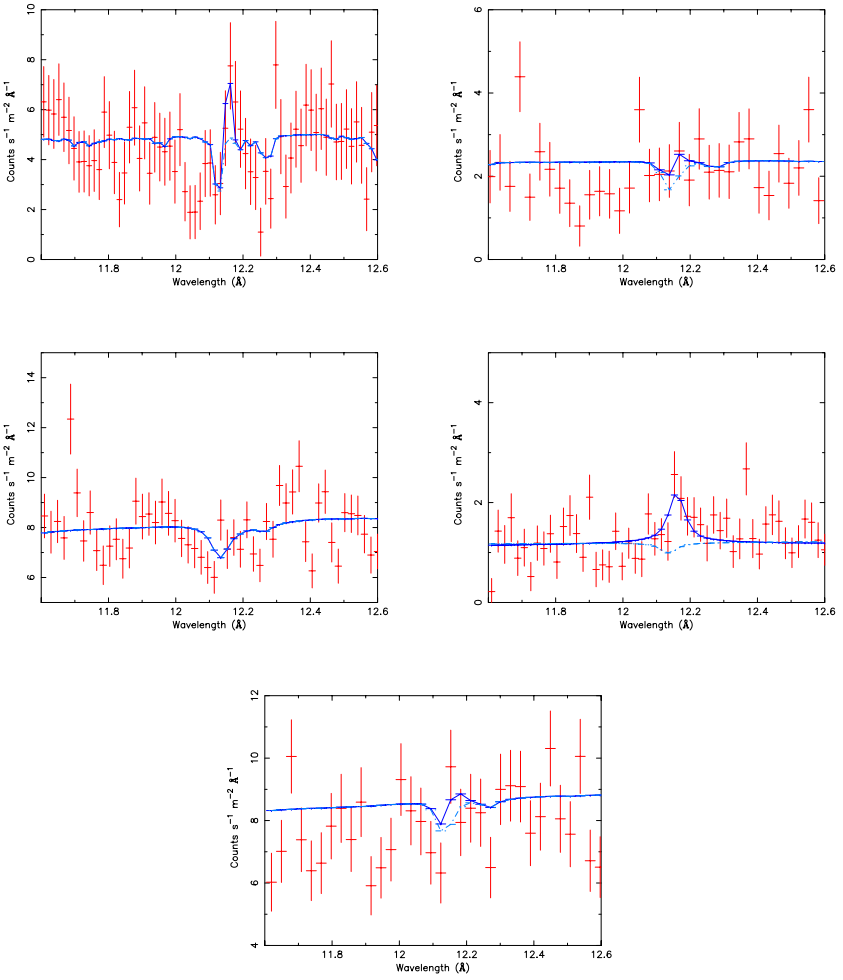

Figure 6.3: As Fig. 6.2, but for NGC 4051 and for the Ne x emission line. Left, from top to bottom, observation 1 and 2. Right, from top to bottom, observation 3 and 4. In the bottom center observation 5.

each with a high quality spectrum. Thanks to this long-term monitoring, drastic spectral changes on longer timescales were detected, which would have escaped detection with randomly timed observations on shorter timescales (i.e. months). The fact that the changes in NGC 5548 were so drastic, made the detection of significant variability in the emission lines possible. Most likely there are also smaller changes in the emission lines on shorter timescales (such as the tentative changes seen in NGC

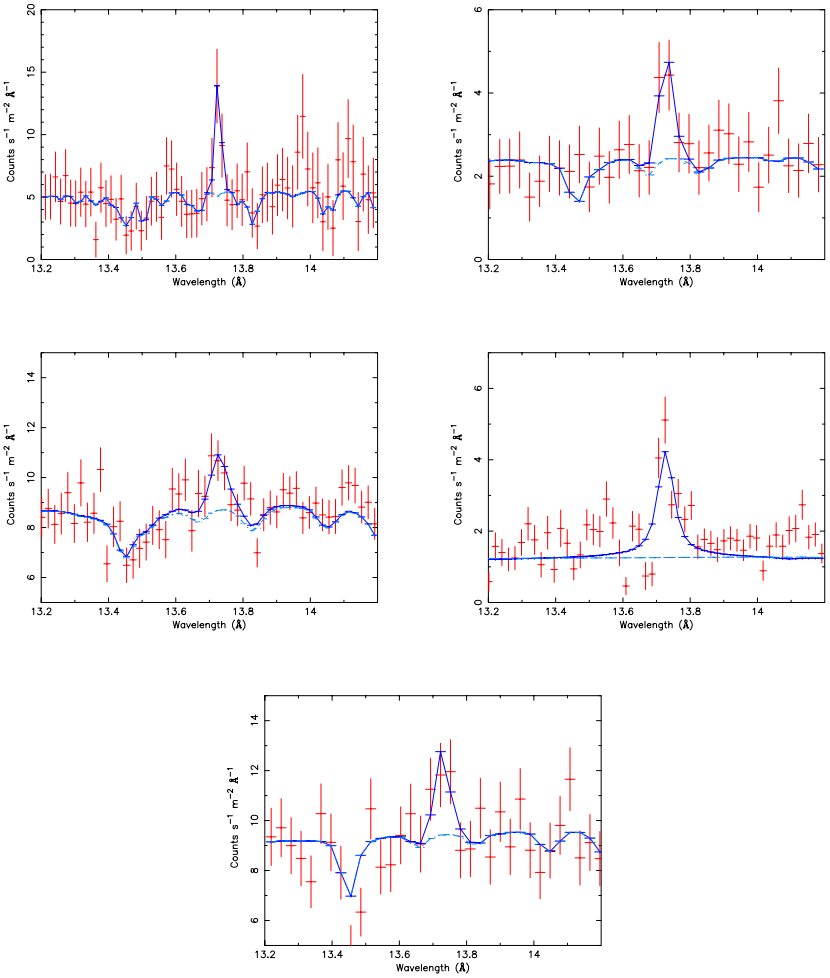

Figure 6.4: As Fig. 6.3, but for the Ne IX f emission line.

4051 and Ark 564), but those are not significant either due to the statistical or the systematic uncertainties. Better quality spectra are needed in order to obtain accurate line fluxes and constrain the timescale of variability of the X-ray NLR.

It is still possible to obtain information on the location and density of the X-ray NLR. This requires the use of photo-ionization models, such as those used for the Broad Line Region in UV and Optical spectra (the so-called LOC model Baldwin et al. 1995). These has been applied successfully in both the analysis of X-ray broad emission lines (Costantini et al. 2007a) and in the analysis of optical spectra of Ark

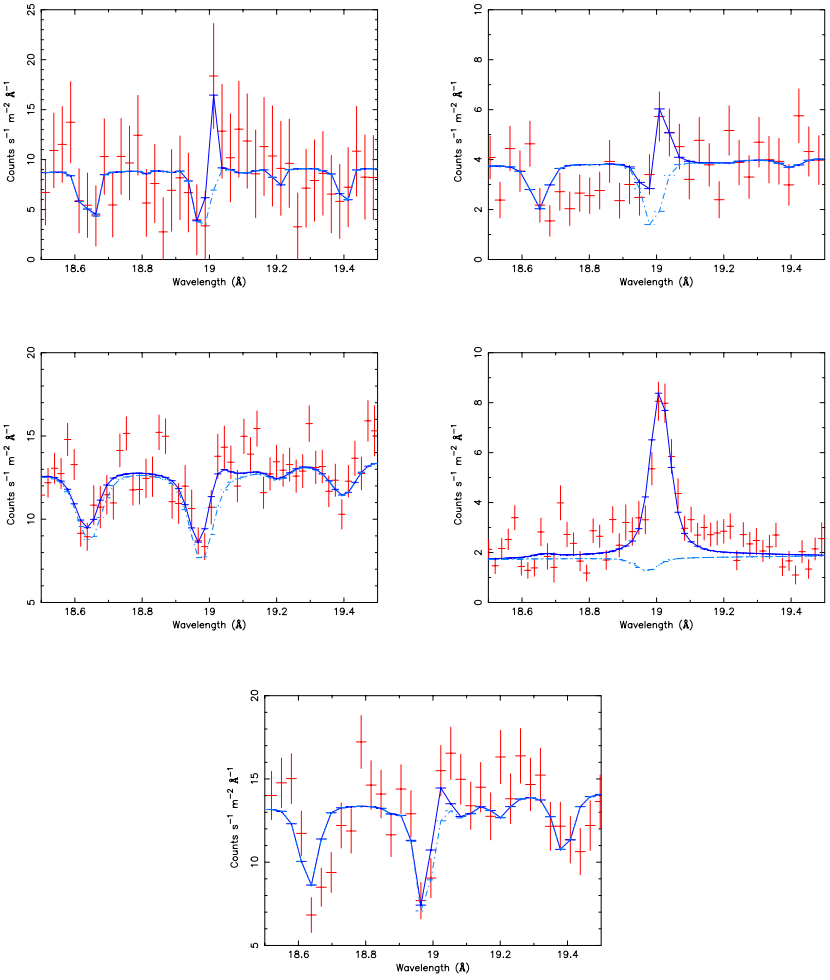

Figure 6.5: As Fig. 6.3, but for the O VIII emission line.

564, where they were used to constrain the location of the forbidden high ionization emission lines (FHIL, Mullaney et al. 2009). For these models, all the spectra of one source can be stacked (at least if there is no variability in the lines), which leads to accurate line fluxes. These photo-ionization models have been applied to only a few sources (Ark 564, NGC 4151), so a lot of information can still be gained from this kind of work. More so if also the UV, optical and IR emission lines are included and the comparison with the absorption models can be made.

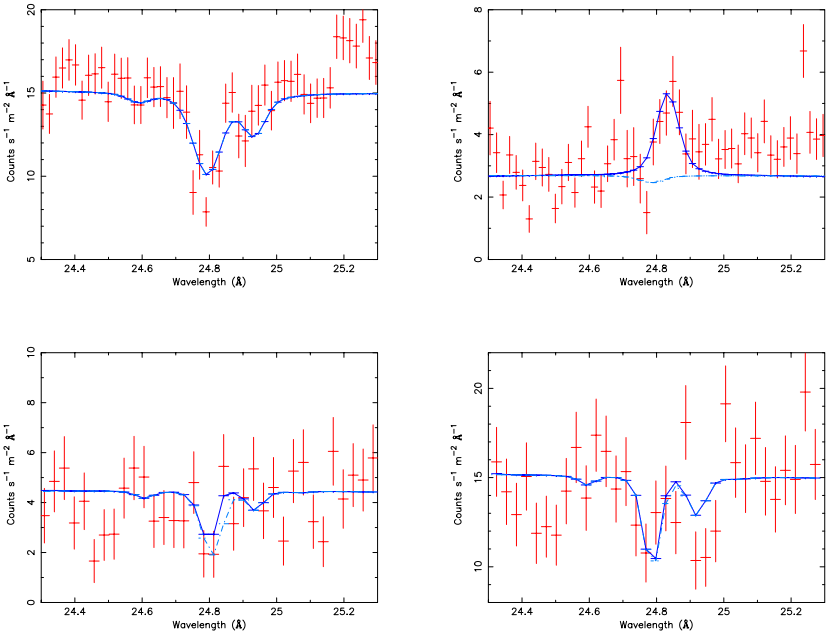

Figure 6.6: As Fig. 6.3, but for the N VII emission line.

6.6 Conclusions

This is the first time that a systematic study of the X-ray NLR in Seyfert 1 galaxies has been performed. Using multiple observations for each source, we have detected possible variability in the emission lines of two AGN, Ark 564 and NGC 4051. However systematic uncertainties in the continuum and the absorption lines prevent us from claiming any significant variability in the emission lines. Better quality spectra are needed in order to probe the variability on the timescales investigated here. Photoionization modeling is the best method at the moment to obtain information on the location and ionization structure of the X-ray NLR, as in most cases spectra form different epochs can be stacked to increase the accuracy of line fluxes. Combining the information contained in the X-ray, UV, optical and IR high-resolution spectra of type 1 AGN is the key towards a better understanding of the X-ray NLR and its connection to the ionized outflow.

Table 6.5: The sample of Seyfert 1 galaxies, along with the fluxes of the emission lines for each observation[1]. IRAS 13349+2438 and Mrk 290 are missing from this list, as no emission lines were detected in those sources. The fluxes are corrected for Galactic and intrinsic absorption. The numbers in parenthesis are the $1-\sigma$ errors on the line fluxes.

Source	Obs	Ne X	Ne IX	O VIII Ly α	O VII r	O VII i	O VII f	N VII Ly α	N VI r	N VI i	N VI f	C VI Ly α
Ark	1	≤ 0.06	≤ 0.34	0.97 (0.45)	≤ 1.26	≤ 1.13	≤ 1.31	–	–	–	–	–
564	2	≤ 0.15	0.51 (0.19)	1.41 (0.33)	≤ 1.03	≤ 0.28	1.09 (0.70)	1.24 (0.38)	≤ 0.98	1.29 (0.62)	≤ 1.1	≤ 1.0
	3	≤ 0.29	0.53 (0.16)	1.52 (0.17)	1.24 (0.40)	≤ 0.31	≤ 0.87	1.15 (0.45)	1.13 (0.47)	≤ 0.79	1.0 (0.6)	1.5 (0.8)
	4	≤ 0.04	0.24 (0.05)	0.72 (0.07)	0.38 (0.16)	≤ 1.12	0.52 (0.18)	0.87 (0.11)	0.69 (0.18)	0.52 (0.19)	≤ 0.5	1.0 (0.3)
	5	≤ 0.09	≤ 0.22	0.57 (0.32)	≤ 0.91	≤ 1.29	≤ 1.37	–	–	–	–	–
	6	≤ 0.04	≤ 0.14	0.65 (0.09)	≤ 0.67	≤ 1.07	≤ 0.48	–	–	–	–	–
MCG	1	≤ 0.02	≤ 0.05	≤ 0.04	≤ 0.15	≤ 0.39	≤ 0.18	–	–	–	–	–
6-30	2	≤ 0.01	0.12 (0.03)	0.08 (0.06)	≤ 0.16	≤ 0.27	0.27 (0.13)	0.22 (0.15)	0.19 (0.10)	≤ 0.15	≤ 0.1	≤ 0.2
-15	3	≤ 0.05	0.09 (0.04)	≤ 0.05	≤ 0.28	≤ 0.25	0.68 (0.40)	–	–	–	–	–
	4	≤ 0.01	0.16 (0.03)	≤ 0.06	≤ 0.02	0.38 (0.24)	0.50 (0.10)	≤ 0.02	0.25 (0.07)	0.09 (0.05)	≤ 0.1	≤ 0.1
	5	≤ 0.01	0.06 (0.03)	≤ 0.02	≤ 0.03	0.36 (0.13)	≤ 0.31	–	–	–	–	–
Mrk	3	≤ 0.07	0.06 ± 0.03	≤ 0.06	≤ 0.10	≤ 0.12	0.10 (0.05)	≤ 0.06	≤ 0.05	≤ 0.17	≤ 0.1	≤ 0.2
279	4	≤ 0.09	≤ 0.08	≤ 0.09	≤ 0.07	≤ 0.12	≤ 0.13	≤ 0.16	≤ 0.09	≤ 0.14	≤ 0.1	≤ 0.2
Mrk	1	≤ 0.10	0.11 (0.06)	0.24 (0.10)	0.74 (0.15)	≤ 0.26	≤ 0.26	≤ 0.05	0.30 (0.15)	≤ 0.08	≤ 0.2	≤ 0.2
335	2	≤ 0.05	0.10 (0.04)	0.25 (0.06)	0.58 (0.11)	0.25 (0.08)	0.31 (0.14)	0.09 (0.07)	0.22 (0.11)	≤ 0.12	≤ 0.2	0.3 (0.2)
	3	≤ 0.08	≤ 0.07	0.31 (0.08)	0.41 (0.14)	0.38 (0.10)	0.36 (0.09)	0.18 (0.05)	0.16 (0.12)	≤ 0.05	≤ 0.1	0.3 (0.1)
Mrk	1	≤ 0.02	≤ 0.14	≤ 0.19	0.24 (0.18)	≤ 0.20	≤ 0.63	–	–	–	–	–
766	2	≤ 0.01	0.09 (0.01)	0.06 (0.01)	≤ 0.05	≤ 0.01	0.29 (0.03)	≤ 0.01	0.04 (0.02)	0.06 (0.03)	0.2 (0.1)	0.2 (0.1)
Mrk	1	≤ 0.05	0.13 (0.04)	≤ 0.14	0.33 (0.13)	≤ 0.23	≤ 0.29	0.16 (0.08)	0.24 (0.12)	0.23 (0.12)	0.2 (0.1)	≤ 0.3
841	2	≤ 0.10	0.13 (0.03)	0.09 (0.05)	0.27 (0.09)	0.38 (0.08)	≤ 0.29	0.24 (0.08)	≤ 0.14	≤ 0.24	0.2 (0.1)	0.3 (0.2)
	3	0.08 (0.04)	0.09 (0.03)	0.09 (0.05)	0.29 (0.09)	0.15 (0.08)	0.18 (0.08)	≤ 0.12	0.18 (0.15)	0.09 (0.07)	≤ 0.1	≤ 0.1
NGC	3	≤ 0.01	≤ 0.03	≤ 0.09	≤ 0.07	≤ 0.14	0.19 (0.08)	≤ 0.03	0.14 (0.06)	≤ 0.05	≤ 0.1	≤ 0.1
3227												

[1] The fluxes are given in photons m^{-2} s^{-1}.

[2] A – indicates a bad pixel was present at the location of the emission line in the RGS, or that the emission lines were outside the range of the HETGS.

Table 6.6: Continued from Table 6.5.

Source	Obs	Ne x	Ne ix	O viii Ly α	O vii r	O vii i	O vii f	N vii Ly α	N vi r	N vi i	N vi f	C vi Ly α
NGC	1	0.05 (0.03)	0.04 (0.03)	0.20 (0.10)	$\leq$ 0.12	$\leq$ 0.23	0.56 (0.19)	–	–	–	–	–
3516	2	$\leq$ 0.08	0.06 (0.03)	0.11 (0.04)	–	0.11 (0.06)	0.26 (0.09)	$\leq$ 0.06	$\leq$ 0.12	$\leq$ 0.16	0.3 (0.1)	$\leq$ 0.3
	3	0.03 (0.02)	0.10 (0.01)	0.13 (0.02)	0.15 (0.05)	0.10 (0.03)	0.38 (0.04)	0.10 (0.02)	0.15 (0.05)	0.09 (0.04)	0.3 (0.1)	0.2 (0.1)
	4	$\leq$ 0.04	0.05 (0.03)	$\leq$ 0.09	$\leq$ 0.15	$\leq$ 0.18	0.30 (0.16)	–	–	–	–	–
	5	$\leq$ 0.04	$\leq$ 0.14	0.15 (0.03)	–	0.19 (0.07)	0.45 (0.07)	$\leq$ 0.07	$\leq$ 0.09	0.26 (0.09)	0.3 (0.1)	$\leq$ 0.2
	6	$\leq$ 0.02	0.07 (0.03)	$\leq$ 0.10	$\leq$ 0.05	$\leq$ 0.19	0.58 (0.27)	–	–	–	–	–
NGC	1	0.14 (0.07)	0.14 (0.04)	0.72 (0.24)	0.68 (0.34)	0.42 (0.29)	1.49 (0.50)	–	–	–	–	–
3783	2	$\leq$ 0.06	$\leq$ 0.10	0.48 (0.10)	–	$\leq$ 0.14	0.48 (0.16)	$\leq$ 0.19	$\leq$ 0.14	0.40 (0.14)	$\leq$ 0.4	0.8 (0.3)
	3	0.06 (0.03)	0.07 (0.02)	0.43 (0.09)	0.68 (0.14)	0.28 (0.10)	1.10 (0.18)	–	–	–	–	–
	4	$\leq$ 0.11	0.11 (0.03)	0.53 (0.14)	0.31 (0.17)	$\leq$ 0.14	0.73 (0.25)	–	–	–	–	–
	5	0.10 (0.05)	0.15 (0.04)	0.36 (0.16)	0.52 (0.20)	$\leq$ 0.09	0.61(0.29)	–	–	–	–	–
	6	$\leq$ 0.07	0.13 (0.03)	0.47 (0.12)	0.51 (0.18)	$\leq$ 0.09	0.75 (0.26)	–	–	–	–	–
	7	0.09 (0.03)	0.18 (0.03)	0.47 (0.05)	0.69 (0.12)	0.27 (0.08)	0.75 (0.10)	0.19 (0.04)	0.14 (0.10)	$\leq$ 0.20	0.3 (0.1)	0.8 (0.2)
NGC	1	0.06 (0.02)	0.23 (0.05)	0.36 (0.14)	$\leq$ 0.22	0.27 (0.16)	1.50 (0.25)	–	–	–	–	–
4051	2	$\leq$ 0.03	0.18 (0.04)	0.22 (0.05)	0.13 (0.07)	0.49 (0.12)	1.82 (0.18)	$\leq$ 0.06	$\leq$ 0.07	0.29 (0.10)	0.5 (0.2)	0.9 (0.2)
	3	$\leq$ 0.08	0.15 (0.04)	0.25 (0.05)	0.07 (0.05)	$\leq$ 0.29	1.44 (0.20)	0.08 (0.06)	$\leq$ 0.09	0.18 (0.09)	0.2 (0.1)	0.4 (0.1)
	4	0.11 (0.03)	0.30 (0.03)	0.75 (0.06)	0.11 (0.04)	0.58 (0.09)	1.84 (0.14)	0.32 (0.05)	$\leq$ 0.08	0.15 (0.05)	0.5 (0.1)	0.6 (0.1)
	5	$\leq$ 0.14	0.20 (0.07)	0.39 (0.08)	0.39 (0.19)	$\leq$ 0.16	0.83 (0.16)	0.16 (0.11)	$\leq$ 0.15	0.27 (0.14)	0.4 (0.2)	0.3 (0.1)
NGC	1	0.20 (0.03)	0.44 (0.07)	1.32 (0.19)	0.86 (0.22)	0.34 (0.17)	4.38 (0.59)	–	–	–	–	–
4151	2	0.28 (0.02)	0.54 (0.03)	1.84 (0.04)	1.56 (0.06)	0.70 (0.03)	5.50 (0.20)	1.04 (0.05)	0.85 (0.06)	0.32 (0.05)	1.6 (0.1)	2.8 (0.1)
	3	0.24 (0.02)	0.42 (0.04)	1.60 (0.12)	1.28 (0.15)	0.90 (0.13)	5.27 (0.34)	–	–	–	–	–
	4	0.22 (0.03)	0.46 (0.06)	1.42 (0.10)	0.93 (0.14)	1.03 (0.12)	4.14 (0.39)	0.62 (0.13)	0.41 (0.12)	0.08 (0.06)	0.8 (0.1)	3.1 (0.3)
	5	0.29 (0.04)	0.38 (0.04)	1.84 (0.07)	1.83 (0.11)	1.22 (0.11)	–	0.98 (0.08)	0.85 (0.09)	0.48 (0.07)	1.5 (0.1)	2.9 (0.2)
	6	0.28 (0.04)	0.45 (0.05)	1.65 (0.07)	1.56 (0.13)	0.79 (0.11)	2.90 (0.33)	0.98 (0.07)	0.81 (0.09)	0.13 (0.08)	1.4 (0.1)	3.0 (0.2)
	7	0.25 (0.04)	0.49 (0.08)	0.48 (0.03)	1.62 (0.11)	0.94 (0.09)	3.62 (0.20)	0.64 (0.07)	0.80 (0.09)	0.35 (0.06)	1.1 (0.1)	2.3 (0.2)
	8	0.21 (0.04)	0.28 (0.06)	1.61 (0.27)	0.87 (0.29)	0.71 (0.34)	2.18 (0.48)	–	–	–	–	–
	9	0.21 (0.04)	0.32 (0.06)	1.15 (0.24)	0.75 (0.27)	1.10 (0.38)	4.75 (0.76)	–	–	–	–	–

Table 6.7: The emission line luminosities of the variable lines for each spectrum of Ark 564. Luminosities are given in 10^{33} W.

Line	1	2	3	4	5	6
Ne IX f	≤ 7.5	9.5 ± 3.6	11.7 ± 3.5	4.7 ± 0.8	≤ 0.5	≤ 0.25
O VIII Ly α	19.8 ± 7.7	20.3 ± 3.5	18.0 ± 3.9	9.2 ± 1.2	6.4 ± 2.9	7.6 ± 4.1

Table 6.8: Same as Table 6.7, but for NGC 4051. Luminosities are given in 10^{31} W.

Line	1	2	3	4	5
Ne X	1.4 ± 0.6	≤ 0.4	≤ 1.0	2.0 ± 0.5	≤ 0.5
Ne IX f	2.9 ± 0.4	3.0 ± 0.6	3.2 ± 0.8	5.0 ± 0.4	2.4 ± 0.8
O VIII Ly α	4.8 ± 2.1	2.8 ± 0.7	4.3 ± 0.9	9.0 ± 0.6	2.0 ± 0.4
N VII Ly α	–	≤ 0.6	1.2 ± 0.9	3.0 ± 0.4	0.6 ± 0.4

Hoofdstuk 7

Nederlandse Samenvatting

Actieve sterrenstelsels (AGN hierna) zijn sterrenstelsels waarvan de kern zeer veel licht produceert. Meer licht dan verklaard kan worden door de straling van de aanwezige sterren. Dit extra licht wordt geproduceerd door de accretie van gas en stof op een superzwaar zwart gat in het midden van het sterrenstelsel. Bij deze accretie komt er ook veel UV en Röntgen straling vrij. Deze straling wordt geabsorbeerd door een gedeelte van het gas in de omgeving van het superzware zwarte gat, waardoor dit gas kan worden weggeblazen met snelheden van vele honderden km s^{-1}. Enorme hoeveelheden gas en stof kunnen zo ver het sterrenstelsel in worden geblazen. Deze uitstromingen kunnen zorgen voor verrijking van het gas in het sterrenstelsel en kunnen ook een groot effect hebben op de evolutie van het sterrenstelsel. Ook kan door het wegblazen van het gas de toevoer van materie naar het zwarte gat verminderen of zelfs helemaal stoppen. Dit zou betekenen dat de evolutie van het sterrenstelsel en de groei van het zwarte gat in het centrum verbonden zijn. Deze verbinding tussen het sterrenstelsel en het zwarte gat wordt ook wel 'feedback' of terugkoppeling genoemd. Het grootste probleem is dat we nog er weinig weten van de feedback. We weten niet zeker of de uitstromingen inderdaad sterk genoeg zijn om een effect te hebben op de evolutie van het sterrenstelsel. En hoe doen ze dat dan precies ? Bijna elk sterrenstelsel (ook het onze) heeft een superzwaar zwart gat in het centrum (maar ze zijn niet allemaal actief). Het vraagstuk van de feedback is dan ook een van de belangrijkste in de moderne sterrenkunde. Door deze AGN en de uitstromingen in detail te bestuderen, kunnen we meer te weten komen over dit feedback proces en uiteindelijk de belangrijkste vragen beantwoorden. Maar alle nieuwe kennis wordt in kleine stappen vergaard en in dit proefschrift probeer ik eerst belangrijke vragen over de uitstroming zelf te beantwoorden. Hoe ontstaat deze precies ? Wat is de structuur van de uitstroming en waar bevind deze zich ? Ik

geef eerst een korte introductie over AGN en de uitstromingen en tot slot bespreek ik het onderzoek dat gepresenteerd wordt in dit proefschrift.

7.0.1 Actieve sterrenstelsels

Een AGN is opgebouwd uit verschillende componenten (zie Fig. 7.1. In het midden bevind zich het superzware zwarte gat met een accretieschijf van gas erom heen. Boven de accretieschijf bevind zich een atmosfeer van hete (tientallen miljoenen graden Celsius) elektronen. Dit wordt de corona genoemd. Iets verderop in de accretieschijf worden brede emissielijnen geproduceerd. Deze lijnen zijn breed door de Doppler verbreding vanwege de rotatiesnelheid van het gas dat zich in een baan om het zwarte gat beweegt. Dit geheel wordt omringd door een grote torus van stof. De uitstroming kan op verschillende plekken ontstaan, in de accretieschijf, het brede lijnen gebied, of op het oppervlak van de torus. Op grotere afstanden bevind zich het gas dat de nauwe emissielijnen produceert. Doordat dit gas zich verder van het zwarte gat bevind is de rotatiesnelheid lager en dus is de Doppler verbreding kleiner.

AGN worden onderverdeeld in twee verschillende soorten, Type 1 en Type 2. Het verschil tussen beide soorten zit hem in onder welke hoek we naar de AGN kijken. Als we onder een hoek kijken waarbij we de torus niet raken, dan zien we alle componenten, inclusief de uitstroming en spreken we van een Type 1 AGN. Als we daarentegen onder een hoek kijken waarbij we de torus raken, dan blokkeert deze het zicht op het binnengebied van de AGN (de accretieschijf en het brede lijnen gebied). We zien de directie straling van de accretieschijf niet en we zien alleen de emissielijnen van het nauwe lijnen gebied verderop. Dit wordt een Type 2 AGN genoemd

7.0.2 De uitstroming

De uitstromingen die in Type 1 zijn gezien in hoge resolutie UV en Röntgen spectra worden nu al meer dan 10 jaar bestudeerd. Daardoor zijn we al heel wat te weten gekomen over de eigenschappen van de uitstroming in verschillende AGN:

- De uitstroomsnelheden variren van ongeveer 50 tot 2000 km s^{-1}.
- Het gas bestaat uit een grote verscheidenheid van ionisatietoestanden, van laag geoniseerd gas (zoals bijvoorbeeld O III en C IV) tot aan zeer hoog geoniseerd gas (zoals Fe XXIV).

Wat nog niet duidelijk is, is hoe en waar deze uitstromingen ontstaan. En wat de structuur precies is; is het een continue stroom van gas of is het meer een chaotisch geheel met grote locale dichtheidsverschillen ? Om deze vragen te beantwoorden maken we gebruik van hoge-resolutie UV en Röntgen spectroscopie om de uitstromingen in detail te bestuderen. In het Röntgen gebied maken we hierbij gebruik van twee satellieten, *Chandra* en *XMM-Newton*. Beide satellieten hebben Röntgen tralies aan boord, de Low Energy Transmission Grating Spectrometer (LETGS) en High

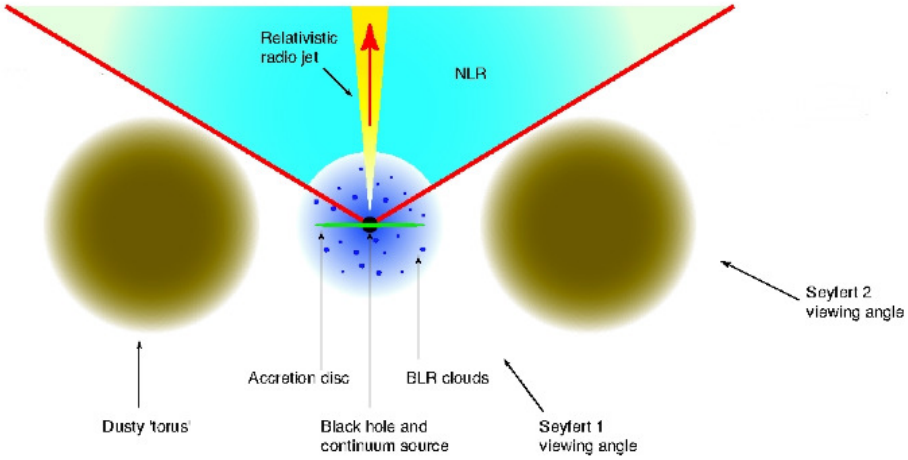

Figuur 7.1: De verschillende componenten van een AGN. Het zwarte gat met daaromheen de accretieschijf bevindt zich in het midden. In sommige gevallen is er een relativistische jet aanwezig die loodrecht op de accretieschijf staat. Het brede emissielijnen gebied (BLR) en nauwe emissielijnen gebied (NLR) zijn ook aangegeven. De torus van stof (dusty torus) die zorgt voor de verschillen tussen Type 1 en 2 AGN is ook te zien.

Energy Transmission Grating Spectrometer (HETGS) voor *Chandra*, en de Reflection Grating Spectrometer (RGS) aan boord van *XMM-Newton*. Door individuele spectra van een AGN te bestuderen, kunnen we de belangrijkste eigenschappen bepalen, zoals uitstroomsnelheid, kolomdichtheden van verschillende ionen en de ionisatieverdeling. Om de locatie ten opzichte van het zwarte gat te bepalen moeten we echter gebruik maken van een belangrijke eigenschap van AGN, namelijk hun variabiliteit.

7.0.3 Variabiliteit

Zoals al eerder aangegeven zijn alle AGN variabel. De lichtkracht varieert op een tijdschaal van uren tot maanden en kan in sommige gevallen fluctuaties vertonen van een factor 10 of groter. Door deze variaties in lichtkracht verandert ook de hoeveelheid ioniserende straling dat het gas van de uitstroming ontvangt. Dit betekend dat het gas meer of minder geoniseerd wordt door de variaties in de lichtkracht. Het gas verandert echter niet meteen van ionisatietoestand, maar reageert met een vertraging. De tijdschaal waarop dit gebeurt wordt de recombinatietijdschaal genoemd en hangt af van de dichtheid van het gas. Hoe groter de dichtheid, des te korter de tijdschaal is. Dit komt doordat de kans op interactie tussen de ionen en de elektronen dan groter is. Als we dus meerdere waarnemingen van dezelfde bron

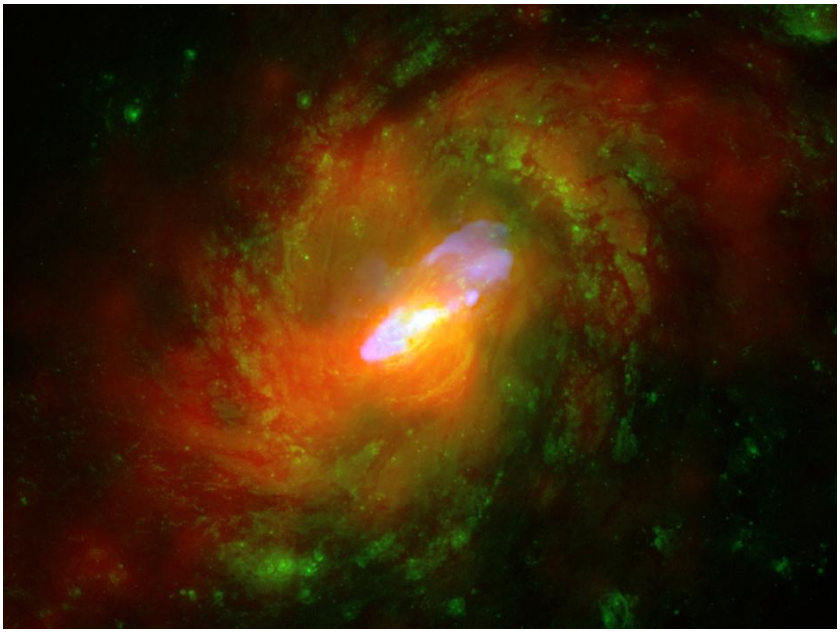

Figuur 7.2: De uitstroming in NGC 1068. De verschillende kleuren laten de verschillende golflengtes zien. Röntgen data van *Chandra* zijn te zien in rood. Zichtbaar licht van de *Hubble Space Telescope* in groen en radio data van de *Very Large Array* (VLA) is te zien in blauw. De uitstroming kan in dit geval meerdere zonsmassa's aan gas verplaatsen tot ver in de uiteindes van het sterrenstelsel. (Image Credit: X-ray (NASA/CXC/ MIT/C.Canizares, D.Evans et al), Optical (NASA/STScI), Radio (NSF/ NRAO/VLA))

hebben, kunnen we kijken of de lichtkracht veranderd is in een latere waarneming en of het gas van de uitstroming hierop heeft gereageerd. Als dit het geval is kunnen we de tijdschaal bepalen waarop het gas heeft gerecombineerd (naar een lagere ionisatietoestand gaan) en dus kunnen we ook de dichtheid van het gas bepalen. In de meeste gevallen kunnen we niet de exacte tijdschaal bepalen en blijft het bij een bovenlimiet. De ionisatietoestand van het gas hangt samen met lichtkracht van de AGN, de dichtheid van het gas en de afstand van het gas tot het zwarte gat. De lichtkracht en de ionisatietoestand kunnen vrij eenvoudig uit de waarnemingen gehaald worden. Met een limiet op de dichtheid hebben we ook een limiet op de afstand van het gas. Op deze manier kunnen we voor een gering aantal heldere AGN de locatie van de uitstroming bepalen.

7.0.4 Dit proefschrift

Hoofdstuk 2

Mrk 509 is een van de helderste AGN aan de hemel. Het doel van de waarnemingen die in dit hoofdstuk beschreven staan is om verschillen te detecteren in de eigenschappen van de uitstroming (voornamelijk de ionisatie toestand). Doordat Mrk 509 slechts kleine verschillen vertoont in lichtkracht, is het bijna onmogelijk om die met behulp van de hoge-resolutie spectrometer RGS te detecteren. De EPIC-pn CCD camera (een ander instrument aan boord van *XMM-Newton*) heeft daarentegen wel een groot effectief oppervlak en zou die kleine verschillen in principe dus kunnen detecteren, maar de spectrale resolutie is te laag om de individuele absorptielijnen te onderscheiden. Door de data simultaan met beide instrumenten (RGS en EPIC-pn) te analyseren kunnen we in principe gebruik maken van de beste eigenschappen van beide instrumenten en zo toch de kleine verschillen in de ionisatietoestand van de uitstroming zien. Hiervoor moest echter eerst een model voor de calibratieverschillen van beide instrumenten worden gemaakt. Met een goed model voor de calibratieverschillen konden we inderdaad kleine verschillen detecteren in de ionisatietoestand van de uitstroming en zo de locatie bepalen tot binnen 1.5 lichtjaar van het centrale zwarte gat.

Hoofdstuk 3

In de herfst van 2009 is een van de grootste waarneemcampagnes van een AGN uitgevoerd voor Mrk 509. Met R⊙ontgen, UV en optische satellieten is Mrk 509 40 dagen lang gevolgd. Het doel was om zo mogelijke veranderingen in de uitstroming op een korte tijdschaal te kunnen volgen in meerdere energiebanden. Het onderzoek in dit hoofdstuk houd zich bezig met het totale RGS spectrum van 600000 seconden. Door de lange waarneemtijd is de kwaliteit van het spectrum uitzonderlijk en konden de eigenschappen van de uitstroming tot in detail worden bestudeerd. De analyse van het spectrum liet voor het eerst zien dat de uitstroming uit vijf discrete ionisatie componenten bestaat. Dit is een belangrijk resultaat wat in verder onderzoek gebruikt kan worden om modellen van de oorsprong van de uitstroming te testen. Een ander belangrijk resultaat is dat er een indicatie is dat er een verband is tussen de ionisatietoestand en de uitstroomsnelheid van het gas. Hoe meer geoniseerd het gas is, des te hoger de uitstroomsnelheid. In het algemeen geldt dat het gas met de grootste uitstroomsnelheid zich dichter bij het zwarte gat bevind, dus dit verband geeft al meteen een schets hoe de verschillende ionisatiecomponenten zich onderling in afstand verhouden. De resultaten van dit onderzoek staan aan de basis van meerdere vervolg artikelen van deze waarneemcampagne.

Hoofdstuk 4

NGC 5548 is een andere heldere AGN die al lang grondig bestudeerd is met meerdere satellieten. Dit onderzoek gaat in op de verschillen van de uitstroming tussen twee

waarnemingen (een in 2002 en een in 2005). Geheel onverwachts liet de waarneming van 2005 een grote afname in helderheid zien (een factor vijf). Door een vrij eenvoudig model toe te passen voor het bepalen van de kolomdichtheden van de uitstroming, konden we laten zien dat er een zeer duidelijke afname was in de ionisatietoestand van het gas in 2005. Hoog geoniseerde ionen zoals O VIII waren afgenomen in hoeveelheid, terwijl de laag geoniseerde ionen zoals O V juist waren toegenomen. Hierdoor konden we de tijdschaal waarop het gas veranderde beperken tot minder dan 3 jaar, wat uiteindelijk in een afstandsbepaling leidde van maximaal 21 lichtjaar voor de uitstroming in NGC 5548.

Hoofdstuk 5

Tijdens de 2005 waarneming van NGC 5548, zagen we ook een opmerkelijk verschil in de sterkte van twee emissielijnen (de verboden lijnen van O VII en Ne IX). Dit was voor het eerste dat een verandering in de sterkte van deze emissielijnen was waargenomen in een AGN. Ook hierbij gold dat we de tijdschaal konden afschatten tot maximaal 3 jaar. Door hiervan gebruik te maken en door het volume te bepalen van het gas wat de lijnen uitzend konden we voor het eerst de geometrie en locatie van het emissiegas in NGC 5548 bepalen. Het emissiegas in NGC 5548 heeft de vorm van een kegel en bevind zich op een afstand tussen 3 en 45 lichtjaar van het zwarte gat. Een vergelijking van de eigenschappen van de uitstroming en dit emissiegas liet zien dat het mogelijk om hetzelfde gas gaat. De uitstroming zelf kan dus verantwoordelijk zijn voor de emissielijnen die we zien in NGC 5548.

Hoofdstuk 6

Na de opmerkelijke detectie van de variatie in de emissielijnen in NGC 5548 was de volgende stap om te kijken of dit ook in andere bronnen mogelijk het geval was. Door de archieven van *Chandra* en *XMM-Newton* door te spitten op geschikte bronnen, bleven er 11 andere bronnen over die geschikt waren voor deze studie. Een systematische analyse van alle waarnemingen van deze AGN liet zien dat er twee bronnen waren waarbij er mogelijke variaties in de emissielijnen gedetecteerd waren. Het probleem is echter dat doordat de individuele spectra van relatief lage kwaliteit waren er grote systematische onzekerheden zijn op het bepalen van de sterkte van de lijnen. Hierdoor kon niet worden vastgesteld of dat deze lijnen ook daadwerkelijk varieerden in sterkte.

Hoofdstuk 8

Acknowledgements

Dit boekje is het resultaat van het werk dat ik de afgelopen 5 jaar gedaan heb. De keuze om een promotieonderzoek in de Sterrenkunde te doen 5 jaar geleden is een van de beste keuzes van mijn leven geweest. Het onderzoek doen, de vele conferenties en landen die ik bezocht heb en de vele mensen en vrienden die ik heb ontmoet maakten het allemaal meer dan waard. Uiteraard ging het niet altijd even vlot, en het afronden van dit proefschrift bleek lastiger te zijn dan gedacht, maar de positieve ervaringen die ik heb opgedaan de afgelopen jaren maken dat allemaal meer dan goed. Ik ben er ook achter gekomen dat onderzoek doen het leukste en beste werk is voor mij. Helaas ben ik er ook achter gekomen dat het op dit moment erg lastig is om een goede baan in de Sterrenkunde te krijgen. Gelukkig ben ik door de vele discussies met mijn EPS collega's de afgelopen jaren erachter gekomen dat klimaatonderzoek ook heel erg interessant en uitdagend is. Ik zal dan ook de Sterrenkunde verlaten en gebruik maken van de data van satellieten die de andere kant opkijken om bosbranden te gaan bestuderen en modelleren. Het voltooien van een PhD is niet eenvoudig en ik ben dan ook dankbaar voor alle hulp, discussies, leuke gesprekken, en ook ontspanning die ik heb gehad van alle mensen.

Jelle, bedankt voor je begeleiding, advies, steun en de vele nuttige en leuke discussies over het AGN en Röntgen spectroscopie. Ook bedankt voor de mogelijkheden die je me gaf om mijn werk op conferenties te presenteren en mijn eigen ideeën uit te werken. Frank, bedankt voor je steun, interesse en de vele gesprekken over de geschiedenis van de Sterrenkunde, politiek en onderwijs. Ook voor je oprechte commentaar wanneer dat nodig was. Elisa, thanks for helping me get started on my research in the first year of my PhD. You've been a great help in explaining and showing a lot of the practical things about doing high−resolution X-ray spectroscopy on AGN and I really appreciate that. I hope you didn't suffer too much with my music preferences when you were my officemate. Frits, I'm really glad that your

one year sabbatical at SRON was during my thesis. Thanks for the many interesting discussions and talks, those were greatly motivating me during my second year and it helped my PhD a lot. It's a shame we did not get to finish our project on dust in AGN. I would also like to thank all the members of the (very successful) Mrk 509 consortium and especially Jerry, Nahum, and Ehud for all the interesting and useful discussions, help and advice during our collaboration. It was very good to be part of the consortium.

Jacobo, Eva, Manuel, Ton, Ciro, Yan, Jelle (de Plaa), Peter, Daniel, Cor, Hans, Lucien, Wim, Jan-Willem, Jean, Mariano, Norbert, Laurens, Peter (den Hartog), Remco, Esther, Marlies, thanks for being great colleagues and for making SRON such a nice place to work the last 5 years. I enjoyed my time here and I will miss it. Also thanks to all the other colleagues at SRON who helped make it a great place to work. Leo, Jiri, Rodrigo and the others of the Torun summer school, thanks for making the summer school such a wonderful experience! I had no idea that it would be so great and motivating and I really enjoyed the nice evenings going out in the old centre of Torun.

Thijs, Arno, Ralph, Sander, Sietse, Pieter, Bart, Rien, Jeroen, bedankt voor de vele, vele spelletjesavonden. Wie had gedacht dat het noemen van gaming als een van mijn hobbies in het SRON nieuws tot hiertoe zou leiden. De vele ontspannende en gezellige avonden en soms hele zaterdagen waren broodnodig en dat zullen ze ook blijven ! Ralph ook bedankt voor de vele leuke gesprekken en discussies die we hebben gehad over ons werk, vooral tijden de Cospar in Montreal. Die hebben mijn interesse om klimaatonderzoek te gaan doen aangewakkerd en dat werpt nu zijn vruchten af. Bedankt ook voor de gelegenheid om voor 3 maanden te werken aan de calibratie voor TROPOMI, wat mij veel inzicht heeft gegeven in de details van calibratie van instrumenten in het algemeen. Thijs, ook bedankt voor de vele discussies over gaming en voor het regelen van mijn eerste eigen appartement. Ik heb er twee jaar lang met plezier gewoond ! Remco, bedankt voor de twee mooie reizen naar Zwitserland en Schotland ! De West Highland Way wandelen was een hele mooie en plezierige ervaring met jou, vooral de Ben Nevis met regen en harde wind was een interessante beklimming ... Eva, Gio, Sara, Fede, Ila, Mauro, Paola, Gabrielle, Claudia, Claudio, thanks for making my trip to Italy such a nice experience. It was a great holiday ! Eva, Gio and Sara, thanks for your friendship over the last couple of years.

Merijn, David, Peter, Eric en Mark, bedankt voor de vele mooie bordspeldagen die we hebben gehad. Vooral ook bedankt voor de vele D&D sessies en avonturen die we hebben beleefd, vooral voor de 5+ jaar Age of Worms campaign die we tot een mooi einde hebben weten te brengen. Ik speel nu al meer dan de helft van mijn leven D&D en in mijn ogen is het zeer bijzonder dat we zolang al deze hobby samen delen. Wie weet komt er nog een keer een nieuwe campaign van. Bedankt voor jullie vriendschap ! David ook bedankt voor de vele lunches / koffiepauzes die we hadden op de Uithof, we hadden het beide erg druk maar mooi dat we zo toch op de hoogte konden blijven van elkaars doen. Gelukkig wonen jullie nu een stuk dichter bij, zodat we elkaar wat vaker kunnen zien.

Rik, Ben, Nieske, Jeroen, Annelies, Anke, Anna, bedankt voor de vele gezellige woensdagavonden van D&D en bordspellen. Het was altijd erg leuk en gaf me de ontspanning die ik nodig had. Floris, bedankt voor je gezelschap tijdens de fantastische reis naar het hoge noorden van Zweden. De Kungsleden lopen was geweldig en het is een hele mooie vakantie geworden. Bedankt ook voor je vriendschap en de vele interessante en leuke gesprekken die we hadden tijdens mijn tijd op de Warande 37 ! Jorrit, bedankt voor je gezelschap tijdens de geweldige reis naar London en het fantastische Springsteen concert dat we daar gezien hebben. Bedankt ook voor je vriendschap de afgelopen jaren en de gezellige etentjes die we nog steeds hebben.

Theo en Karin, bedankt voor het onderhouden van de Stripotheek iedere week. Het was erg fijn om in Wijchen te komen en dan te kunnen ontspannen met een nieuwe lading stripboeken, ook al heb ik de meeste series nu wel zo'n 10 keer gelezen. Theo, ook bedankt voor de vele fijne gesprekken op de vrijdagavond. Jan, bedankt voor de leuke gesprekken die we hebben gehad op feestjes en verjaardagen en voor de interesse die je toonde in mijn werk.

Marieke, ik zal het kort houden, jij bent de beste zus die ik me kan wensen. Ook al snap je niet altijd wat je broer precies deed, je toonde altijd interesse en was er altijd voor je me en dat waardeer ik enorm. Pap en mam, jullie onvoorwaardelijke steun met alles heeft me zeer veel geholpen en betekend veel voor me. Ik hoefde maar iets te vragen en jullie stonden klaar voor me als dat nodig was. Ik waardeer dit alles enorm en ik beschouw mezelf erg gelukkig dankzij jullie. Pap, ook bedankt voor de vele, vele concerten die we samen bezochten. Die hebben ons nog meer verbonden denk ik en ik vind het fantastisch dat ik een vader heb waarmee ik dat kan doen. Als Springsteen, Tom Petty, BAP of Lohues weer in de buurt komen, gaan we zeker ! We hebben tenslotte allemaal baat bij muziek !

Oliwia, moja misiu, I don't really know where to start to thank you. Let's start by saying thanks for your help and patience in the last weeks of writing this thing. You've made an amazing cover illustration ! Thanks for the great holidays we've had together, it's great to know that we share the love for the mountains (whether in winter or summer). I'm sure Alaska will also be amazing ! You and me have something wonderful and very special together and I hope that we can keep on sharing that for a long time. Kocham cie !

"But the stars are burnin' bright like some mystery uncovered"
"I'll keep movin' through the dark with you in my heart "

Bruce Springsteen

Chapter 9

Curriculum Vitae

Ik ben geboren op 14 Juni 1981 te Arnhem in Nederland. Na in 1985 naar Wijchen verhuisd te zijn, zat ik daar op de basisschool de Paschalisschool. In 1993 ging ik naar het Dominicuscollege te Nijmegen om daar mijn Atheneum opleiding te volgen. In 1999 haalde ik mijn eindexamen VWO en in September van dat jaar ben ik met de opleiding Natuur−en Sterrenkunde begonnen in Utrecht. Binnen het eerste studiejaar haalde ik mijn propedeuse en in 2004 begon ik aan mijn afstudeeronderzoek aan Gamma-Ray Burst progenitors onder begeleiding van Prof. dr. Norbert Langer. Dit onderzoek leidde uiteindelijk ook tot een publicatie in het tijdschrift Astronomy & Astrophysics. Mijn doctoraalexamen in de Natuur−en Sterrenkunde behaalde ik op 25 April 2006. In September 2006 begon ik aan mijn promotieonderzoek over hogeresolutie Rntgen spectroscopie van actieve sterrenstelsels onder begeleiding van Dr. Jelle Kaastra en Prof. dr. Frank Verbunt bij SRON Netherlands Institute for Space Research. Tijdens mijn promotie heb ik vele conferenties en workshops bezocht waar ik mijn resultaten kon presenteren en heb ik ook twee waarnemingsvoorstellen voor de XMM-Newton telescoop ingediend die beide gehonoreerd zijn met waarnemingstijd. Ook ben ik nauw betrokken geweest bij een grote, zeer succesvolle internationale waarnemingscampagne. In September 2010 liep mijn officile contract bij SRON af en heb ik nog een half jaar extra gewerkt aan mijn promotieonderzoek. Na een korte uitstap bij de EPS divisie van 3 maanden voor een project over TROPOMI calibratie, zal ik op 15 November 2011 de Sterrenkunde vaarwel zeggen en beginnen aan een postdoc baan bij de VU in Amsterdam over biomass burning.

Chapter 10

Publications

Refereed publications

1. K. C. Steenbrugge, J. S. Kaastra, R. G. Detmers, J. Ebrero, G. Ponti, E. Costantini, G. A. Kriss, M. Mehdipour, C. Pinto, G. Branduardi-Raymont, E. Behar, N. Arav, M. Cappi, S. Bianchi, P.-O. Petrucci, E. M. Ratti and T. Holczer, 2011, "*Multiwavelength campaign on Mrk 509 VII. Relative abundances of the warm absorber*", A&A 534, A42

2. G. A. Kriss, N. Arav, J. S. Kaastra, J. Ebrero, C. Pinto, B. Borguet, D. Edmonds, E. Costantini, K. C. Steenbrugge, R. G. Detmers, E. Behar, S. Bianchi, A. J. Blustin, G. Branduardi-Raymont, M. Cappi, M. Mehdipour, P. Petrucci and G. Ponti, 2011, "*Multiwavelength campaign on Mrk 509 VI. HST/COS observations of the far-ultraviolet spectrum*", A&A 534, A41

3. J. Ebrero, G. A. Kriss, J. S. Kaastra, R. G. Detmers, K. C. Steenbrugge, E. Costantini, N. Arav, S. Bianchi, M. Cappi, G. Branduardi-Raymont, M. Mehdipour, P. O. Petrucci, C. Pinto and G. Ponti. 2011, "*Multiwavelength campaign on Mrk 509 V. Chandra-LETGS observation of the ionized absorber*", A&A 534, A40

4. M. Mehdipour, G. Branduardi-Raymont, J. S. Kaastra, , P. O. Petrucci, G. A. Kriss, , G. Ponti, A. J. Blustin, S. Paltani, M. Cappi, R. G. Detmers, and K. C. Steenbrugge, 2011, "*Multiwavelength campaign on Mrk 509 IV. Optical-UV-X-ray variability and the nature of the soft X-ray excess*", A&A 534, A39

5. R. G. Detmers, J. S. Kaastra, K. C. Steenbrugge, J. Ebrero, G. A. Kriss, N. Arav, E. Behar, E. Costantini, G. Branduardi-Raymont, M. Mehdipour, S. Bianchi, M. Cappi, P. Petrucci, G. Ponti, C. Pinto, E. M. Ratti and T. Holczer, 2011, "*Multiwavelength campaign on Mrk 509 III. The 600 ks RGS spectrum: unravelling the inner region of an AGN*", A&A 534, A38 (Chapter 3)

6. J. S. Kaastra, C. P. de Vries, K. C. Steenbrugge, R. G. Detmers, J. Ebrero, E. Behar, S. Bianchi, E. Costantini, G. A. Kriss, M. Mehdipour, S. Paltani, P.-O. Petrucci, C. Pinto and G. Ponti, 2011, "*Multiwavelength campaign on Mrk 509 II. Analysis of high-quality Reflection Grating Spectrometer spectra*", A&A 534, A37

7. J. S. Kaastra, P.-O. Petrucci, M. Cappi, N. Arav, E. Behar, S. Bianchi, J. Bloom, A. J. Blustin, G. Branduardi-Raymont, E. Costantini, M. Dadina, R. G. Detmers, J. Ebrero, P. G. Jonker, C. Klein, G. A. Kriss, P. Lubi?ski, J. Malzac, M. Mehdipour, S. Paltani, C. Pinto, G. Ponti, E. M. Ratti, R. A. N. Smith, K. C. Steenbrugge, and C. P. de Vries, 2011, "*Multiwavelength campaign on Mrk 509 I. Variability and spectral energy distribution*", A&A 534, A36

8. J.-U. Ness, J. P. Osborne, A. Dobrotka, K. L. Page, J. J. Drake, C. Pinto, R. G. Detmers, G. Schwarz, M. F. Bode, A. P. Beardmore, S. Starrfield, M. Hernanz, G. Sala, J. Krautter and C. E. Woodward, 2011, "*XMM-Newton X-ray and Ultraviolet observations of the fast nova V2491 Cyg during the supersoft source phase*", ApJ 733 70

9. J. Ebrero, E. Costantini, J. S. Kaastra, R. G. Detmers, N. Arav, G. A. Kriss, K. T. Korista and K. C. Steenbrugge, 2010, "*XMM-Newton RGS observation of the warm absorber in Mrk 279*", A&A 520, A36

10. R. G. Detmers, J. S. Kaastra, E. Costantini, F. Verbunt, M. Cappi and C. de Vries, 2010, "*The outflow in Mrk 509. A method to calibrate XMM-Newton EPIC-pn and RGS*", A&A 516, A61 (Chapter 2)

11. R.G. Detmers, J.S. Kaastra and I.M. McHardy, 2009, "*X-ray narrow line region variability as a geometry probe. The case of NGC 5548*", A&A 504, 409 (Chapter 5)

12. R. G. Detmers, J. S. Kaastra, E. Costantini, I. M. McHardy and F. Verbunt, 2008, "*The warm absorber in NGC 5548. The lean years*", A&A 488, 67-72 (Chapter 4)

13. R. G. Detmers, N. Langer, Ph. Podsiadlowski and R. G. Izzard, 2008, "*Gamma-ray bursts from tidally spun-up Wolf-Rayet stars?*", A&A 484, 831-839

14. O. Toledano, E. Moreno, G. Koenigsberger, R. G. Detmers and N. Langer, 2006, "*Tides in asynchronous binary systems*", A&A 461, 1057-1063

Conference proceedings

1. R.G. Detmers and J.S. Kaastra, 2009, "*AGN Outflow Feedback: Constraints from Variability*", AIP conference proceedings, Volume 1201, pp. 60-63

Submitted

1. R.G. Detmers, 2011, "*Ionized outflows in absorption and emission? Investigating the Seyfert 1 X-ray narrow line region with variability*", submitted to A&A (Chapter 6)

Bibliography

Andrillat, Y. 1968, AJ, 73, 862 (cited on page 5)

Antonucci, R. 1993, ARA&A, 31, 473 (cited on pages 7 and 87)

Arav, N., Gabel, J. R., Korista, K. T., et al. 2007, ApJ, 658, 829 (cited on page 49)

Arav, N., Korista, K. T., Barlow, T. A., & Begelman. 1995, Nature, 376, 576 (cited on page 13)

Arav, N., Korista, K. T., & de Kool, M. 2002, ApJ, 566, 699 (cited on page 12)

Balbus, S. A. & Hawley, J. F. 1991, ApJ, 376, 214 (cited on page 13)

Baldwin, J., Ferland, G., Korista, K., & Verner, D. 1995, ApJ, 455, L119 (cited on pages 5 and 116)

Ballantyne, D. R., Weingartner, J. C., & Murray, N. 2003, A&A, 409, 503 (cited on page 111)

Behar, E. 2009, ApJ, 703, 1346 (cited on pages 16, 49, 69, and 73)

Behar, E., Rasmussen, A. P., Blustin, A. J., et al. 2003, ApJ, 598, 232 (cited on pages 7, 28, 49, 68, 92, and 106)

Bennert, N., Jungwiert, B., Komossa, S., Haas, M., & Chini, R. 2006a, A&A, 459, 55 (cited on pages 102 and 103)

Bennert, N., Jungwiert, B., Komossa, S., Haas, M., & Chini, R. 2006b, A&A, 456, 953 (cited on page 7)

Bentz, M. C., Denney, K. D., Cackett, E. M., et al. 2006, ApJ, 651, 775 (cited on page 6)

Bentz, M. C., Denney, K. D., Cackett, E. M., et al. 2007, ApJ, 662, 205 (cited on pages 78, 86, 88, and 99)

Bentz, M. C., Walsh, J. L., Barth, A. J., et al. 2010, ApJ, 716, 993 (cited on page 109)

Bianchi, S., Guainazzi, M., & Chiaberge, M. 2006, A&A, 448, 499 (cited on pages 7, 92, 97, and 102)

Bianchi, S., Miniutti, G., Fabian, A. C., & Iwasawa, K. 2005, MNRAS, 360, 380 (cited on page 92)

Blandford, R. D. & McKee, C. F. 1982, ApJ, 255, 419 (cited on page 13)

Blustin, A. J. & Fabian, A. C. 2009, MNRAS, 399, L169 (cited on page 6)

Blustin, A. J., Page, M. J., Fuerst, S. V., Branduardi-Raymont, G., & Ashton, C. E. 2005, A&A, 431, 111 (cited on pages 12, 13, 15, 49, and 78)

Bottorff, M. C., Korista, K. T., & Shlosman, I. 2000, ApJ, 537, 134 (cited on pages 40, 85, and 98)

Bower, R. 2009, in American Institute of Physics Conference Series, Vol. 1201, American Institute of Physics Conference Series, ed. S. Heinz & E. Wilcots, 1–8 (cited on page 48)

Brandt, W. N., Mathur, S., Reynolds, C. S., & Elvis, M. 1997, MNRAS, 292, 407 (cited on page 109)

Branduardi-Raymont, G., Sako, M., Kahn, S. M., et al. 2001, A&A, 365, L140 (cited on page 111)

Brinkman, A. C., Gunsing, C. J. T., Kaastra, J. S., et al. 2000, ApJ, 530, L111 (cited on page 79)

Brotherton, M. S., Green, R. F., Kriss, G. A., et al. 2002, ApJ, 565, 800 (cited on page 101)

Brown, G. V., Beiersdorfer, P., Liedahl, D. A., Widmann, K., & Kahn, S. M. 1998, ApJ, 502, 1015 (cited on page 148)

Brown, G. V., Beiersdorfer, P., Liedahl, D. A., et al. 2002, ApJS, 140, 589 (cited on page 148)

Burtscher, L., Jaffe, W., Raban, D., et al. 2009, ApJ, 705, L53 (cited on page 9)

Cappi, M., Tombesi, F., Bianchi, S., et al. 2009, A&A, 504, 401 (cited on pages 29, 42, and 50)

Cardelli, J. A., Clayton, G. C., & Mathis, J. S. 1989, ApJ, 345, 245 (cited on page 30)

Cash, W. 1979, ApJ, 228, 939 (cited on page 79)

Chakravorty, S., Kembhavi, A. K., Elvis, M., & Ferland, G. 2009, MNRAS, 393, 83 (cited on pages 14 and 32)

Charbonneau, P. 1995, ApJS, 101, 309 (cited on page 61)

Clavel, J., Reichert, G. A., Alloin, D., et al. 1991, ApJ, 366, 64 (cited on page 5)

Collins, J. A., Shull, J. M., & Giroux, M. L. 2009, ApJ, 705, 962 (cited on page 7)

Costantini, E. 2010, Space Sci. Rev., 157, 265 (cited on pages 13 and 18)

Costantini, E., Kaastra, J. S., Arav, N., et al. 2007a, A&A, 461, 121 (cited on pages 6, 7, 12, 15, 84, and 116)

Costantini, E., Kaastra, J. S., Arav, N., et al. 2007b, A&A, 461, 121 (cited on pages 49, 54, 55, 57, 68, and 69)

Crenshaw, D. M. & Kraemer, S. B. 1999, ApJ, 521, 572 (cited on page 78)

Crenshaw, D. M. & Kraemer, S. B. 2007, in Astronomical Society of the Pacific Conference Series, Vol. 373, The Central Engine of Active Galactic Nuclei, ed. L. C. Ho & J.-W. Wang, 319 (cited on pages 106 and 112)

Crenshaw, D. M., Kraemer, S. B., Boggess, A., et al. 1999, ApJ, 516, 750 (cited on page 78)

Crenshaw, D. M., Kraemer, S. B., Gabel, J. R., et al. 2003, ApJ, 594, 116 (cited on pages 3, 78, 80, and 84)

Crenshaw, D. M., Kraemer, S. B., Schmitt, H. R., et al. 2010, AJ, 139, 871 (cited on page 106)

Crenshaw, D. M., Kraemer, S. B., Schmitt, H. R., et al. 2009, ArXiv e-prints (cited on page 103)

Das, V., Crenshaw, D. M., Hutchings, J. B., et al. 2005, AJ, 130, 945 (cited on page 7)

den Herder, J. W., Brinkman, A. C., Kahn, S. M., et al. 2001, A&A, 365, L7 (cited on page 28)

Denney, K. D., Peterson, B. M., Pogge, R. W., et al. 2010, ApJ, 721, 715 (cited on pages 49 and 109)

Denney, K. D., Watson, L. C., Peterson, B. M., et al. 2009, ApJ, 702, 1353 (cited on pages 6 and 109)

Detmers, R., Kaastra, J., Steenbrugge, K., Ebrero, J., & Kriss, G. 2011, accepted for publication in A&A (cited on page 110)

Detmers, R. G., Kaastra, J. S., Costantini, E., et al. 2010, A&A, 516, A61 (cited on page 72)

Detmers, R. G., Kaastra, J. S., & McHardy, I. M. 2009, A&A, 504, 409 (cited on page 110)

Di Matteo, T., Springel, V., & Hernquist, L. 2005, Nature, 433, 604 (cited on pages 1, 28, and 48)

Dickey, J. M. & Lockman, F. J. 1990, ARA&A, 28, 215 (cited on page 109)

Dunn, J. P., Bautista, M., Arav, N., et al. 2010, ApJ, 709, 611 (cited on pages 48 and 106)

Ebrero, J., Kriss, G. A., Kaastra, J. S., et al. 2011, A&A, 534, A40 (cited on page 72)

Elvis, M. 2006, Mem. Soc. Astron. Italiana, 77, 573 (cited on page 48)

Engstrom, L. & Litzen, U. 1995, Journal of Physics B Atomic Molecular Physics, 28, 2565 (cited on pages 36 and 148)

Fabian, A. C. 2010, in IAU Symposium, Vol. 267, IAU Symposium, 341–349 (cited on page 48)

Fabian, A. C., Sanders, J. S., Allen, S. W., et al. 2003, MNRAS, 344, L43 (cited on page 48)

Fabian, A. C., Sanders, J. S., Taylor, G. B., et al. 2006, MNRAS, 366, 417 (cited on page 21)

Fabian, A. C., Vasudevan, R. V., & Gandhi, P. 2008, MNRAS, 385, L43 (cited on page 13)

Ferland, G. J., Korista, K. T., Verner, D. A., et al. 1998, PASP, 110, 761 (cited on pages 32 and 51)

Ferrarese, L. & Merritt, D. 2000, ApJ, 539, L9 (cited on page 48)

Ferrarese, L., Pogge, R. W., Peterson, B. M., et al. 2001, ApJ, 555, L79 (cited on page 21)

Feruglio, C., Maiolino, R., Piconcelli, E., et al. 2010, A&A, 518, L155 (cited on page 106)

Fischer, T. C., Crenshaw, D. M., Kraemer, S. B., Schmitt, H. R., & Trippe, M. L. 2010, AJ, 140, 577 (cited on page 106)

Fisher, K. B., Huchra, J. P., Strauss, M. A., et al. 1995, ApJS, 100, 69 (cited on page 29)

Fukumura, K., Kazanas, D., Contopoulos, I., & Behar, E. 2010, ApJ, 715, 636 (cited on pages 13 and 73)

Gabel, J. R., Crenshaw, D. M., Kraemer, S. B., et al. 2003, ApJ, 583, 178 (cited on pages 12, 28, and 49)

Garcia, J. D. & Mack, J. E. 1965, Journal of the Optical Society of America (1917-1983), 55, 654 (cited on page 36)

Gaskell, C. M., Klimek, E. S., & Nazarova, L. S. 2007, ArXiv e-prints, submitted to ApJ (cited on page 49)

Gebhardt, K., Bender, R., Bower, G., et al. 2000, ApJ, 539, L13 (cited on pages 21 and 48)

Gelbord, J. M., Mullaney, J. R., & Ward, M. J. 2009, MNRAS, 397, 172 (cited on page 9)

Ghez, A. M., Salim, S., Hornstein, S. D., et al. 2005, ApJ, 620, 744 (cited on page 2)

Goad, M. R. & Page, K. L. 2006, in Proceedings of the The X-ray Universe 2005 (ESA SP-604)., ed. A. Wilson, 623 (cited on page 78)

Gu, M. F. 2006, in High Resolution X-ray Spectroscopy: towards XEUS and Con-X (cited on page 147)

Guainazzi, M., Barbarisi, I., Bianchi, S., Osuna, P., & Salgado, J. 2008, AdSpR, 41, 1998 (cited on page 103)

Guainazzi, M. & Bianchi, S. 2007, in Astronomical Society of the Pacific Conference Series, Vol. 373, The Central Engine of Active Galactic Nuclei, ed. L. C. Ho & J.-W. Wang, 467 (cited on pages 54 and 106)

Gültekin, K., Richstone, D. O., Gebhardt, K., et al. 2009, ApJ, 698, 198 (cited on page 22)

Halpern, J. P. 1984, ApJ, 281, 90 (cited on page 10)

Hamann, F. & Ferland, G. 1999, ARA&A, 37, 487 (cited on page 78)

Harris, D. E. & Krawczynski, H. 2006, ARA&A, 44, 463 (cited on page 3)

Holczer, T., Behar, E., & Arav, N. 2010, ApJ, 708, 981 (cited on pages 111 and 148)

Holczer, T., Behar, E., & Kaspi, S. 2007, ApJ, 663, 799 (cited on pages 15, 49, 56, and 69)

Hopkins, P. F. & Elvis, M. 2010, MNRAS, 401, 7 (cited on pages 1 and 18)

Horne, K., Peterson, B. M., Collier, S. J., & Netzer, H. 2004, PASP, 116, 465 (cited on page 6)

Huchra, J., Latham, D. W., da Costa, L. N., Pellegrini, P. S., & Willmer, C. N. A. 1993, AJ, 105, 1637 (cited on page 52)

Jaffe, W., Meisenheimer, K., Röttgering, H. J. A., et al. 2004, Nature, 429, 47 (cited on page 9)

Kaastra, J. S., de Vries, C., Steenbrugge, K., et al. 2011a, submitted to A&A (cited on page 109)

Kaastra, J. S., de Vries, C. P., Steenbrugge, K. C., et al. 2011b, A&A, 534, A37 (cited on pages 50, 68, and 73)

Kaastra, J. S., Lanz, T., Hubeny, I., & Paerels, F. B. S. 2009, A&A, 497, 311 (cited on page 29)

Kaastra, J. S., Mewe, R., Liedahl, D. A., Komossa, S., & Brinkman, A. C. 2000, A&A, 354, L83 (cited on page 12)

Kaastra, J. S., Mewe, R., & Nieuwenhuijzen, H. 1996, in UV and X-ray Spectroscopy of Astrophysical and Laboratory Plasmas, ed. K. Yamashita & T. Watanabe, 411–414 (cited on pages 31, 79, and 93)

Kaastra, J. S., Petrucci, P.-O., Cappi, M., et al. 2011c, A&A, 534, A36 (cited on pages 50, 51, and 52)

Kaastra, J. S., Raassen, A. J. J., Mewe, R., et al. 2004, A&A, 428, 57 (cited on pages 28 and 95)

Kaastra, J. S., Steenbrugge, K. C., Brinkman, A. C., et al. 2003, in Astronomical Society of the Pacific Conference Series, Vol. 290, Active Galactic Nuclei: From Central Engine to Host Galaxy, ed. S. Collin, F. Combes, & I. Shlosman, 101 (cited on pages 86 and 103)

Kaastra, J. S., Steenbrugge, K. C., Brinkman, A. C., & Edelson, R. 2002a, in X-ray Spectroscopy of AGN with Chandra and XMM-Newton, ed. T. Boller, S. Komossa, S. Kahn, H. Kunieda, & L. Gallo, 15 (cited on page 79)

Kaastra, J. S., Steenbrugge, K. C., Raassen, A. J. J., et al. 2002b, A&A, 386, 427 (cited on pages 6, 7, and 11)

Kaastra, J. S., Steenbrugge, K. C., Raassen, A. J. J., et al. 2002c, A&A, 386, 427 (cited on pages 78, 79, 82, 83, 92, 94, and 109)

Kaspi, S. & Behar, E. 2010, Space Sci. Rev., 157, 249 (cited on pages 17 and 18)

Kaspi, S., Brandt, W. N., George, I. M., et al. 2002, ApJ, 574, 643 (cited on pages 11, 12, 55, and 92)

Kelly, R. L. 1987, Atomic and ionic spectrum lines below 2000 Angstroms. Hydrogen through Krypton (cited on page 36)

Kinkhabwala, A., Sako, M., Behar, E., et al. 2002, ApJ, 575, 732 (cited on pages 92, 103, 106, and 111)

Königl, A. & Kartje, J. F. 1994, ApJ, 434, 446 (cited on page 13)

Kraemer, S. B., Crenshaw, D. M., Filippenko, A. V., & Peterson, B. M. 1998, ApJ, 499, 719 (cited on pages 86 and 92)

Kraemer, S. B., Crenshaw, D. M., Gabel, J. R., et al. 2006, ApJS, 167, 161 (cited on page 92)

Kraemer, S. B., Crenshaw, D. M., Yaqoob, T., et al. 2003, ApJ, 582, 125 (cited on pages 56, 67, and 72)

Kraemer, S. B., George, I. M., Crenshaw, D. M., et al. 2005, ApJ, 633, 693 (cited on page 112)

Kraemer, S. B., Schmitt, H. R., & Crenshaw, D. M. 2008, ApJ, 679, 1128 (cited on pages 7 and 106)

Kraemer, S. B., Trippe, M. L., Crenshaw, D. M., et al. 2009, ApJ, 698, 106 (cited on page 7)

Kriss, G. A., Arav, N., Kaastra, J. S., et al. 2011, A&A, 534, A41 (cited on pages 12 and 72)

Kriss, G. A., Green, R. F., Brotherton, M., et al. 2000, ApJ, 538, L17 (cited on pages 56, 67, and 72)

Krolik, J. H. & Kriss, G. A. 1995, ApJ, 447, 512 (cited on pages 40, 85, and 98)

Krolik, J. H. & Kriss, G. A. 2001, ApJ, 561, 684 (cited on pages 8, 12, and 49)

Krongold, Y., Nicastro, F., Brickhouse, N. S., et al. 2003, ApJ, 597, 832 (cited on pages 15, 49, and 57)

Krongold, Y., Nicastro, F., Brickhouse, N. S., Elvis, M., & Mathur, S. 2005, ApJ, 622, 842 (cited on page 28)

Krongold, Y., Nicastro, F., Elvis, M., et al. 2007, ApJ, 659, 1022 (cited on pages 23, 49, and 92)

Lee, J. C., Ogle, P. M., Canizares, C. R., et al. 2001, ApJ, 554, L13 (cited on page 111)

Lepson, J. K., Beiersdorfer, P., Behar, E., & Kahn, S. M. 2005, Nuclear Instruments and Methods in Physics Research B, 235, 131 (cited on page 148)

Lodders, K. & Palme, H. 2009, Meteoritics and Planetary Science Supplement, 72, 5154 (cited on pages 51 and 59)

Longinotti, A. L., Bianchi, S., Ballo, L., de La Calle, I., & Guainazzi, M. 2009, MNRAS, 394, L1 (cited on page 6)

Longinotti, A. L., Nucita, A., Santos-Lleo, M., & Guainazzi, M. 2008, A&A, 484, 311 (cited on pages 92 and 102)

Matt, G., Fabian, A. C., & Ross, R. R. 1993, MNRAS, 262, 179 (cited on page 88)

Mazzalay, X., Rodríguez-Ardila, A., & Komossa, S. 2010, MNRAS, 405, 1315 (cited on page 106)

McHardy, I. M., Gunn, K. F., Uttley, P., & Goad, M. R. 2005, MNRAS, 359, 1469 (cited on page 109)

McHardy, I. M., Papadakis, I. E., Uttley, P., Page, M. J., & Mason, K. O. 2004, MNRAS, 348, 783 (cited on page 79)

McNamara, B. R., Kazemzadeh, F., Rafferty, D. A., et al. 2009, ApJ, 698, 594 (cited on page 21)

McNamara, B. R. & Nulsen, P. E. J. 2007, ARA&A, 45, 117 (cited on pages 21 and 48)

Mehdipour, M., Branduardi-Raymont, G., Kaastra, J. S., et al. 2011, A&A, 534, A39 (cited on page 54)

Miniutti, G. & Fabian, A. C. 2004, MNRAS, 349, 1435 (cited on page 87)

Miyoshi, M., Moran, J., Herrnstein, J., et al. 1995, Nature, 373, 127 (cited on page 2)

Moe, M., Arav, N., Bautista, M. A., & Korista, K. T. 2009, ApJ, 706, 525 (cited on page 48)

Morganti, R., Tadhunter, C., Oosterloo, T., Holt, J., & Emonts, B. 2007, in ASPC, Vol. 373, The Central Engine of Active Galactic Nuclei, ed. L. C. Ho & J.-W. Wang, 343 (cited on page 106)

Mullaney, J. R., Ward, M. J., Done, C., Ferland, G. J., & Schurch, N. 2009, MNRAS, 394, L16 (cited on pages 9 and 117)

Murphy, E. M., Lockman, F. J., Laor, A., & Elvis, M. 1996, ApJS, 105, 369 (cited on pages 29 and 52)

Murray, N. & Chiang, J. 1997, ApJ, 474, 91 (cited on page 49)

Nahar, S. N. 1999, ApJS, 120, 131 (cited on pages 86 and 87)

Nandra, K., Fabian, A. C., George, I. M., et al. 1993, MNRAS, 260, 504 (cited on page 79)

Netzer, H. 1990, in 20. Saas-Fee Advanced Course of the Swiss Society for Astrophysics and Astronomy: Active galactic nuclei, p. 57 - 160, ed. R. D. Blandford, H. Netzer, L. Woltjer, T. J.-L. Courvoisier, & M. Mayor, 57–160 (cited on pages 86 and 99)

Netzer, H. 2008, New A Rev., 52, 257 (cited on page 7)

Netzer, H., Chelouche, D., George, I. M., et al. 2002, ApJ, 571, 256 (cited on page 28)

Netzer, H., Kaspi, S., Behar, E., et al. 2003, ApJ, 599, 933 (cited on pages 28, 49, and 92)

Nucita, A. A., Guainazzi, M., Longinotti, A. L., et al. 2010, A&A, 515, A47 (cited on page 106)

Page, M. J., Davis, S. W., & Salvi, N. J. 2003, MNRAS, 343, 1241 (cited on page 29)

Peacock, N. J., Speer, R. J., & Hobby, M. G. 1969, Journal of Physics B Atomic Molecular Physics, 2, 798 (cited on page 148)

Peterson, B. M. 1997, An Introduction to Active Galactic Nuclei (Publisher: Cambridge, New York Cambridge University Press, 1997 Physical description xvi, 238 p.) (cited on page 78)

Peterson, B. M. 2008, New A Rev., 52, 240 (cited on page 1)

Peterson, B. M. 2010, in IAU Symposium, Vol. 267, IAU Symposium, 151–160 (cited on pages 5 and 6)

Peterson, B. M., Balonek, T. J., Barker, E. S., et al. 1991, ApJ, 368, 119 (cited on page 5)

Peterson, B. M., Ferrarese, L., Gilbert, K. M., et al. 2004, ApJ, 613, 682 (cited on pages 86, 92, and 109)

Peterson, B. M. & Wandel, A. 2000, ApJ, 540, L13 (cited on pages 2 and 49)

Peterson, J. R., Paerels, F. B. S., Kaastra, J. S., et al. 2001, A&A, 365, L104 (cited on page 21)

Phillips, M. M., Baldwin, J. A., Atwood, B., & Carswell, R. F. 1983, ApJ, 274, 558 (cited on pages 54 and 67)

Pinto, C., Kaastra, J. S., Costantini, E., & Verbunt, F. 2010, A&A, 521, A79 (cited on page 52)

Ponti, G., Cappi, M., Vignali, C., et al. 2009, MNRAS, 394, 1487 (cited on pages 17, 48, and 50)

Porquet, D. & Dubau, J. 2000, A&AS, 143, 495 (cited on page 54)

Pounds, K., Reeves, J., O'Brien, P., et al. 2001, ApJ, 559, 181 (cited on page 29)

Pounds, K. A. & Reeves, J. N. 2009, MNRAS, 397, 249 (cited on page 48)

Pounds, K. A., Reeves, J. N., Page, K. L., et al. 2003, MNRAS, 341, 953 (cited on pages 17 and 83)

Predehl, P. & Schmitt, J. H. M. M. 1995, A&A, 293, 889 (cited on page 30)

Rafferty, D. A., McNamara, B. R., Nulsen, P. E. J., & Wise, M. W. 2006, ApJ, 652, 216 (cited on page 21)

Reeves, J. N., Fabian, A. C., Kataoka, J., et al. 2006, Astronomische Nachrichten, 327, 1079 (cited on page 88)

Reeves, J. N., O'Brien, P. T., & Ward, M. J. 2003, ApJ, 593, L65 (cited on pages 17 and 48)

Risaliti, G., Elvis, M., Fabbiano, G., Baldi, A., & Zezas, A. 2005, ApJ, 623, L93 (cited on page 9)

Romano, P., Mathur, S., Turner, T. J., et al. 2004, ApJ, 602, 635 (cited on page 109)

Sako, M., Kahn, S. M., Branduardi-Raymont, G., et al. 2003, ApJ, 596, 114 (cited on page 111)

Scannapieco, E. & Oh, S. P. 2004, ApJ, 608, 62 (cited on page 1)

Schawinski, K., Thomas, D., Sarzi, M., et al. 2007, MNRAS, 382, 1415 (cited on page 106)

Schmidt, M. 1963, Nature, 197, 1040 (cited on page 2)

Schmidt, M., Beiersdorfer, P., Chen, H., et al. 2004, ApJ, 604, 562 (cited on page 148)

Schmitt, H. R., Antonucci, R. R. J., Ulvestad, J. S., et al. 2001, ApJ, 555, 663 (cited on page 102)

Schödel, R., Ott, T., Genzel, R., et al. 2003, ApJ, 596, 1015 (cited on page 2)

Sembach, K. R., Savage, B. D., Lu, L., & Murphy, E. M. 1995, ApJ, 451, 616 (cited on page 52)

Sergeev, S. G., Doroshenko, V. T., Dzyuba, S. A., et al. 2007, ApJ, 668, 708 (cited on page 92)

Seyfert, C. K. 1943, ApJ, 97, 28 (cited on page 2)

Shakura, N. I. & Sunyaev, R. A. 1973, A&A, 24, 337 (cited on page 4)

Smith, R. A. N., Page, M. J., & Branduardi-Raymont, G. 2007, A&A, 461, 135 (cited on pages 29, 49, 50, and 72)

Smith, R. A. N., Page, M. J., & Branduardi-Raymont, G. 2008, A&A, 490, 103 (cited on page 106)

Somerville, R. S., Hopkins, P. F., Cox, T. J., Robertson, B. E., & Hernquist, L. 2008, MNRAS, 391, 481 (cited on page 1)

Spoon, H. W. W., Armus, L., Marshall, J. A., et al. 2009, ApJ, 693, 1223 (cited on page 8)

Spoon, H. W. W. & Holt, J. 2009, ApJ, 702, L42 (cited on page 8)

Steenbrugge, K. C., Fenovčík, M., Kaastra, J. S., Costantini, E., & Verbunt, F. 2009, A&A, 496, 107 (cited on pages 12 and 28)

Steenbrugge, K. C., Kaastra, J. S., Crenshaw, D. M., et al. 2005, A&A, 434, 569 (cited on pages 12, 15, 49, 56, 57, 68, 69, 78, 80, 81, 82, 83, 85, 94, 95, 99, 100, and 111)

Steenbrugge, K. C., Kaastra, J. S., de Vries, C. P., & Edelson, R. 2003, A&A, 402, 477 (cited on pages 78 and 94)

Steenbrugge, K. C., Kaastra, J. S., Detmers, R. G., et al. 2011, A&A, 534, A42 (cited on page 60)

Strüder, L., Briel, U., Dennerl, K., et al. 2001, A&A, 365, L18 (cited on page 28)

Suganuma, M., Yoshii, Y., Kobayashi, Y., et al. 2006, ApJ, 639, 46 (cited on pages 9, 19, and 87)

Tamura, T., Kaastra, J. S., Peterson, J. R., et al. 2001, A&A, 365, L87 (cited on page 21)

Tarter, C. B., Tucker, W. H., & Salpeter, E. E. 1969, ApJ, 156, 943 (cited on pages 15, 85, and 97)

Tombesi, F., Cappi, M., Reeves, J. N., et al. 2010a, A&A, 521, A57 (cited on page 17)

Tombesi, F., Cappi, M., Reeves, J. N., et al. 2010b, A&A, 521, A57 (cited on page 48)

Tombesi, F., Sambruna, R. M., Reeves, J. N., et al. 2010c, ApJ, 719, 700 (cited on page 48)

Tristram, K. R. W., Meisenheimer, K., Jaffe, W., et al. 2007, A&A, 474, 837 (cited on page 9)

Vaughan, S. & Uttley, P. 2008, MNRAS, 390, 421 (cited on page 18)

Weymann, R. J., Carswell, R. F., & Smith, M. G. 1981, ARA&A, 19, 41 (cited on page 78)

Woo, J. & Urry, C. M. 2002, ApJ, 579, 530 (cited on page 109)

Yaqoob, T., George, I. M., Nandra, K., et al. 2001, ApJ, 546, 759 (cited on pages 83 and 94)

Yaqoob, T., McKernan, B., Kraemer, S. B., et al. 2003, ApJ, 582, 105 (cited on pages 29, 49, 56, 72, and 73)

Appendix A

Appendix to Chapter 2 and 3

A.1 Chapter 2: Additional figures

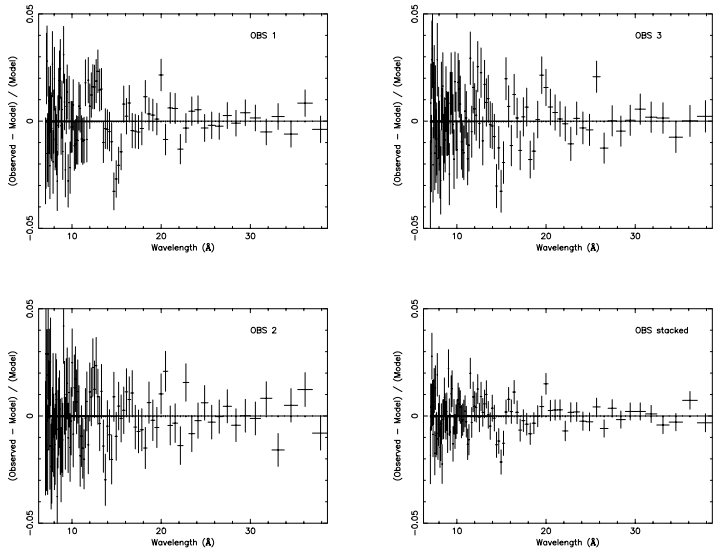

Figure A.1: The best fit residuals for the pn spectra after applying the *knak* model. Left from top to bottom: observation 1 and 2. Right, from top to bottom: observation 3 and the stacked spectrum.

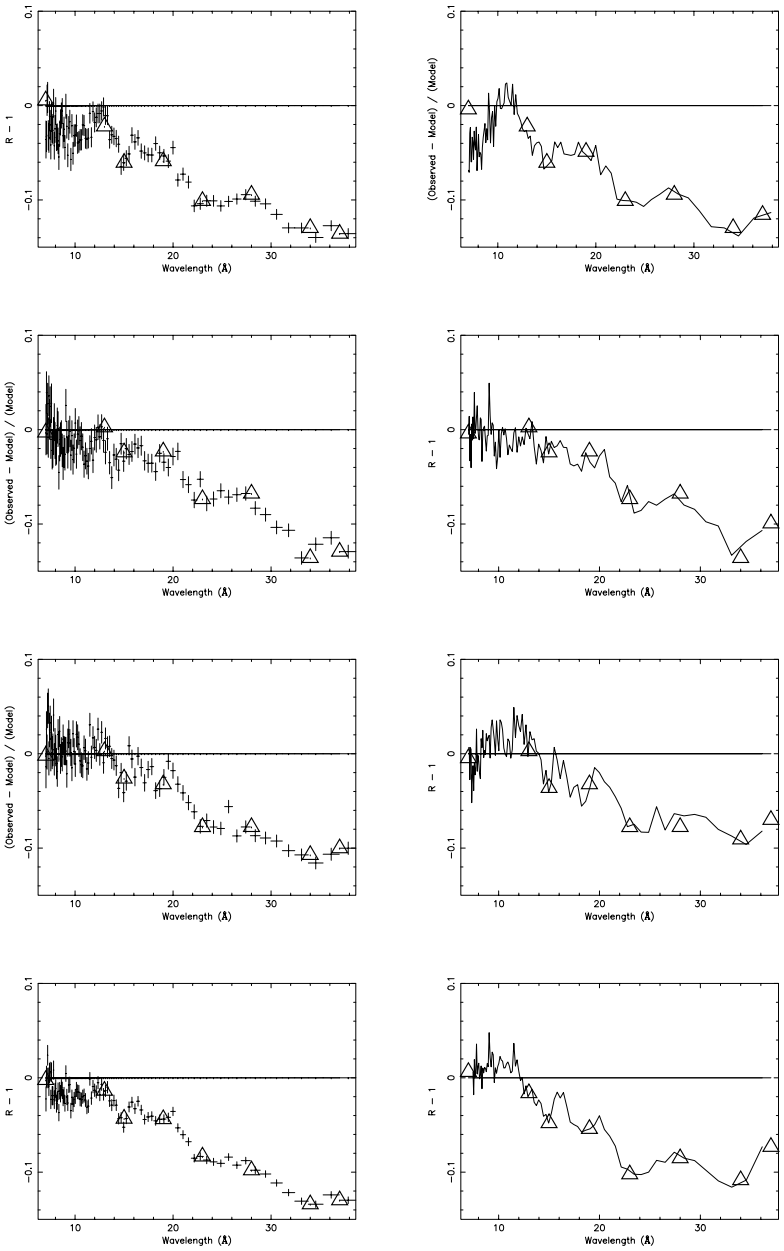

Figure A.2: The ratios $R(PI) = \frac{C_O(PI)}{C_M(PI)}$ for all observations. The lefthand column shows the ratios for method 1, while the righthand column shows the ratios for method 2. The locations of the *knak* hinge points are indicated by the triangles (The y-axis values for each point are not accurate, as the values shown in Table 2.2 are averaged between hinge points, the triangles shown here are just to guide the eye). From top to bottom: Observation 1, 2, 3 and the stacked spectrum.

A.2 Chapter 3: Improving the atomic data

Due to the high quality of the Mrk 509 dataset, we have also updated some of the laboratory wavelengths of the important ions detected in the Mrk 509 spectrum. Table A.1 shows all the updated lines. The O III lines are not resolved, so the strongest line at 23.071 was used (Gu 2006) and the other two lines were shifted by the same amount.

Table A.1: Updated line list for important ions in the Mrk 509 spectrum.

Ion	Wavelength (new) (Å)	Wavelength (old) (Å)	Reference[1]
N VI	28.7875	28.7870	1
O III	22.9400	22.9784	2
O III	23.0280	23.0489	2
O III	23.0710	23.1092	2
O V	19.3570	19.3251	2
O V	19.9680	19.9242	2
O VI	18.2699	18.2896	2
O VI	18.2700	18.2897	2
O VI	18.5869	18.6059	2
O VI	18.5870	18.6060	2
O VI	19.1798	19.1355	2
O VI	19.1805	19.1362	2
O VI	19.3789	19.3412	2
O VI	19.3791	19.3414	2
O VI	22.0189	22.0063	3
O VI	22.0205	22.0079	3
O VII	17.7683	17.7680	1
O VII	18.6284	18.6288	1
Ne VIII	13.6533	13.6460	4
Ne VIII	13.6553	13.6480	4
S XIII	32.2380	32.2420	5
S XIV	30.4330	30.4270	5
S XIV	30.4750	30.4690	5
Fe XVII	15.2610	15.2650	6
Fe XVIII	14.3720	14.3780	7
Fe XVIII	14.5340	14.5400	7
Fe XVIII	14.5710	14.5550	7
Fe XIX	13.4620	13.4650	7
Fe XIX	13.5180	13.5210	7
Fe XIX	13.7950	13.7980	7
Fe XX	12.8240	12.8130	7
Fe XX	12.8460	12.8270	7
Fe XX	12.8640	12.8470	7
Fe XX	12.9150	12.9040	7
Fe XXI	12.2840	12.2860	7

[1] References; (1) Engstrom & Litzen (1995); (2) Holczer et al. (2010); (3) Schmidt et al. (2004); (4) Peacock et al. (1969); (5) Lepson et al. (2005); (6) Brown et al. (1998); (7) Brown et al. (2002).